

University of Science and Technology of China

A dissertation for doctor's degree



**Synthesis and  
Characterization of Hybrid  
Nanostructures**

Author's Name: Majid Khan

Speciality: Materials Processing Engineering

Supervisor: Professor Liangbin Li

Co-Supervisor: Professor Zeming Qi

Finished time: 04, 2015



## 中国科学技术大学学位论文原创性声明

本人声明所呈交的学位论文,是本人在导师指导下进行研究工作所取得的成果。除已特别加以标注和致谢的地方外,论文中不包含任何他人已经发表或撰写过的研究成果。与我一同工作的同志对本研究所做的贡献均已在论文中作了明确的说明。

作者签名: Mao Pi-Chang

签字日期: 2015-06-02

## 中国科学技术大学学位论文授权使用声明

作为申请学位的条件之一,学位论文著作权拥有者授权中国科学技术大学拥有学位论文的部分使用权,即:学校有权按有关规定向国家有关部门或机构送交论文的复印件和电子版,允许论文被查阅和借阅,可以将学位论文编入《中国学位论文全文数据库》等有关数据库进行检索,可以采用影印、缩印或扫描等复制手段保存、汇编学位论文。本人提交的电子文档的内容和纸质论文的内容相一致。

保密的学位论文在解密后也遵守此规定。

公开    保密 (\_\_\_\_年)

作者签名: Mao Pi-Chang

导师签名: 李良彬

签字日期: 2015-06-02

签字日期: 2015.6.2

## Abstract

This thesis deals with the fabrication and manufacturing of novel hybrid nanostructures with enhanced functionality, particularly core-shell hybrid nanomaterials, 2D nanostructured materials and surfaces, and polymer nanocomposites. The study includes four parts; in the first part, core-shell hybrid nanocomposites composed of ZnO nanorods/Ag nanoparticles were prepared by a very simple chemical technique. ZnO nanorods were employed as core material for Ag seeds, and subsequent nucleation and growth of Ag nanoparticle by a cationic surfactant cetyltrimethylammonium bromide (CTAB) formed the ZnO nanorods/Ag core-shell nanocomposites and its morphological and optical properties have been investigated. The integration of semiconductor and noble metal nanoparticles with controlled structure at the nanoscale can effectively combine various effects specific to the different domains of the nanocomposite for better application versatility. This work demonstrates that Ag nanoparticles with an average diameter of 20 nm were coated onto the surface of hexagonal phase ZnO nanorods with a minimum amount of 0.09 mmol concentration of CTAB. The excitonic absorption band and surface plasmon absorption band of the ZnO NRs/Ag nanocomposites show red-shifts relative to pristine ZnO nanorods and metallic Ag nanoparticles. The coating of Ag nanoparticles onto the ZnO nanorods display red-shift in the near band edge luminescence spectra and a reasonable detracting in the deep level emission spectra compared with the pure ZnO nanorods.

In the second part, palladium (Pd) octahedral and spherical nanocrystals were successfully synthesized on reduced graphene oxide (GO) by surface adsorption of H<sub>2</sub> and CO in the presence of capping agent poly(vinylpyrrolidone) (PVP). Their comparative studies as anode material for direct methanol fuel cells (DMFCs) have been measured by hydrogen evolution reaction (HER) performance and methanol oxidation reaction (MOR) activity were studied in HClO<sub>4</sub> acidic media. Pd octahedral nanocrystals have shown the low onset potential in the HER region and specific MOR activity of ca. 4.3 mA cm<sup>-2</sup> and mass activity of ca. 5300 mA mg<sup>-1</sup><sub>Pd</sub> much higher than that of spherical nanocrystals. This result can be attributed to the abundance of (111) facets on the Pd octahedral shaped nanocrystals. Moreover, bimetallic PdPt nanoparticles of different compositions were anchored on graphene sheets through a novel and facile route and its electrocatalytic properties including methanol oxidation reaction (MOR), oxygen reduction reaction (ORR) and methanol tolerant oxygen reduction reaction (MORR) were evaluated in HClO<sub>4</sub> solution. The as-synthesized

GO/PdPt composites showed higher electrocatalytic activity, higher specific ORR activity and excellent poisoning tolerance for the methanol electro-oxidation compared with graphene supported monometallic catalyst, due to the combined effect of the composite with unique properties of graphene and alloying of Pd with Pt.

In the third part, we developed a facile and novel hydrothermal route for the synthesis of 3D MoS<sub>2</sub>/GO-CNT hybrid nanostructure and explored their practical application in hydrogen evolution reactions. This new type of 3D networked structure was hydrothermally synthesized through an aqueous dispersion of GO and CNT, followed by the anchoring of MoS<sub>2</sub> nanoparticles on the surfaces of GO-CNT. This ternary composite shows superior electrocatalytic activity and stability in the hydrogen evolution reaction (HER) with a low onset potential of only 35 mV, a Tafel slope of ~38 mV/decade and an apparent exchange current density of  $2.02 \times 10^{-4}$  mA. The superior hydrogen evolution activity stemmed from the synergistic effect of the MoS<sub>2</sub> with electrocatalytically active edge sites and excellent electrical coupling to the underlying graphene and CNTs network.

In the last and fourth part, bulk transparent polymer-inorganic nanocomposites were produced by a novel synthesis method and its optical and thermal properties have been investigated. Morphological study on the nanocomposite reveals that a homogenous dispersion of ZnO nanoparticles was achieved in the PMMA matrix. A reasonable increase in thermal and optical properties was also observed after loading a small amount of ZnO nanoparticles. Moreover, the PMMA/ZnO nanocomposites films were highly transparent and possess good absorption of light in the UV region which can strongly shield harmful UV light for human health.

Comprehensive characterization of the hybrid materials synthesized in this work has been undertaken using a wide range of techniques; scanning electron microscopy (SEM) and field emission SEM (FESEM), transmission electron microscopy (TEM) and high resolution TEM (HRTEM), X-ray diffraction (XRD), Raman spectroscopy, X-ray photoelectron spectrometry (XPS), UV-Vis and photoluminescence (PL), thermo gravimetric analysis (TGA), and differential scanning calorimetry (DSC).

**Keywords:** Hybrid nanostructures; methanol oxidation reaction; oxygen reduction reaction; methanol tolerant oxygen reduction reaction; hydrogen evolution reaction

## Table of Contents

<b>Abstract</b> .....	i
<b>List of Figures</b> .....	vi
<b>List of Tables</b> .....	ix
<b>Chapter 1 Introduction</b> .....	1
1.1 Introduction.....	1
1.1.1 Background and Motivation.....	1
1.2 Objectives .....	4
1.3 Thesis Organization .....	5
1.4 References.....	6
<b>Chapter 2 Synthesis and Characterization of ZnO/Ag Core-Shell Nanocomposites</b> .....	8
2.1 Introduction.....	8
2.2 Experimental Details.....	10
2.2.1 Synthesis of ZnO Nanorods .....	10
2.2.2 Preparation of ZnO NRs/Ag core-shell nanocomposite.....	10
2.2.3 Characterization Tools .....	11
2.3 Results and Discussion .....	11
2.3.1 Morphology and Mechanism .....	11
2.3.2 Structural Characterization .....	17
2.3.3 Optical Properties.....	20
2.4 Summary .....	23
2.5 References.....	24
<b>Chapter 3 Synthesis and Characterization of Pd Octahedral and Pd Spherical Nanocrystals on Graphene Oxide used as Anode Material for Direct Methanol Fuel Cells</b> .....	27
3.1 Introduction.....	27
3.2 Methanol Oxidation Reaction (MOR) .....	29
3.3 Experimental Procedure.....	31
3.3.1 Chemicals and Materials.....	31
3.3.2 Synthesis of Graphene Oxide.....	32
3.3.3 Synthesis of Pd Octahedral Nanocrystals on Graphene Oxide .....	32
3.3.4 Synthesis of Pd Spherical Nanocrystals on Graphene Oxide.....	32
3.3.5 Characterization Tools .....	32

## Table of Contents

---

3.4	Results and Discussion .....	33
3.4.1	Morphology, Mechanism and UV-Vis Absorption.....	33
3.4.2	Structural Characterization .....	37
3.4.3	Electrochemical Performance .....	38
3.5	Summary .....	43
3.6	References.....	44
<b>Chaper 4 Preparation and Characterization of Pd-Pt Bimetallic Alloy on Graphene oxide and its Electrocatalytic Properties .....</b>		<b>47</b>
4.1	Introduction.....	47
4.2	Oxygen Reduction Reaction (ORR) .....	48
4.3	Experimental Procedure.....	50
4.3.1	Chemicals and Materials.....	50
4.3.2	Synthesis of Graphene Oxide.....	50
4.3.3	Synthesis of Clean PdPt Alloy Nanocrystals on Graphene Oxide .....	51
4.3.4	Characterization .....	51
4.3.5	Electrochemical Experiments .....	51
4.3.6	Electrocatalytic Applications .....	52
4.4	Results and Discussion .....	52
4.4.1	Morphology.....	52
4.4.2	Structural Characterization .....	54
4.4.3	Electrochemical Performance .....	57
4.5	Summary .....	64
4.6	References.....	64
<b>Chaper 5 Synthesis and Characterization of MoS<sub>2</sub>/GO-CNT Composite for Electrocatalytic Application of Hydrogen Evolution Reaction .....</b>		<b>68</b>
5.1	Introduction.....	68
5.2	Hydrogen Evolution Reaction.....	69
5.3	Experimental Procedure.....	72
5.3.1	Materials .....	72
5.3.2	Synthesis of GO .....	73
5.3.3	Synthesis of COOH-Functionalized MWCNTs.....	73
5.3.4	Synthesis of GO-CNT Composite.....	73
5.3.5	Synthesis of MoS <sub>2</sub> /GO-CNT Composite .....	73
5.3.6	Characterizations.....	74

5.3.7	Electrochemical Measurements .....	74
5.4	Results and Discussion .....	75
5.4.1	Morphology and Mechanism .....	75
5.4.2	Structural Characterization .....	79
5.5	Electrochemical Performance .....	84
5.6	Summary .....	86
5.7	References.....	87
<b>Chaper 6</b>	<b>Synthesis and Characterization of ZnO/PMMA Polymer Nanocomposites.....</b>	<b>90</b>
6.1	Introduction.....	90
6.2	Optical Properties of Polymer Nanocomposites .....	92
6.3	Experimental Details.....	93
6.3.1	Chemical Reagents.....	93
<b>6.3.2</b>	<b>Synthesis of ZnO Nanoparticles .....</b>	<b>93</b>
6.3.3	Preparation of ZnO/PMMA Nanocomposite Thin Film .....	93
6.3.4	Characterization Tools .....	94
6.4	Results & Discussion .....	94
6.4.1	Structural Characterization .....	94
6.4.2	Surface Morphology .....	95
6.4.3	Thermal Properties.....	97
6.4.4	Optical Characterization .....	100
6.5	Summary .....	102
6.6	References.....	103
<b>Acknowledgements</b>	.....	<b>106</b>
<b>List of Publications</b>	.....	<b>108</b>

## List of Figures

<b>Figure 2.1</b> Schematic representation of the synthesis of ZnO NRs/Ag core-shell nanocomposites. ....	12
<b>Figure 2.2</b> SEM and FESEM images of ZnO NRs/Ag nanocomposite obtained (a) and (b) without using CTAB (c) and (d) with 2 mmol of CTAB. ....	13
<b>Figure 2.3</b> Low and high magnification SEM and FESEM images of (a) and (b) ZnO NRs, (c) and (d) ZnO NRs/Ag-1 and (e) and (f) ZnO NRs/Ag-2. ....	14
<b>Figure 2.4</b> TEM images of (a) and (b) ZnO NRs, (c) and (d) ZnO NRs/Ag-1 and (e) and (f) ZnO NRs/Ag-1 annealed at 200 °C. ....	15
<b>Figure 2.5</b> HRTEM images of (a) ZnO NRs and (b) ZnO NRs/Ag-1. ....	16
<b>Figure 2.6</b> EDX spectra of ZnO NRs/Ag-1 nanocomposite. ....	16
<b>Figure 2.7</b> (a) XRD patterns of pure ZnO NRs, ZnO NRs/Ag-1 and ZnO NRs/Ag-2 nanocomposites, and (b) XRD patterns of ZnO NRs/Ag-1 nanocomposite annealed at 200 °C. ....	18
<b>Figure 2.8</b> Raman spectra of the pure ZnO NRs and ZnO NRs/Ag-1 nanocomposite. ....	19
<b>Figure 2.9</b> UV-Vis absorption spectra of the pure ZnO NRs, Ag nanoparticles, ZnO NRs/Ag nanocomposites. ....	21
<b>Figure 2.10</b> Room temperature photoluminescence (PL) of pure ZnO NRs and ZnO NRs/Ag nanocomposites. Inset shows magnified UV emission spectra. ....	23
<b>Figure 3.1</b> Schematic representation of the synthesis procedure of the GO/Pd hybrid catalyst. ....	34
<b>Figure 3.2</b> Characterizations of synthesized Graphene Oxide (a) TEM image, (b) FTIR spectrum, (c) UV-Vis spectrum and (d) CV in 0.1M HClO <sub>4</sub> at a scan rate of 50 mV/s vs RHE. ....	34
<b>Figure 3.3</b> FE-SEM images of (a) & (b) Pd nanocrystals on GO sheets, (b) & (d) High magnifications images of Pd Octahedral and Pd Spherical nanocrystals on GO sheets, respectively. ....	35
<b>Figure 3.4</b> UV-Vis spectra of Pd Octahedral (GO/Pd-01) and Pd Spherical (GO/Pd-02) nanocrystals. ....	36
<b>Figure 3.5</b> XRD spectra of Pd octahedral (GO/Pd-01) and Pd spherical (GO/Pd-02) nanocrystals. ....	37
<b>Figure 3.6</b> CVs of Pd octahedral (GO/Pd-01) nanocrystals after different cleaning treatments, in 0.1M HClO <sub>4</sub> at a scan rate of 50 mV/s vs RHE. ....	39
<b>Figure 3.7</b> CVs of Pd spherical (GO/Pd-02) nanocrystals after different cleaning treatments, in 0.1M HClO <sub>4</sub> at a scan rate of 50 mV/s vs RHE. ....	39



<b>Figure 3.8</b> CVs of Pd octahedral (GO/Pd-01) and Pd spherical (GO/Pd-02) nanocrystals after CO-stripping cleaning treatment in a wide potential range between 0 V to 1.2 V vs RHE to show the oxidation ( $H_{ads}$ , $O_{ads}$ ) reduction ( $H_{des}$ , $O_{des}$ ) peaks, in 0.1M HClO <sub>4</sub> at a scan rate of 50 mV/s vs RHE.....	40
<b>Figure 3.9</b> Polarization curves for HER activity of Pd octahedral (GO/Pd-01) and Pd spherical (GO/Pd-02) nanocrystals in 0.1M HClO <sub>4</sub> at a scan rate of 10 mV/s vs Ag/AgCl. $E_{onset}$ for HER is measured by tangent method. ....	40
<b>Figure 3.10</b> MOR activity peaks (forward and backward scans) of Pd octahedral (GO/Pd-01) and Pd spherical (GO/Pd-02) nanocrystals in 0.1M HClO <sub>4</sub> + 1M CH <sub>3</sub> OH at a scan rate of 50 mV/s vs RHE.....	42
<b>Figure 3.11</b> CA results of MOR activity for Pd octahedral (GO/Pd-01) and Pd spherical (GO/Pd-02) nanocrystals in 0.1M HClO <sub>4</sub> + 1M CH <sub>3</sub> OH at constant voltage 0.30 V, 0.40 V and 0.50 V up to 300 s time.....	43
<b>Figure 4.1</b> TEM images of the (a) GO/Pd (b) GO/PdPt-01 (c) GO/PdPt-02 and (d) GO/PdPt-03 composites. The scale bar is 50 nm. ....	53
<b>Figure 4.2</b> XRD patterns of GO/Pd and GO/PdPt composites. ....	55
<b>Figure 4.3</b> XPS spectra of (a-d) GO/PdPt-03 sample. Observed regions were (b) C1s with deconvolution results, (c) Pt4f and (d) Pd3d. ....	56
<b>Figure 4.4</b> Base CVs of GO/Pd, GO/Pt and GO/PdPt composites in 0.1 M HClO <sub>4</sub> at a scan rate of 50 mV/s vs RHE.....	58
<b>Figure 4.5</b> LSV peaks of GO/Pd, GO/Pt and GO/PdPt composites in 0.1 M HClO <sub>4</sub> at a scan rate of 50 mV/s vs RHE.....	59
<b>Figure 4.6</b> MOR activity peaks (forward and backward scans) of GO/Pd, GO/Pt and GO/PdPt composites w.r.t geometric surface area in 0.1 M HClO <sub>4</sub> + 1M CH <sub>3</sub> OH at a scan rate of 50 mV/s vs RHE. ....	60
<b>Figure 4.7</b> ORR polarization curves of GO/Pd and GO/PdPt composites in 0.1M HClO <sub>4</sub> at a scan rate of 50 mV/s vs RHE. ....	61
<b>Figure 4.8</b> MORR polarization curves of GO/Pd and GO/PdPt composites in 0.1M HClO <sub>4</sub> + 1M CH <sub>3</sub> OH at a scan rate of 50 mV/s vs RHE.....	63
<b>Figure 5.1</b> Volcano plot for various pure metals and metal overlayers <sup>[41]</sup> .....	71
<b>Figure 5.2</b> FESEM images of (a) GO and (b) COOH-functionalized MWCNTs.....	75
<b>Figure 5.3</b> Schematic illustration of the synthesis of MoS <sub>2</sub> /GO-CNT composite. ....	75
<b>Figure 5.4</b> (a) Low and (b) high magnification FESEM images of GO-CNT composite.....	76
<b>Figure 5.5</b> FESEM images of (a) pristine MoS <sub>2</sub> and MoS <sub>2</sub> /GO-CNT composite. (b) Low, (c) and (d) high magnification images of MoS <sub>2</sub> /GO-CNT composite.....	77
<b>Figure 5.6</b> (a) TEM and (b) HRTEM images of MoS <sub>2</sub> /GO-CNT composite. ....	78
<b>Figure 5.7</b> EDS spectra of GO-CNT and MoS <sub>2</sub> /GO-CNT composites.....	78

<b>Figure 5.8</b> XRD spectra of pristine MoS <sub>2</sub> and MoS <sub>2</sub> /GO-CNT composite. ....	79
<b>Figure 5.9</b> (a) X-ray photoemission spectroscopy (XPS) profiles of GO-CNT and MoS <sub>2</sub> /GO-CNT hybrid samples. (b) Curve fit of the C1s peak of GO-CNT. (c) Curve fit of the C1s peak of MoS <sub>2</sub> /GO-CNT. (d) Curve fit of Mo3d peak of MoS <sub>2</sub> /GO-CNT. (e) Curve fit of S2p peak of MoS <sub>2</sub> /GO-CNT. ....	80
<b>Figure 5.10</b> Raman spectra of the E <sub>12g</sub> <sup>1</sup> and A <sub>1g</sub> vibrational modes for pristine MoS <sub>2</sub> and MoS <sub>2</sub> /GO-CNT composite. ....	82
<b>Figure 5.11</b> The D and G bands of the Raman vibrational modes of reduced-GO, COOH-functionalized MWCNTs, GO-CNT and MoS <sub>2</sub> /GO-CNT composite. Their corresponding peak positions, FWHM and height of D and G respectively, are also visible in the table. ....	83
<b>Figure 5.12</b> Linear sweep voltammogram measured in a 0.1 M HClO <sub>4</sub> solution at a scan rate of 5 mVs <sup>-1</sup> and (b) corresponding Tafel slope of pristine MoS <sub>2</sub> and MoS <sub>2</sub> /GO-CNT hybrid samples. (c) Representative cyclic voltammograms of pristine MoS <sub>2</sub> and MoS <sub>2</sub> /GO-CNT composite measured in 0.1 M HClO <sub>4</sub> solution at a scan rate of 0.5 mVs <sup>-1</sup> between 0.0 V and 1.2 V. (d) A durability test of the MoS <sub>2</sub> /GO-CNT hybrid catalyst measured in 0.1M HClO <sub>4</sub> solution at a scan rate of 10 mV/s with 1000 rpm rotation speed up to 1000 cycles. ....	85
<b>Figure 6.1</b> XRD patterns of PMMA/ZnO nanocomposite films loaded with different amount of ZnO nanoparticles. ....	95
<b>Figure 6.2</b> SEM images of PMMA/ZnO nanocomposite films with (a) 0.5 wt% (b) 1.0 wt% (c) 1.5 wt% (d) 2.0 wt % filler contents. ....	96
<b>Figure 6.3</b> TGA and DTG curves of PMMA films before and after the loading of different amount of ZnO nanoparticles, taken in nitrogen atmosphere. ....	98
<b>Figure 6.4</b> (a) DSC scans of PMMA/ZnO films loaded with different amounts of ZnO nanoparticles (b) The variation in glass transition temperature (T <sub>g</sub> ) as a function of the ZnO contents. ....	99
<b>Figure 6.5</b> (a) UV-Vis spectra of PMMA/ZnO nanocomposite films loaded with different amounts of ZnO nanoparticles. (b) Transmittance of PMMA/ZnO nanocomposite films as a function of filler content in the UV (350 nm) and visible regions (550 nm). ....	101
<b>Figure 6.6</b> Room temperature photoluminescence (PL) emission spectra of PMMA/ZnO nanocomposite films loaded with different amounts of ZnO nanoparticles. ....	102

## List of Tables

<b>Table 2.1</b> Optical measurements of ZnO NRs and ZnO NRs/Ag nanocomposites. ....	21
<b>Table 4.1</b> Table illustrating the composition and the electrochemical performance of different electrocatalysts towards methanol oxidation reaction (MOR). ....	53



## Chapter 1 Introduction

### 1.1 Introduction

#### 1.1.1 Background and Motivation

Hybrid nanostructures have engrossed substantial interest during the recent years, explicitly because of the opportunity that this peculiar type of nanostructures intends to design materials with advanced and excellent physical, optical, chemical and mechanical properties <sup>[1-4]</sup>. The attractiveness of hybrid nanostructures is that various functions can be combined into one system for particular applications. Moreover, the interactions at the nanoscale between different components can prominently promote the overall application performance of the nanostructured system and even generate innovative synergistic properties <sup>[5]</sup>. Such hybrid nanostructure constituents composed of a semiconductor and a noble metal, graphene oxide and noble metals, graphene oxide-carbon nanotubes and metal dichalcogenides, and polymer nanocomposites are of pronounced importance, because of their innovative physical and chemical properties, besides they offer the opportunity to modify the optical properties, including absorption, emission, and concentration of electromagnetic radiation, the electrocatalytic phenomenon, including water-splitting, oxygen reduction and methanol oxidation reactions <sup>[6-10]</sup>. These properties allow the hybrid nanostructure to be used in the development of fuel cells, optoelectronic and sensing devices, and in the optimization of photovoltaic, electrocatalytic and photocatalytic systems.

Core-shell nanostructures have got great attraction in the last decade, since these nanostructures have emerged at the boundary between materials chemistry and many other fields, such as electronics, biomedical, pharmaceutical, optics, and catalysis. Core-shell nanostructures are extremely functional materials with modified properties. Hybrid nanostructures composed of core-shell nanomaterials can be categorized based on single or multiple materials into simple and core-shell or composite nanostructures. The core-shell type nanoparticles can be mostly defined as comprising a core (inner material) and a shell (outer layer material). These can comprise of an extensive range of different combinations in close interaction, including inorganic/inorganic, inorganic/organic, organic/inorganic, and organic/organic materials. The selection of shell material of the core-shell nanostructure is generally strongly dependent on the final application and use <sup>[11-14]</sup>. Core-shell material composed of inorganic/inorganic materials such as semiconductor and metal have got great attention in the recent years. The optical enhancement is the most prominent feature required

for a semiconductor to be used in optoelectronics and photovoltaic devices. Actually most of the semiconductors have defects in their structure and their optical emission spectra are accompanied with the defects emission spectra. Consider the case of ZnO which have oxygen vacancies localized on its surface and these defects are responsible for the defect emission in the visible region. Therefore, noble metal nanoparticles such as Ag are coated on ZnO. The captured Ag nanoparticles can interact with the surface defects. This in term will change the defect structures and lead to the passivation of deep defect activity. Consequently, more energetic electrons in the conduction band recombine with the holes in the valence band; therefore the band gap emission is enhanced.

The constantly increasing use of fossil fuels, together with the limited supply of the natural resources, has encouraged for the serious search of renewable and ecological sources of energy. In various applications, methanol fuel cells have grown into attractive contenders in transportation and electrical power generation, particularly for mobile and transportable applications due to their stimulating performance. Regardless of their great potential as a proficient device to convert chemical energy into electric energy, methanol fuel cells do have their own severe limitations that stop them from being scaled up for commercial applications [15-19]. Both the methanol oxidation reaction and the oxygen reduction reaction require a catalyst to lower their electrochemical overpotentials and to attain high voltage output, and Pt based nanomaterials have been the general choice of catalyst for both reactions. Though, such promising devices always involve noble metal catalysts, such as Pt, to gain low overpotential and faster kinetics of their slow half-cell reactions (such as oxygen reduction reaction and hydrogen evolution reaction) for practical applications. Thus, developing innovative nanoelectrocatalysts and thus refining the performances of fuel cells is extremely compulsory and remains a great challenge. The catalyst made of a single Pt component can hardly meet the increasing demands of industrial applications at low costs due to its extreme shortage and high price. It is also very challenging to enhance the mass activity of the monometallic catalyst of Pt because only the outermost few layers of Pt atoms in the catalyst are essentially needed in catalyzing a reaction. Furthermore, its susceptibility towards reaction poisons (e.g., CO poison) usually happening in the presence of Pt remains a serious limitation to many applications. In order to circumvent these problems, great efforts have been focused on the development of bimetallic structures that combine Pt with another metal having relatively cost-effective and plentiful features. Various metals have been used to form bimetallic with Pt and they have shown great catalytic properties. These single Pt materials and bimetallic materials require a matrix for the efficient transfer of electrons. Graphene oxide is the one

used as matrix materials and also extensively used in electrochemistry because of its low price, appropriate electrocatalytic activity for a range of redox reactions, wide potential window, and reasonably inert electrochemistry. Combining the excellent electrocatalytic activities of noble metal nanostructures with the coalescing effect of graphene oxide, graphene oxide/noble metal hybrids have emerged as a different kind of nanocomposites and acknowledged great attention in electrocatalysis [20-24].

The mechanism of an electrocatalysis occurs through typical experimental set-up which is generally consists of electrodes, electrolyte, an electrochemical cell, and an external circuit with a mechanism that permits the experimentalist to switch and observe the parameters such as potential or current. The word electrocatalysis is an indication to the optimization of an electrode processes through a careful design of the electrode material and the environments of the electrolyte.

In the field of heterogeneous catalysis, the main role of the catalyst is to increase the rate of a chemical reaction by giving a low energy pathway for the reaction to follow. The catalyst does not contribute as a reactant and it is not consumed in the reaction process. The use of a catalyst also does not disturb the position of the equilibrium. The role of an electrocatalyst can be described in a similar manner. The electrocatalyst is a material, generally a solid electrode, which accelerates an electrochemical reaction without being consumed in the chemical process. Therefore, an electrocatalyst can be assumed as a heterogeneous catalyst for an electrochemical process. The activity of an electrocatalyst towards a specific reaction is marked by its capability to increase the standard rate constant of the reaction. This increase in the rate constant is usually observed as an increase in the faradic current of the reaction [25]. In terms of hydrogen evolution reactions an excellent catalyst defined as an electrode is said to have good electrocatalytic activity for a reaction when the exchange current density is high and the Tafel slope is small. For this purpose layered materials have been extensively used in hydrogen evolution reactions in their pristine forms as well as doped and composite forms. MoS<sub>2</sub> nanostructures have been generally used as catalysts in catalytic reactions such as hydrogen evolution reactions. The catalytic activity is usually attributed to the unsaturated sites at the particle edge surfaces, parallel to the hexagonal axis of lamellar MoS<sub>2</sub> structures. The integration of layered MoS<sub>2</sub> with the morphologically compatible graphene has also shown promise in increasing the catalytic activity. The addition of graphene to MoS<sub>2</sub> increases the electronic conductivity of the electrode, thereby improving the overall activity [26]. Furthermore, MoS<sub>2</sub> is hybridized with multiwall CNTs to increase its electrical conductivity and the prepared catalysts presented

good performance towards HER. To enhance the electrocatalytic HER performance of a catalyst, it is important to increase either the surface area of the catalyst loading or making a binder free film and 3D electrode structure [27,28]. This can be achieved by making a hybrid composite of GO and MWCNTs, which leads to the formation of the catalyst with high surface area and 3D nanostructure.

At the end discussing about hybrid nanostructures composed of inorganic nanomaterials and organic polymers making a polymer nanocomposite. It have attracted immense interests due to their superior thermal (flammability resistance), biological, optical (reflex index and absorption spectrum), magnetic, mechanical (stiffness and toughness), electronic, and optoelectronic properties as compared to the individual inorganic or polymer constituent only. By integrating nanoparticles into polymer matrix even with a very little amount, many remarkable optical properties including absorption, luminescence, fluorescence, non-linearity, high reflex index, magnetic properties, and superb mechanical properties may be achieved.

## 1.2 Objectives

The main objective of this thesis work is the development of novel hybrid nanostructured materials with enhanced functionality. The work has been concerned with four different types of materials; core-shell ZnO/Ag, Pd/GO and bimetallic Pd-Pt/GO, MoS<sub>2</sub>/GO-CNT, and ZnO/PMMA.

The first type of material considered is core-shell hybrid nanostructured material composed of a semiconducting material ZnO and a noble metal Ag. The objective of the work is the development of ZnO/Ag core-shell nanocomposites where the Ag nanoparticles are homogenously coated on the surfaces of ZnO nanorods. For this part of the thesis, we developed a novel solution based method to synthesize ZnO/Ag core-shell nanocomposite via a cationic surfactant CTAB and evaluated the effectiveness of this material in the applications of photovoltaics, sensors, optoelectronics, plasmonics and photocatalysis.

The second type of material considered is hybrid nanostructured composed of octahedral and spherical shaped nanocrystals on graphene oxide and also bimetallic Pd-Pt nanoparticles on graphene oxide. The main objectives of the work was to study the oxidation of methanol on Pd supported graphene oxide and to study and methanol oxidation as well as oxygen reduction and methanol tolerant oxygen reduction on bimetallic Pd-Pt supported



graphene oxide electrodes by employing conventional and advanced electrochemical methods.

The third type of material considered is 3D hybrid nanostructured ternary composite of MoS<sub>2</sub>, graphene oxide and MWCNTs. The objective of the work was to achieve high performance electrocatalyst for hydrogen evolution reaction by fabricating ternary composite where a 3D network of graphene oxide and CNTs were coated with MoS<sub>2</sub>. This work was done for the first time.

The fourth material considered is nanostructured composite of inorganic nanoparticles dispersed in polymeric matrix. The objective of the work is the fabrication and engineering of transparent bulk nanocomposite where the nanoparticles are very homogeneously dispersed into the matrix. For this part of the thesis, we studied and developed a method for the fabrication of PMMA-ZnO hybrid materials and evaluated the effectiveness of this material for UV absorption and UV shielding.

### 1.3 Thesis Organization

This thesis is organized as a collection of individual chapters and includes five scientific papers presented for publication in peer reviewed journals. The main emphases of this dissertation are realizing high quality hybrid nanostructures and the development of performance enhanced development of fuel cells, optoelectronic and sensing devices, and electrocatalytic systems. Chapters two, three, four, five and six are the scientific papers. Starting the thesis by giving a background and motivation, and objectives highlighted by the author, the chapters of this thesis are organized as below:

Chapter 2, *synthesis and characterization of ZnO/Ag core-Shell nanocomposites*, is already published in Journal of Alloys and Compounds. This chapter emphasizes on the synthesis of ZnO nanorods and the coating of Ag nanoparticles on the surfaces of ZnO nanorods through a cationic surfactant CTAB. CTAB was used for the first time to coat ZnO nanorods. The as-prepared core-shell nanomaterials shows some good properties related to optical phenomenon.

Chapter 3, *synthesis and characterization of octahedral and spherical nanocrystals on graphene oxide for electrocatalytic applications of methanol oxidation reaction*, is intended for publication in Advanced Material Letters and deals with the shape controlled synthesis of Pd nanocrystals supported on graphene oxide and its electrocatalytic performance towards methanol oxidation reaction.

Chapter 4, *preparation and characterization of Pd-Pt bimetallic alloy on graphene oxide and its electrocatalytic properties*, is already published in the Journal of Power Sources. This chapter deals with the preparation of Pd-Pt bimetallic alloy supported on graphene oxide with a reducing gas CO. The bimetallic were characterized for electrocatalytic applications related methanol oxidation reaction, oxygen reduction reaction and methanol tolerant oxygen reduction reaction.

Chapter 5, *synthesis and characterization of MoS<sub>2</sub>/GO-CNT composite for electrocatalytic applications of hydrogen evolution reactions*, is intended for publication in Nano Research and deals with the preparation of ternary MoS<sub>2</sub>/GO-CNT composite and its electrochemical performance towards hydrogen evolution reactions.

Chapter 6, *synthesis and characterization of ZnO/PMMA polymer nanocomposites*, is already published in Applied Physics A. This chapter focuses on the synthesis of solution mixing method of ZnO nanoparticles in the PMMA matrix through a solvent DMAc. The as-prepared polymer nanocomposite was studied for its optical and thermal properties.

#### 1.4 References

1. A. R. Tao, S. Habas, P. Yang, *Small*, 4, 310 (2008).
2. Y. N. Xia, Y. J Xiong, B. Lim, S. E Skrabalak, *Angew. Chem., Int. Ed.*, 48, 60 (2009).
3. T. K. Sau, A. L. Rogach, *Adv. Mater.*, 22, 1781 (2010).
4. T. K. Sau, A. L. Rogach, F. Jackel, T. A. Klar, J. Feldmann, *Adv. Mater.*, 22, 1805 (2010).
5. J. Gao, G. Liang, J.S. Cheung, Y. Pan, Y. Kuang, F. Zhao, B. Zhang, X. Zhang, E.X. Wu, B. Xu, *J. Am. Chem. Soc.* 130 (2008) 11828-11833.
6. J. Twidell, T. Weir, *Renewable Energy Resources*, E & FN SPON, London, 1998.
7. T.D. Jarvi, E.M. Stuve, in: *Electrocatalysis*, J. Lipkowski, P.N. Ross (Eds.), Wiley-VCH, New York, 1998, pp. 75-154.
8. J.M. Feliu, E. Herrero, in: *Handbook of Fuel Cells - Fundamentals, Technology and Applications*, W. Vielstich, H.A. Gasteiger, A. Lamm (Eds.), Vol 2 *Electrocatalysis*, John Wiley & Sons, Chichester, 2003, pp. 625-634.
9. S.-G. Sun, in: *Electrocatalysis*, J. Lipkowski, P.N. Ross (Eds.), WileyVCH, New York, 1998, pp. 243-291.
10. N. Kosaric, J. Velikonja, *FEMS Microbiology Reviews* 16 (1995) 111.

11. R. Bardhan, Mukherjee, S.; Mirin, N. A.; Levit, S. D.; Nordlander, P.; Halas, N. J. *J. Phys. Chem. C* 2010, 114, 7378.
12. C. Radloff, Halas, N. J. *Nano Lett.* 2004, 4, 1323.
13. S. Wang, Jarrett, B. R.; Kauszarich, S. M.; Louie, A. Y. *J. Am. Chem. Soc.* 2007, 129, 3848.
14. H. Wang, Brandl, D. W.; Nordlander, P.; Halas, N. J. *Acc. Chem. Res.* 2007, 40, 53.
15. X. H. Xia, T. Iwasita, F. Ge, W. Vielstich, *Electrochim. Acta*, 41 (1996) 711.
16. Sriramulu, S., Jarvi, T. D., Stuve, E. M., *J. Electroanal. Chem.*, 467 (1999) 132.
17. G. A. Planes, J.L. Rodriguez, E. Pastor, C. Barbero, *Langmuir*, 19 (2003) 8137.
18. D. Cao, G.Q. Lu, A. Wieckowski, S.A. Wasileski, M. Neurock, *J. Phys. Chem. B*, 109 (2005) 11622.
19. J. Jiang, A. Kucernak, *J. Electroanal. Chem.*, 533 (2002) 153.
20. N. Porter, H. Wu, Z. Quan, J. Fang, *Acc. Chem. Res.* 46 (2013) 1867-1877.
21. M. Debe, *Nature* 486 (2012) 43-51.
22. J. Wu, P. Li, Y. Pan, S. Warren, X. Yin, H. Yang, *Chem. Soc. Rev.* 41 (2012) 8066-9074.
23. M. Liu, R. Zhang, W. Chen, *Chem. Rev.* 114 (2014) 5117-5160.
24. B. Lim, M. Jiang, P. Camargo, E. Cho, J. Tao, X. Lu, Y. Zhu, Y. Xia, *Science* 324 (2009) 1302-1305.
25. Li, Y.; Wang, H.; Xie, L. M. Liang, Y.; Hong, G.; Dai, H. *J. Am. Chem. Soc.* 2011, 133, 7296-7299.
26. Zheng, Y.; Jiao, Y.; Zhu, Y. H.; Li, L. H.; Han, Y.; Chen, Y.; Du, A. J.; Jaroniec, M.; Qiao, S. Z. *Nat. Commun.* 2014, 5, 3783.
27. Hou, Y. D.; Laursen, A. B.; Zhang, J. H.; Zhang, G. G.; Zhu, Y. S.; Wang, X. C.; Dahl, S., Chorkendorff, I. *Angew. Chem. Int. Ed.* 2013, 52, 3621-3625.
28. Laursen, A. B.; Kegnaes, S.; Dahl, S., Chorkendorff, I. *Energy Environ. Sci.* 2012, 5, 5577- 5591.

## Chaper 2 Synthesis and Characterization of ZnO/Ag Core-Shell Nanocomposites

### 2.1 Introduction

Hybrid nanostructures have induced substantial interest during the last era, more importantly because of the probability that this new type of system deals with the design of materials with advanced and excellent physical chemistry properties [1-5]. The beauty of hybrid nanostructures is that numerous functions can be combined into one system for specific uses [6-7]. In addition, the interactions at the nanoscale between different components can greatly enhance the whole application performance of the nanostructured system and even form innovative synergistic properties. These kinds of hybrid nanostructure materials usually composed of a semiconductor and a noble metal are of pronounced importance, because of their innovative physical and chemical properties, in addition they offer the chance to modify the optical system, including absorption and emission phenomena, and the concentration of electromagnetic radiations [8-10]. These properties allow the nanocomposite to be used in the advancement of optoelectronic and sensing devices and in the miniaturization of photovoltaic and photocatalytic systems [11-13].

Among the best renowned semiconductor materials used in hybrid nanostructures is Zinc Oxide (ZnO). It is a semiconductor with a wide bandgap of 3.37 eV, a huge exciton binding energy of 60 meV and outstanding radiation hardness [14]. The present theoretical and experimental work specified to ZnO nanostructures is apprehensive with the improvement of its optical properties. Various nanostructures of ZnO also exhibit piezoelectricity, transparent conductivity, and ferromagnetic and gas sensing properties [15-17]. These features are strongly dependent on the size, shapes, crystallinity, doping and surface modification of ZnO nanostructures as reported by various authors in the literature. For that reason, different structures of ZnO on the micro and nanoscale level have been prepared, for example nanoparticles, nanotubes, nanorods, nanowires, and other morphologies, via sol-gel, hydrothermal, template, thermal decomposition, physical sputtering, chemical bath deposition and etc. [18-23]. Among the most famous noble metal materials extensively used in hybrid nanostructures is silver (Ag). The incorporation of Ag nanoparticles together with ZnO nanorods can offer exceptional properties in electronic, optical, and thermal systems [24-26].

Currently, there have been many reports on the synthesis of ZnO NRs/Ag nanocomposites by coating ZnO with either a metal nanoparticle or a dielectric layer, the

near-band-gap emission (NBE) intensity can be either improved [24-27], or quenched [28,29]. Especially, direct metal covering seems to be an effective way of enhancing the NBE due to surface plasmon coupling [24-27]. Numerous metals have been verified to be able to enhance the NBE emission of ZnO [24-27]. Though, plenty of contrary results have also been shown in the literature about the influence of metals on the NBE emission of ZnO. For instance, Cheng *et al.*, [30] reported the boosted NBE luminescence of ZnO nanorods after capping Au nanoparticles, while Lai *et al.*, [31] disclosed that Au had a trivial effect on the emission enhancement of ZnO film. Richters *et al.*, [32] experimentally observed that the deposition of five different metals on ZnO nanowires would all shrink their comparative intensity of NBE emission. These unpredictable results show that the mechanism behind the luminescence improvement or detracting of metal coated ZnO is reasonably complicated. In most of the circumstances, the NBE emission enhancement of ZnO can be ascribed to the coupling between surface plasmons of metals and excitons of ZnO [30,31]. Many other aspects, however, have also been testified to take impact in some circumstances, for example the diffusion of metals into ZnO [33], the spontaneous hydrogen incorporation in ZnO [32], and the separation space between ZnO and metals [29].

However, most of these reports emphasize on the physical methods to make vertical aligned ZnO nanorods from the seeds of ZnO thin films coated with Ag nanoparticles. Amongst the chemical method applied, Mahanti *et al.*, reported the synthesis of Ag nanoparticles spin coated on vertically grown ZnO nanorod arrays and found a 10-times improvement in the near band edge emission [34]. Hong *et al.*, integrated Ag nanoparticles with uniform size distribution, which were synthesized by using trisodium citrate as a capping agent, on ZnO thin films through photochemical solution deposition technique [24]. It was reported that the electrical resistance increases and transmittance decrease for the composite film. Recently, Li *et al.*, prepared ZnO/Ag core-shell nanocomposites through the pre-activation of ZnO nanorods and the nucleation and subsequent growth of Ag nanoparticles on the surfaces of ZnO nanorods [35]. It was found that the photoluminescence spectra of the ZnO/Ag core-shell nanocomposite were absolutely quenched.

In this chapter, we emphasize on the development of a simplistic solution based method to synthesize ZnO/Ag core-shell nanocomposite through a cationic surfactant CTAB, and predominantly investigate the structural, morphological and optical properties of the as-prepared core-shell nanocomposites. In this technique, we initially, apply the cationic surfactant CTAB to overcome the poor dispersion of ZnO nanorods (NRs) in an aqueous solution and afterwards attain uniform deposition of Ag nanoparticles on ZnO nanorods in a

controlled environment. The morphological, structural and optical properties of ZnO NRs/Ag nanocomposite with an altered concentration of AgNO<sub>3</sub> and CTAB, and after annealing at 200 °C were examined. In our results, we found out that Ag nanoparticles were homogeneously coated on ZnO nanorods with a 0.09 mmol of CTAB and 0.7 mmol of AgNO<sub>3</sub> concentration. The subsequent UV absorption has red-shifted and NBE is suppressed, and deep level emission (DLE) is reduced, showing the strong interfacial contact between the Ag nanoparticles and ZnO nanorods.

## 2.2 Experimental Details

### 2.2.1 Synthesis of ZnO Nanorods

ZnO nanorods were synthesized via a typical hydrothermal process using ZnCl<sub>2</sub> as a precursor material for initiating the chemical reaction. This solvothermal process was already reported by Zhu *et al.*, [36]. In a typical chemical route, 0.64g of ZnCl<sub>2</sub> and 0.50 g of N<sub>2</sub>H<sub>4</sub>.H<sub>2</sub>O were mixed in 90 mL of deionized (DI) water under continuous stirring. After some time, slurry like white precipitate was formed promptly. After 15 minutes of continuous stirring the mixture was transferred to a 100 mL Teflon-lined stainless steel autoclave and was sealed. The autoclave was well-maintained at 165 °C for 24 hours and gradually cooled down to room temperature. Subsequently opening the lid of the autoclave, a white precipitate was formed at the bottom of the autoclave. The final product was centrifuged two times and washed with alcohol and DI water various times, and was air-dried in an oven at 80 °C.

### 2.2.2 Preparation of ZnO NRs/Ag core-shell nanocomposite

In a typical synthesis, 0.8 mmol of ZnO nanorods were dispersed in 50 mL DI water using ultrasonication for 30 minutes. After ultrasonication, 0.09 mmol of CTAB was dissolved in the above solution under constant continuous stirring. The solution was heated to 45 °C under constant magnetic stirring and cooled down to room temperature slowly. At room temperature, a 25 mL aqueous solution of 0.8 mmol of AgNO<sub>3</sub> was gradually added dropwise to the ZnO nanorods-CTAB suspension under continuous magnetic stirring for 1 hour. In the last step, a 25 mL aqueous solution of 0.9 mmol of NaBH<sub>4</sub> was added directly to the above solution under continuous magnetic stirring to reduce the Ag nanoparticles. The solution was centrifuged two times, and washed with alcohol and DI water and dried out overnight in an oven at 70 °C. The sample having 0.8 mmol of ZnO NRDs, 0.8 mmol of AgNO<sub>3</sub> and 0.09 mmol of CTAB was labelled as ZnO NRs/Ag-1. The concentration of AgNO<sub>3</sub> was increased to 1.6 mmol while the concentration of CTAB was held constant for

the sample named as ZnO NRs/Ag-2. In order to strengthen the bond between Ag nanoparticles and to improve the crystallinity of the sample named ZnO NRs/Ag-1, it was annealed at 200 °C for 1 hour.

### 2.2.3 Characterization Tools

The prepared samples were structurally characterized and investigated by scanning electron microscope (SEM) and field emission SEM (FESEM) equipped with EDX, transmission electron microscope (TEM), high resolution TEM (HRTEM) and powder X-ray diffraction (XRD). The surface morphology of the samples was examined by using field emission scanning electron microscope (FESEM, JEOL, JSM-6700F). The Compositional analysis and concentration of elements were achieved by energy dispersive X-ray spectroscopy (EDX) attached with FESEM. The microstructure, morphology and electron diffraction pattern of the products was also studied by transmission electron microscope (HRTEM, JEM-2010). For TEM analysis, the powder was dispersed in ethanol and ultrasonicated for 10 to 15 mins. A few drops from this solution were put down on the carbon coated copper grid. The X-ray diffraction (XRD) patterns of the products were recorded using Rigaku powder X-ray diffractometer with  $\text{CuK}\alpha_1$  source ( $\lambda=0.15405$  nm) in  $\theta$ -2 $\theta$  configuration. Room temperature optical absorption spectra in the UV and visible wavelength regions were recorded on a Shimadzu spectrophotometer (SOLID3700) by dispersing the samples in ethanol. Photoluminescence (PL) emission spectra and Raman spectra were examined using Nd-YAG laser with a 325 nm excitation source and recording the luminescence with a spectrometer together with a photomultiplier tube.

## 2.3 Results and Discussion

### 2.3.1 Morphology and Mechanism

A facile solution based synthetic route is applied to produce hybrid ZnO NRs/Ag core-shell nanocomposite under ambient conditions. The formation of ZnO NRs/Ag core-shell nanocomposite is based on the nucleation and growth of Ag nanoparticles through a cationic surfactant CTAB and by the reduction of  $\text{AgNO}_3$  on the selective and suitable surface sites of ZnO nanorods. As a typical cationic surfactant, CTAB molecule has a positively charged oleophilic head group and a long hydrophilic tail, and it can form micelles at 33 °C in water [37]. Micelles can stabilize the substrates, intermediates or products through hydrophobic, electrostatic, hydrogen bonding and Van der Waals forces [38]. In our case, we have found that

CTAB can efficiently disperse ZnO nanorods and also serve as a soft template for Ag nanoparticles (Figure 2.1) [39]. Moreover, the role of CTAB can be explained by the incorporation of silver nanoparticles onto the surface of CTAB micelles, which could slowly form  $\text{Ag}^+/\text{CTAB}$ ,  $\text{AgBr}/\text{CTAB}$ , and  $\text{AgBr}$  structures through their quaternary ammonium groups [40,41], and then the reduction of  $\text{Ag}^+$  ions occur through  $\text{NaBH}_4$ . The concentration of both the capping molecules and reactive  $\text{Ag}^+$  will have a great effect on tuning the size and density of the deposited Ag nanoparticles. Under a condition where a smaller number of CTAB molecules cap the ZnO nanorods or higher concentrations of volatile  $\text{AgNO}_3$  are present, the abundant  $\text{Ag}^+$  ions have easy access to the ZnO nanorod surface, which promotes nuclei formation and further particle growth. In the present case, we have only used 0.09 mmol of CTAB and 0.7 mmol of  $\text{AgNO}_3$ . As the concentration of CTAB molecules increases up to 2 mmol, no signs of Ag nanoparticle coating on ZnO nanorods were observed (Figure 2.2c and 2.2d). This result indicates that as the concentration of CTAB molecules increases beyond 0.09 mmol, it can only stabilize Ag nanoparticles and there is also a great influence occurred in the particle size of Ag nanoparticles. ZnO NRs/Ag nanocomposite was also prepared without using CTAB, and systematic investigations were carried out using FESEM technique. As expected, no signs of Ag nanoparticles coating were observed in the system without using CTAB as shown in Figure 2.2a and 2.2b.

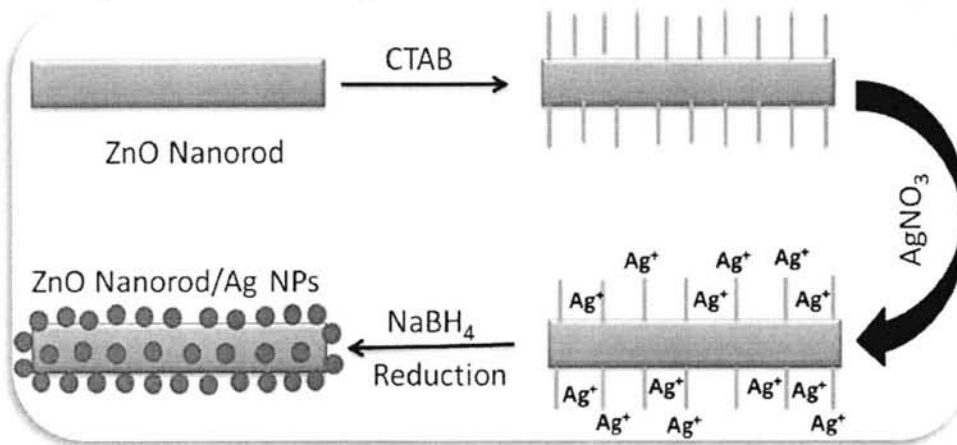


**Figure 2.1** Schematic representation of the synthesis of ZnO NRs/Ag core-shell nanocomposites.

The formation of Ag nanoparticles coated on ZnO nanorods is also observed from SEM, FESEM and TEM images. The SEM studies depicted in Figure 2.3a and 2.3b indicated that the morphology of hydrothermally grown ZnO is rod shaped. Figure 2.4a and 2.4b shows typical TEM images of uncoated ZnO nanorods with an average diameter of about 50 nm and a length of 500 nm, with smooth surfaces. Moreover, Figure 2.4b show typical TEM image of



an individual nanorod. The inset of Figure 2.4 shows SAED pattern of the uncoated ZnO nanorods and expose that the obtained ZnO nanorod exhibits single crystal with (002) growth direction along the c-axis and can be indexed as the hexagonal ZnO phase, which is in good agreement with XRD results shown in Figure 2.7. High-resolution TEM (HRTEM) image of a single ZnO nanorod shown in Figure 2.5a reveals that the ZnO nanorods are structurally uniform and well-oriented lattice fringes of interplanar spacing is 0.25 nm, which corresponds to the (101) plane of ZnO nanocrystal.

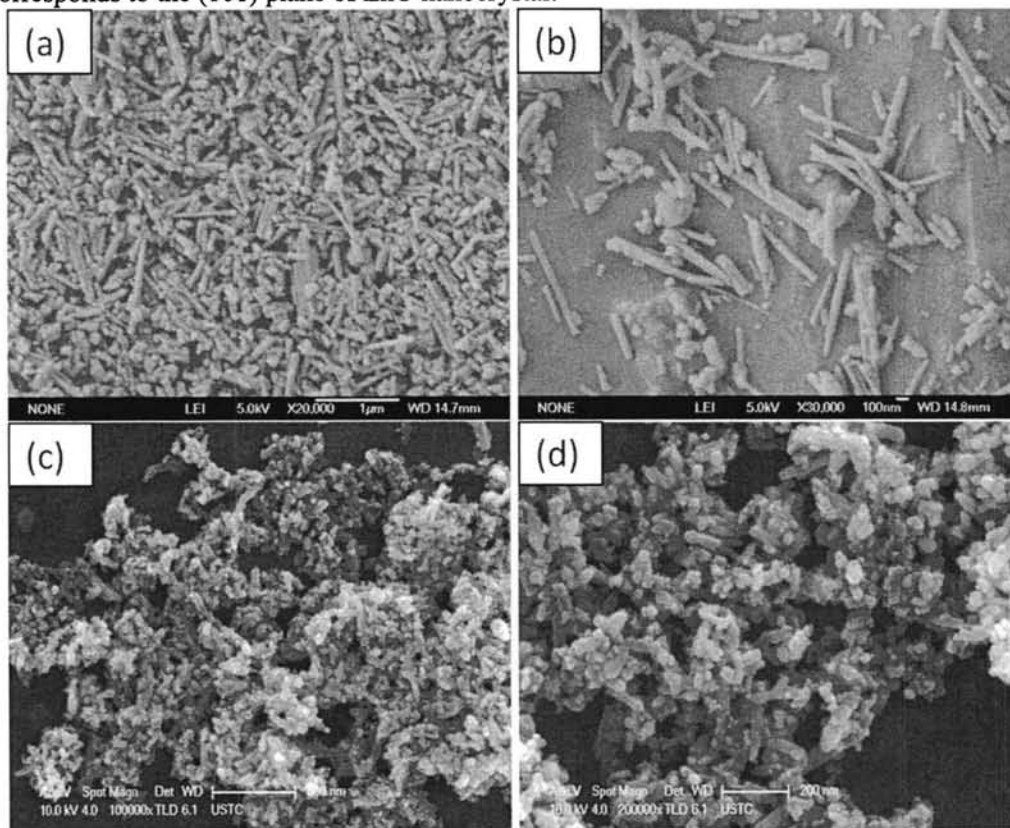


**Figure 2.2** SEM and FESEM images of ZnO NRs/Ag nanocomposite obtained (a) and (b) without using CTAB (c) and (d) with 2 mmol of CTAB.

Figure 2.3c-d and Fig. 2.4c-d show the FESEM and TEM images of Ag coated ZnO nanorods. Low magnification FESEM image of ZnO NRs/Ag-1 nanocomposite is illustrated in Figure 2.3c, where ZnO nanorods are uniformly coated with Ag nanoparticles. The uniform coating is basically composed of a large number of spherical Ag nanoparticles with different sizes, ranges from 10 to 30 nm. The average diameter of the Ag nanoparticle is about 20nm. High magnification FESEM image shows that the surface of the ZnO nanorods became rough after the Ag nanoparticles shell growth. Figure 2.3e and 2.3f shows that most

of the ZnO nanorods appeared to be uncovered with the increase in the concentration of Ag nanoparticles, which indicates the poor interfacial interaction between ZnO nanorods and Ag nanoparticles.

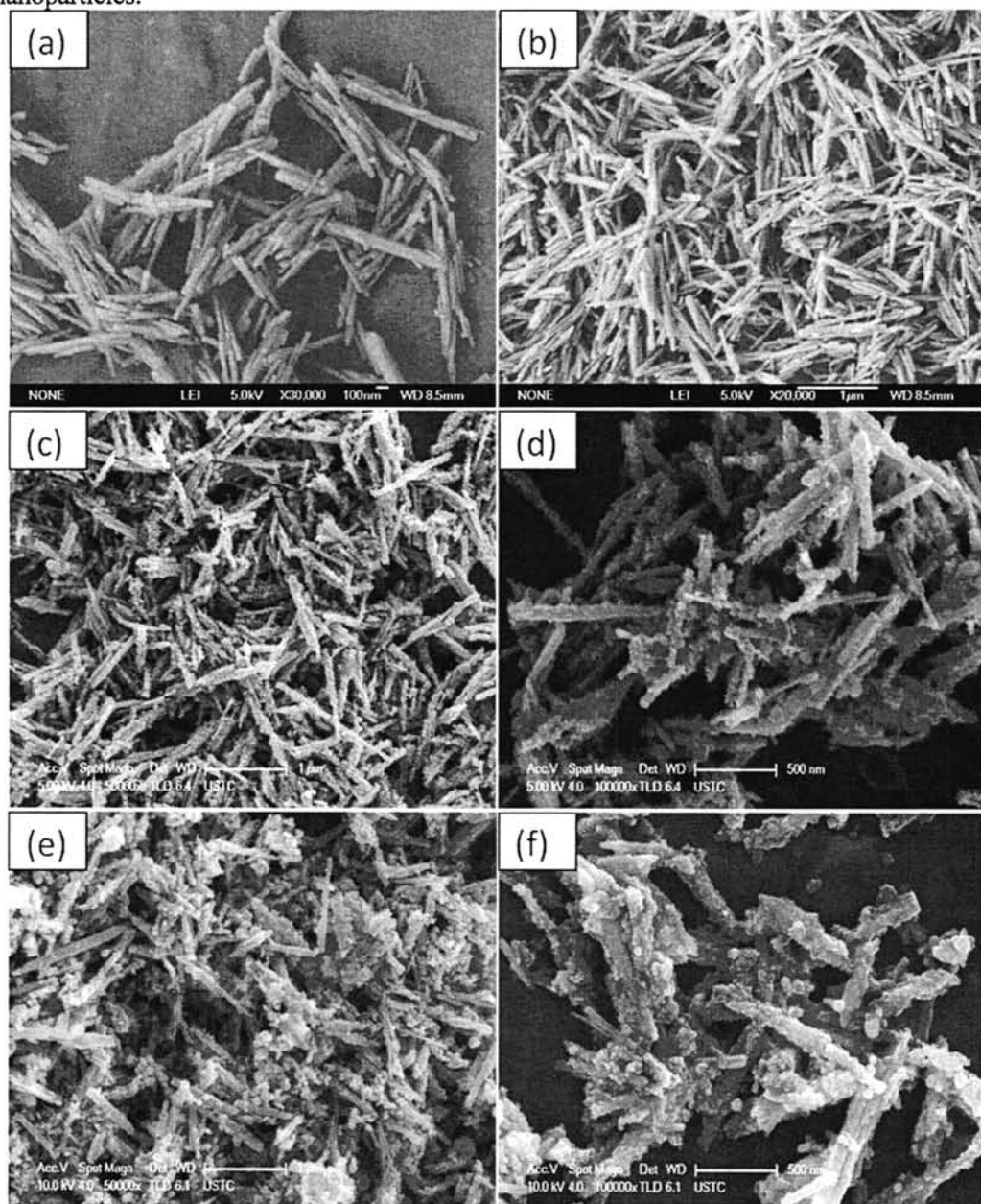


**Figure 2.3** Low and high magnification SEM and FESEM images of (a) and (b) ZnO NRs, (c) and (d) ZnO NRs/Ag-1 and (e) and (f) ZnO NRs/Ag-2.

The TEM images shown in Figure 2.4c and 2.4d further confirm the shell growth of Ag nanoparticles shown in FESEM images. The apparent contrast in the TEM image between

ZnO core and the Ag nanoparticle shell offers evidence for the formation of ZnO NRs/Ag nanocomposite. The images show that Ag nanoparticles are uniformly coated on ZnO nanorods in different sizes. By comparison with Figure 2.4c, the ZnO nanorod appeared much blacker and shadier in contrast than the uncoated ZnO nanorods, which is characteristic of the existence of Ag nanoparticles partially or entirely covered on ZnO nanorods surface.

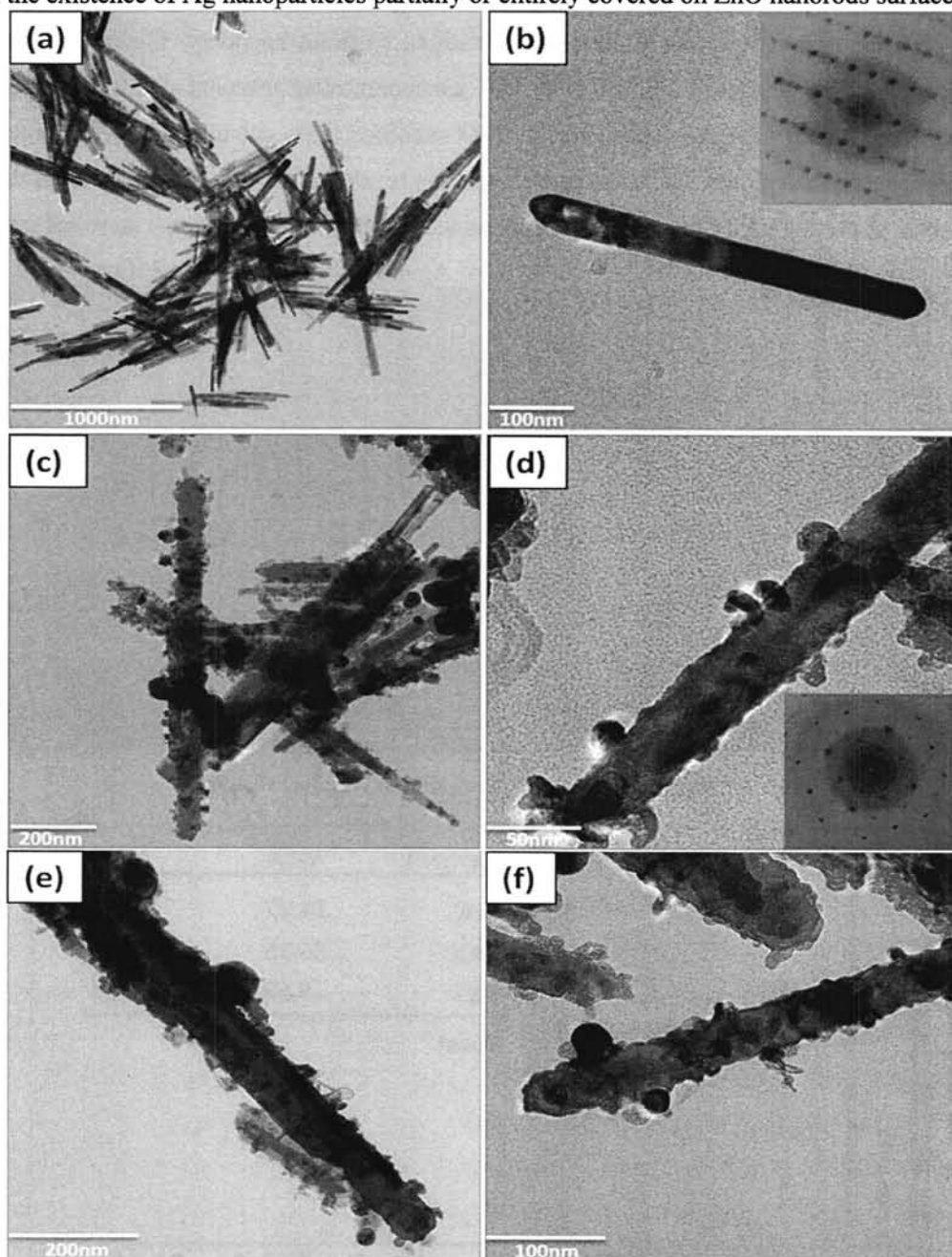


**Figure 2.4** TEM images of (a) and (b) ZnO NRs, (c) and (d) ZnO NRs/Ag-1 and (e) and (f) ZnO NRs/Ag-1 annealed at 200 °C.

The HR-TEM image shown in Figure 2.5b again confirms the sharp interface between ZnO nanorod core and the shell of Ag nanoparticles. The periodicity of the lattice fringes obtained for the core is  $d=0.25$  nm, corresponding to the (101) planes of hexagonal ZnO, and for the shell is  $d=0.236$  nm, corresponding to the (111) planes of the metallic Ag with FCC crystal structure. Obviously, the lattice fringes of the two adjacent nanorod and nanoparticle show different orientations and are interjected with an apparent boundary. Figure 2.4e and 2.4f show the TEM images of the ZnO NRs/Ag-1 nanocomposites annealed at  $200^{\circ}\text{C}$ . As can be seen, the coating of Ag nanoparticles on ZnO nanorods turns out to be denser, and the particles become more quenched after annealing. This result can also be confirmed from the XRD data, as the crystallite size decreases after annealing, the particles become more reduced in their size. This represents still better adhesion of Ag nanoparticles with the ZnO nanorods.

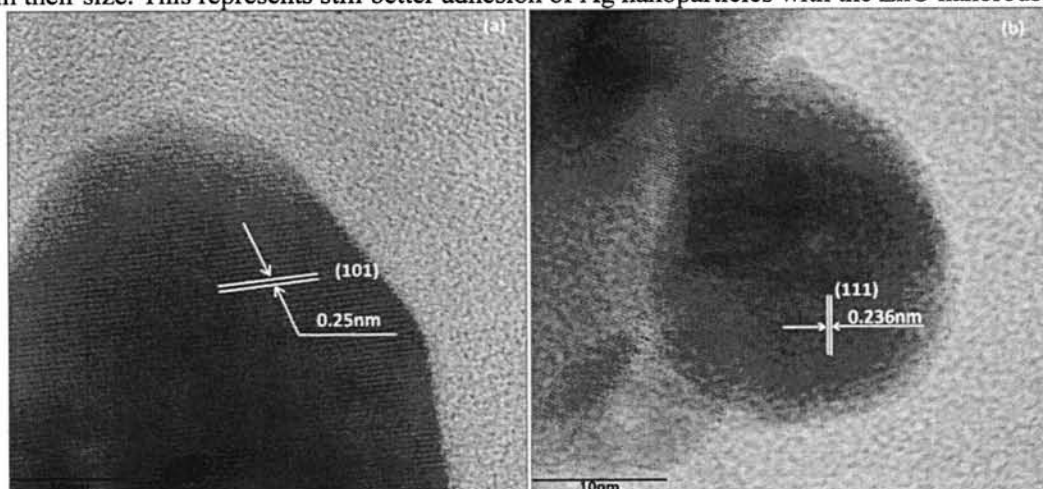


Figure 2.5 HRTEM images of (a) ZnO NRs and (b) ZnO NRs/Ag-1.

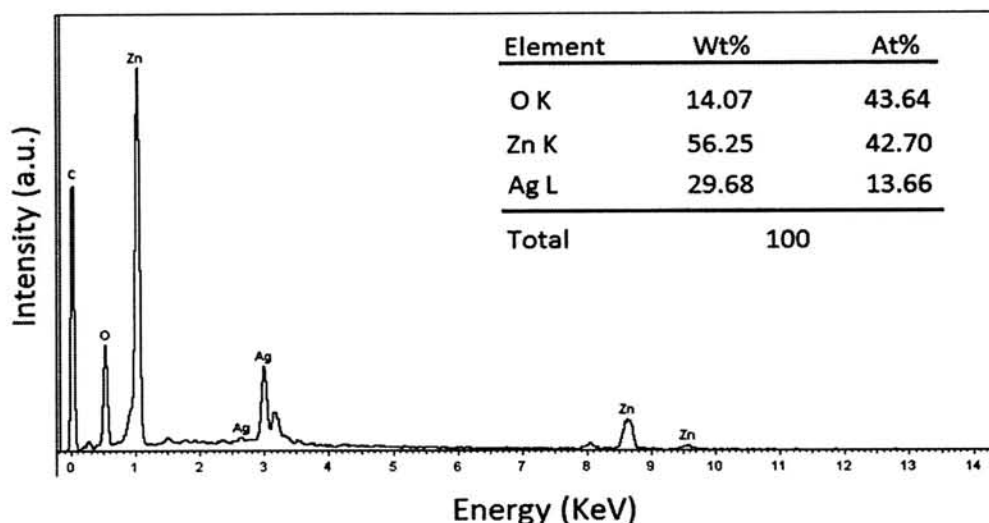


Figure 2.6 EDX spectra of ZnO NRs/Ag-1 nanocomposite.

The elemental composition of the ZnO NRS/Ag-1 nanocomposite was carried out using EDX integrated with FESEM instrument as expected in Figure 2.6. From EDX measurements, it can be seen that zinc, oxygen and silver are present in the core-shell nanocomposite. The composition of Ag in the ZnO-NRs/Ag-1 nanocomposite is 13.66 at.% of the total elements. The identified carbon and copper elements come from the amorphous carbon coated copper grids.

### 2.3.2 Structural Characterization

The structural and crystalline phases of pure ZnO nanorods and ZnO NRs/Ag core shell nanocomposites were identified by X-ray diffraction studies. Figure 2.7a and 2.7b show the XRD patterns of pure ZnO nanorods, ZnO NRs/Ag-1, ZnO NRs/Ag-2 and annealed ZnO NRs/Ag-1 nanocomposite. The XRD pattern of pure ZnO nanorods shows a highly crystalline hexagonal wurtzite structure of ZnO with a lattice constant of  $a=3.245$  and  $c=5.197$  (JCPDS card no. 36-1451). In the XRD pattern of ZnO NRs/Ag core-shell nanocomposite, diffraction peaks at  $2\theta=31.75$  (100),  $34.39$  (002),  $36.25$  (101),  $47.61$  (102),  $56.61$  (110),  $62.88$  (103),  $66.37$  (200),  $67.99$  (112), and  $69.11$  (201) corresponding to the hexagonal wurtzite structure of ZnO nanorods, while additional peaks at  $2\theta=38.150$  (111),  $44.430$  (200),  $64.540$  (220) and  $77.510$  (311) clearly indicate the existence of the face centered cubic (FCC) phase of the silver shell. Their diffraction angle positions and relative intensities are in good agreement with the JCPDS card no. 4-0783 of bulk silver, which proves the formation of crystalline Ag nanoparticles. As the concentration of Ag is increased, the relative intensity of the diffracting plane (111) also increased, and the relative intensity of the pure ZnO diffracting plane (101) decreased, which suggests that Ag nanoparticles coating can depress the intensities of high intensity peaks of pure ZnO nanorods. Figure 2.7b shows the diffraction pattern of annealed ZnO NRs/Ag-1 at  $200\text{ }^{\circ}\text{C}$ . The relative intensity of the diffracting planes at (111), (200), (220) and (311) increased after annealing, which indicates that the crystallinity of Ag nanocrystals had been improved to some extent.

The average crystallite size is calculated from the XRD pattern using the Scherer's equation <sup>[42]</sup> (Equation 2.1) with the integral widths corrected with the standard Si sample (Equation 2.2) using the Cauchy-Lorentzian fit. The crystallite size was calculated from the average of the high intensity peaks (100), (002) and (101) of the hexagonal phases of ZnO and high intensity peak (111) of face centered cubic phase of Ag.

$$L = 0.9\lambda/\beta_{hkl}\cos\theta \quad 2.1$$

where,  $L$  is the average crystallite size,  $\lambda$  is the wavelength (0.15405 nm) of Cu  $K_{\alpha 1}$  radiation,  $\beta_{hkl}$  is the instrumental corrected FWHM in radians and  $\theta$  is the scattering angle in degree. The corrected instrumental broadening for Lorentzian is given by

$$\beta_{hkl} = \beta_{measured} - \beta_{instrumental} \quad 2.2$$

The calculated crystallite size of pure ZnO nanorods estimated around 41nm and that of Ag nanoparticles were found to be 31 nm. As the concentration of Ag is increased the crystallite size increases and reaches its maximum value of 44 nm for ZnO NRs/Ag-2 sample. It is also found that the average crystallite size increased with annealing temperature, from 31 nm to 37 nm when the sample was annealed to 200 °C.

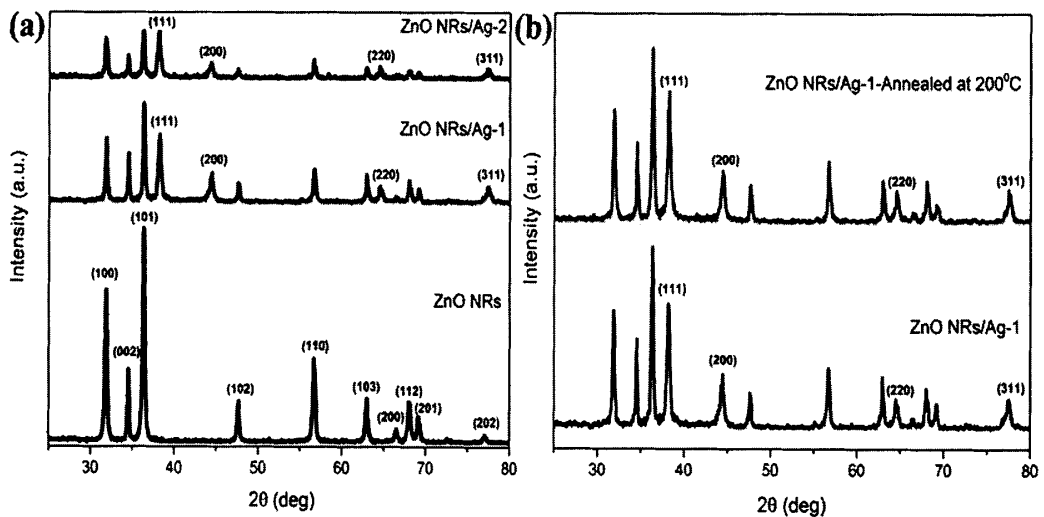


**Figure 2.7** (a) XRD patterns of pure ZnO NRs, ZnO NRs/Ag-1 and ZnO NRs/Ag-2 nanocomposites, and (b) XRD patterns of ZnO NRs/Ag-1 nanocomposite annealed at 200 °C.

We have measured the Raman spectra in order to investigate the influence of Ag nanoparticles on the Raman scattering of ZnO nanorods and whether any extra peak of Ag exists in the Raman spectra of ZnO NRs/Ag nanocomposite. The Raman scattering spectra of ZnO nanorods is shown in Figure 2.8 with a 325 nm laser light (Nd:YAG), as an excitation source. The Raman signals are very sensitive to the structure of the crystal as well as to the defects in the crystal structure. The crystal structure of ZnO is wurtzite (hexagonal) with  $C_{6v-4}(P63mc)$  point group symmetry and group theory predicts that there are two  $A_1$ , two  $E_1$ , two  $E_2$  and two  $B_1$  modes, where two  $B_1$  modes are not Raman active and the other six modes are Raman active [43]. From the Figure 2.8, the peak at  $439.6\text{ cm}^{-1}$  and  $99.5\text{ cm}^{-1}$  can be ascribed to high and low  $E_2$  mode. The peak at  $334.7\text{ cm}^{-1}$  is the second order Raman spectrum originating from the zone boundary phonons  $3E_{2H}-E_{2L}$  and the peak at  $380.6\text{ cm}^{-1}$  can be labeled as  $A_{1T}$ . It is clear from the Figure 2.8 that  $A_{1L}$  mode and  $E_1$  (low) mode at

575.5  $\text{cm}^{-1}$  and 588.3  $\text{cm}^{-1}$ , respectively, are also observed but its intensity is very low. The  $A_{1L}$  mode is commonly associated with the oxygen vacancies, zinc interstitial and surface defect complexes containing oxygen vacancy and zinc interstitial in ZnO nanostructures<sup>[44]</sup>.

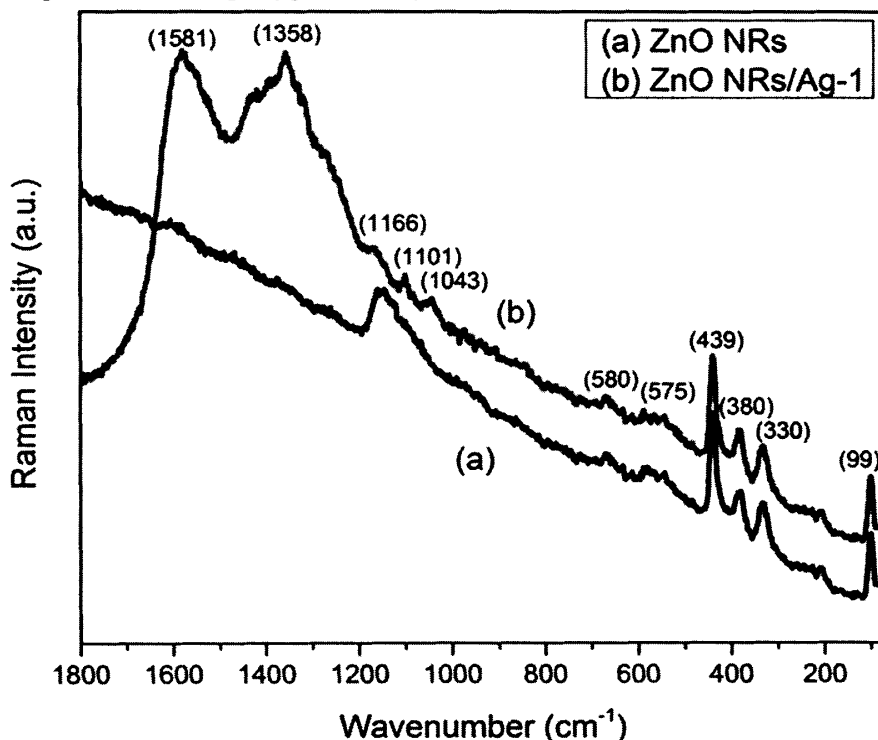


**Figure 2.8** Raman spectra of the pure ZnO NRs and ZnO NRs/Ag-1 nanocomposite.

The Raman spectrum of ZnO NRs/Ag-1 nanocomposite is also shown in the Figure 2.8. The main dominant peaks of ZnO nanorods at 439  $\text{cm}^{-1}$  and 99  $\text{cm}^{-1}$ , designated as  $E_2$  (high) and  $E_2$  (low), respectively, are also observed in the spectra of ZnO NRs/Ag-1 nanocomposite. The result is consistent with XRD spectra of ZnO NRs/Ag-1 nanocomposite. In addition to the  $E_2$ , the  $A_{1L}$  mode with very low intensity was also observed in the Raman spectra of ZnO NRs/Ag-1 nanocomposite. Since the  $A_{1L}$  mode is related to the defects such as oxygen vacancy and zinc interstitial in ZnO, that is why, the low intensity of  $A_{1L}$  mode indicates that defect level is partly removed, and it is also consistent with the PL spectra shown in Figure 2.10, which shows that the deep level emission (DLE) spectra is suppressed by coating of Ag nanoparticles on ZnO nanorods. The coating of Ag on ZnO nanorods is further confirmed by observing the high-intensity peaks at 1358  $\text{cm}^{-1}$  and 1581  $\text{cm}^{-1}$  in the Raman spectra of ZnO NRs/Ag-1 nanocomposite. Other peaks at 1043  $\text{cm}^{-1}$ , 1101  $\text{cm}^{-1}$  and 1166  $\text{cm}^{-1}$  are also observed, which are related to Ag nanoparticles<sup>[45-47]</sup>.

### 2.3.3 Optical Properties

The optical properties of the obtained ZnO nanorods and ZnO NRs/Ag nanocomposites were monitored using UV-Vis spectroscopy. The optical absorption spectra of pure ZnO nanorods, Pure Ag nanoparticles, ZnO NRs/Ag core-shell nanocomposites and annealed nanocomposites are shown in Figure 2.9 and the detailed values are listed in Table 2.1. It is found that a distinct peak at about 374 nm (3.33 eV) is revealed for pure ZnO nanorods, which is corresponding to the excitonic absorption. The pure Ag nanoparticles prepared through the reduction of AgNO<sub>3</sub> by NaBH<sub>4</sub> shows a broad surface plasmon absorption peak centered at 411 nm (Figure 2.8). The optical absorption spectra of ZnO NRs/Ag-1 nanocomposite and annealed nanocomposite show an excitonic absorption peak at about 377 nm (3.29 eV) and surface plasmon absorption peaks at 443 nm and 418 nm, respectively. This result indicates a red-shift of 3 nm and 32 nm in the excitonic and surface plasmon absorption band edge for the ZnO NRs/Ag-1 sample. While for the annealed sample, a red shift of 3 nm and 7 nm in the excitonic and surface plasmon absorption band edge was observed, which is similar to the previous reports [48]. The reason for the red-shift in the surface plasmon absorption band is due to the strong interfacial coupling between ZnO nanorod and Ag nanoparticle. The UV absorption of ZnO NRs/Ag nanocomposite and annealed nanocomposite also show a red-shift of about 4 nm compared to pure ZnO nanorods, which implies that the size of ZnO nanorods turns larger during synthesis of ZnO NRs/Ag nanocomposites because the absorption shift of pure ZnO is typically associated to their change in sizes [49].

Moreover, the absorption spectra of ZnO NRDs/Ag-2 nanocomposite show an excitonic absorption peak at about 350 nm and surface plasmon peak at 407 nm. This result shows a blue shift of 24 nm and 4 nm in the excitonic and surface plasmon absorption band edge, respectively. The blue-shift in the surface plasmon indicates that there is no interfacial coupling occurs between ZnO nanorods and Ag nanoparticles. This result is also evident from FESEM images of ZnO NRS/Ag-2 nanomposites (Figure 2.2), which clearly shows that Ag nanoparticles are not coated on ZnO nanorods.

Figure 2.10 shows the PL emission spectra of the pure ZnO nanorods and ZnO NRs/Ag nanocomposite and annealed nanocomposite recorded using an excitation at 325 nm. The PL spectra of Pure ZnO nanorods show a strong UV emission at 384 nm (3.23 eV) due to exciton recombination and a broad deep level visible emission (DLE) ranging from 425-625 nm, centered at 498 nm, which is attributed to the recombination between the electrons in a deep defect level or a surface defect level and the holes in the valence band [50,51].



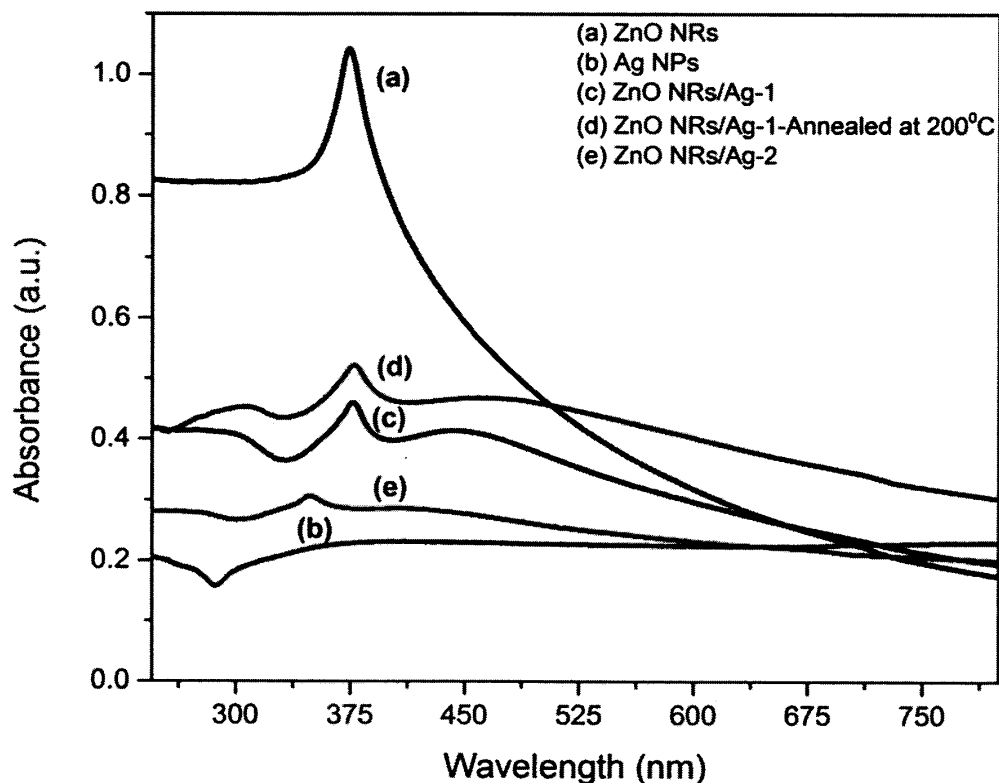


**Figure 2.9** UV-Vis absorption spectra of the pure ZnO NRs, Ag nanoparticles, ZnO NRs/Ag nanocomposites.

**Table 2.1** Optical measurements of ZnO NRs and ZnO NRs/Ag nanocomposites.

Sample Name	Absorbance Band (nm)	Surface Plasmon Band (nm)	PL Band (nm)	
			NBE	DLE
ZnO NRs	374	-	384	498
Ag NPs	-	411	-	-
ZnO NRs/Ag-1	377	443	386	519
ZnO NRs/Ag-1-Annealed at 200 °C	377	418	387	520
ZnO NRs/Ag-2	350	403	383	519

The UV peak position is changed from 386 nm (3.21 eV) for ZnO NRs/Ag-1 and 387 nm (3.20 eV) for annealed nanocomposite (Figure 2.10). Such red-shifts of UV peaks of ZnO have also been reported in the literature<sup>[52-53]</sup>. Lai *et al.*, has observed a red-shift of 3.27 eV to 3.22 eV in the UV peak position when Ag and Au have been used for capping ZnO<sup>[51]</sup>. Recently, Mahanti *et al.*,<sup>[34]</sup> has observed a red-shift of 3.27-3.22 eV in the UV peak position

when Ag was coated on vertically grown ZnO nanorods through a chemical solution based route. A substantial red-shift has also been observed in ZnO/Ag/ZnO thin films<sup>[53]</sup>. The shift is probably due to the strain in the ZnO nanorods as Ag nanoparticles get attached onto the surface of the rods<sup>[53]</sup>. Such strain effect is also observed from our XRD results. ZnO NRs/Ag-1 nanocrystals exhibit absorption in the UV and visible region as shown in Figure 2.9. The absorption edge at about 377 nm is assigned to the absorption of ZnO semiconductor. The absorption peak at 443 nm is the characteristic plasmon absorption of silver nanoparticles in ZnO NRs/Ag-1 nanocrystals, and it is red shifted compared to that of pure ZnO NRs and Ag NPs. It is evident that the red shift in the plasmon absorption is due to the formation of ZnO NRs/Ag nanocomposite. To further evaluate the shifting in the plasmon absorption, we need more in-depth analysis. The plasmon absorption of silver is represented by the following equation:

$$\lambda_p = \left[ \frac{4\pi^2 C^2 m_{eff} \epsilon_0}{(N \cdot e^2)} \right]^{\frac{1}{2}} \quad 2.3$$

where  $m_{eff}$  is the effective mass of the free electron of metal and  $N$  is the electron density of the metal. From equation (2.3), it can be found that for Ag nanoparticles, the position of plasmon absorption is related to the electron density of metallic Ag. When the electron density of the metallic Ag decreases, the plasmon absorption ( $p$ ) will increase accordingly (*i.e.*, the red shift of the plasmon absorption). The plasmon absorption band of the small Ag nanoparticles prepared using  $\text{NaBH}_4$  reduction is around 411 nm. Herein, the red shift of the plasmon peak of silver suggests that the electron density of Ag decreases. The decrease in electron density of the Ag nanocrystals is due to the transfer of electrons from the Ag nanoparticles to the ZnO nanocrystals *via* ZnO-O Ag bonds, which is caused by the work function differences between Ag and ZnO nanocrystals.

For ZnO NRs/Ag-2 nanocomposite the UV emission occurs at 383 nm (3.24 eV), which is blue-shifted compared to pure ZnO nanorods. This blue shift suggests that the coupling between ZnO nanorod and Ag nanoparticle is very weak. This fact is also evident from the absorption spectra (Figure 2.9) and FESEM images (Figure 2.4). It is also clear from the Figure 2.10 that a significant amount of change occurs in the visible emission due to Ag loading under the present experimental conditions. The deep level emission (DLE) spectra are almost suppressed due to Ag loading and annealing of the nanocomposite. On one hand, the deep DLE peaks can be reduced by the surface modification of Ag nanoparticles on ZnO nanorods, while on the other hand, they may also be reduced by the weakening of crystal defects with annealing temperature. But however, the growth of Ag nanoparticles onto the ZnO nanorods suppresses the UV emission spectra in our present experimental conditions, as

shown in the Figure 2.10. This suppression is also evident from the XRD results. After the Ag coating on ZnO nanorods, the intensity of the diffraction peaks of ZnO nanorods decreases. In contrast to our work, literature proposes that UV emission peak is highly enhanced due to loading of Al, Au, Ti and Ag onto ZnO nanorods. However, despite the enhancement in UV emission, literature also proposed that completely detracting of UV emission peak occurs in the work related to Li *et al.*, [35]. Therefore, our method is just a convenient way to coat ZnO nanorods with Ag nanoparticles or to coat any semiconductor with metallic nanoparticles in the future.

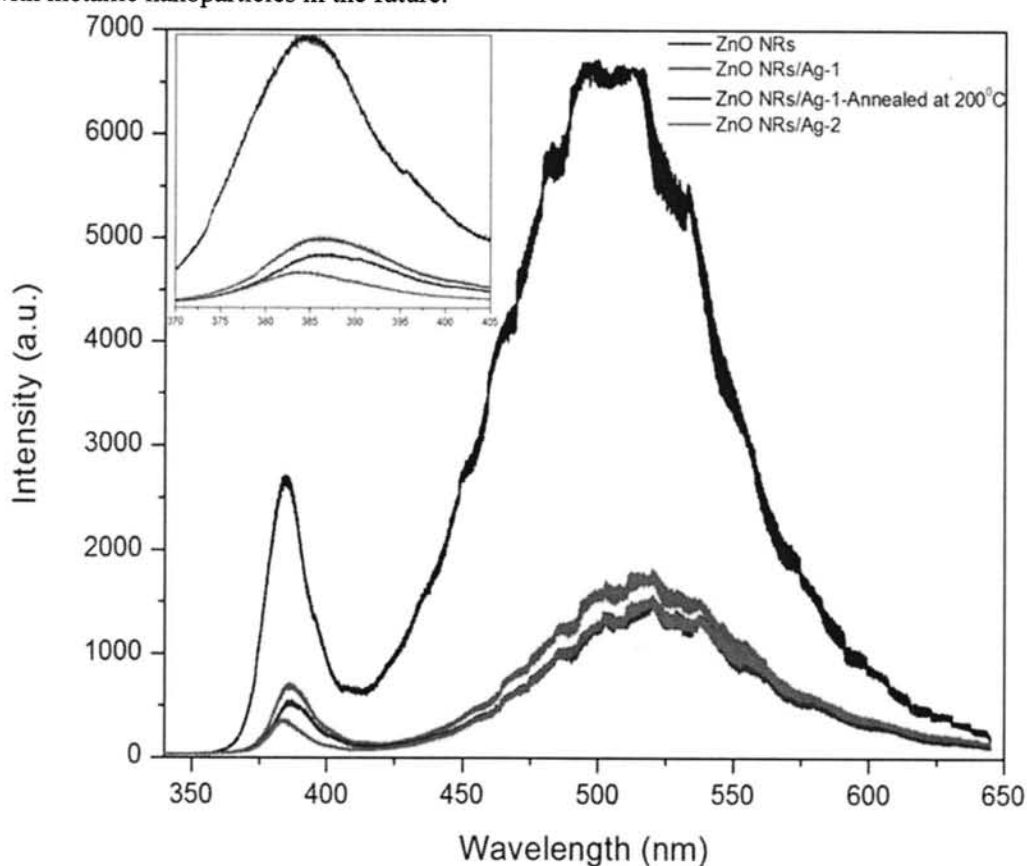


**Figure 2.10** Room temperature photoluminescence (PL) of pure ZnO NRs and ZnO NRs/Ag nanocomposites. Inset shows magnified UV emission spectra.

## 2.4 Summary

In summary, we demonstrated a simple and facile approach for the synthesis of ZnO NRs/Ag core-shell nanocomposites. Comprehensive morphological, structural and elemental analysis confirms the existence of a core made of ZnO nanorod, surrounded by a uniform thin shell of Ag nanoparticles. The formation of Ag nanoparticles coating on ZnO nanorods

occurs through a cationic surfactant CTAB, utilizing only 0.09 mmol. The anneal treatment of ZnO NRs/Ag nanocomposite can improve the crystallinity and bond strength between Ag and ZnO. The concentration of CTAB and precursor material AgNO<sub>3</sub> greatly affects the formation of Ag nanoparticles coated on ZnO nanorods. The obtained nanocomposite, prepared through 0.09mmol of CTAB and 0.7mmol of AgNO<sub>3</sub>, has some red-shifts, showing the strong interfacial interaction between Ag nanoparticles and ZnO nanorods. With the increase of precursor material AgNO<sub>3</sub>, the absorption spectra changes to be blue-shift, revealing no interfacial coupling between ZnO nanorods and Ag nanoparticle. We have also studied the emission properties of ZnO NRs/Ag-1 nanocomposites. The NBE luminescence spectra is red-shifted and suppressed when Ag nanoparticles are coated on ZnO nanorods while a reasonable detractorion also occurs in the deep level emission (DLE) spectra of the nanocomposite. We believe that our synthetic methodology can be further utilized and extended for the preparation of semiconducting metal oxide nanocrystals coated with different metal nanoparticles. Such hybrid nanostructures can be readily used in many applications such as photovoltaics, sensors, optoelectronics, plasmonics and photocatalysis.

## 2.5 References

1. E. Cohen-Hoshen, G.W. Bryant, I. Pinkas, J. Sperling, I. Bar-Joseph, *Nano Lett.* 12 (2012) 4260–4264.
2. R. Costi, A.E. Saunders, U. Banin, *Angew. Chem. Int. Ed. Engl.* 49 (2010) 4878–4897.
3. B.P. Khanal, A. Pandey, L. Li, Q. Lin, W.K. Bae, H. Luo, V.I. Klimov, J.M. Pietryga, *ACS Nano.* 6 (2012) 3832–3840.
4. P. V Kamat, *J. Phys. Chem. Lett.* 3 (2012) 663–672.
5. X. Yin, W. Que, D. Fei, F. Shen, Q. Guo, *J. Alloys Compd.* 524 (2012) 13–21.
6. J. Kim, J.E. Lee, S.H. Lee, J.H. Yu, J.H. Lee, T.G. Park, T. Hyeon, *Adv. Mater.* 20 (2008) 478–483.
7. J. Gao, G. Liang, J.S. Cheung, Y. Pan, Y. Kuang, F. Zhao, B. Zhang, X. Zhang, E.X. Wu, B. Xu, *J. Am. Chem. Soc.* 130 (2008) 11828–11833.
8. M. Achermann, *J. Phys. Chem. Lett.* 1 (2010) 2837–2843.
9. Y. Fedutik, V. Temnov, U. Woggon, E. Ustinovich, M. Artemyev, *J. Am. Chem. Soc.* 129 (2007) 14939–14945.
10. A.O. Govorov, G.W. Bryant, W. Zhang, T. Skeini, J. Lee, N.A. Kotov, J.M. Slocik, R.R. Naik, *NANO Lett.* 6 (2006) 984–994.

11. Q. Xiang, G. Meng, Y. Zhang, J. Xu, P. Xu, Q. Pan, W. Yu, *Sensors Actuators, B Chem.* 143 (2010) 635–640.
12. S. Öztürk, N. Kılınc, Z.Z. Öztürk, *J. Alloys Compd.* 581 (2013) 196–201.
13. P. V Kamat, *J. Phys. Chem. C.* 111 (2007) 2834–2860.
14. U. Ozgur, Y. Alivov, C. Liu, *J. Appl. Phys.* 98 (2005) 041301.
15. T. Mitsuyu, S. Ono, K. Wasa, *J. Appl. Phys.* 51 (1980) 2464.
16. J.M. Baik, J.-L. Lee, *Adv. Mater.* 17 (2005) 2745–2748.
17. Z.L. Wang, *Adv. Mater.* 15 (2003) 432–436.
18. N. Audebrand, J.P. Auffrédic, D. Louër, *Chem. Mater.* 10 (1998) 2450–2461.
19. C.H. Lu, C.H. Yeh, *Ceram. Int.* 26 (2000) 351–357.
20. P. O'Brien, T. Saeed, J. Knowles, *J. Mater. Chem.* 6 (1996) 1135–1139.
21. Z.R. Tian, J.A. Voigt, J. Liu, B. McKenzie, M.J. McDermott, *J. Am. Chem. Soc.* 124 (2002) 12954–12955.
22. L. Guo, Y.L. Ji, H. Xu, P. Simon, Z. Wu, *J. Am. Chem. Soc.* 124 (2002) 14864–14865.
23. S. Komarneni, M. Bruno, E. Mariani, *Mater. Res. Bull.* 35 (2000) 1843–1847.
24. C.S. Hong, H.H. Park, S.J. Wang, J. Moon, H.H. Park, R.H. Hill, *Appl. Surf. Sci.* 252 (2006) 7739–7742.
25. J.T. Lue, W.C. Huang, S.K. Ma, *Phys. Rev. B* 51 (1995) 014570.
26. U. Kreibig, M. Vollmer, *Optical Properties of Metal Clusters*, Springer: Berlin, 1995.
27. M. Mahanti, D. Basak, *J. Lumin.* 145 (2014) 19–24.
28. M. Misra, P. Kapur, M.L. Singla, *Appl. Catal. B Environ.* 150–151 (2014) 605–611.
29. X.D. Zhou, X.H. Xiao, J.X. Xu, G.X. Cai, F. Ren, C.Z. Jiang, *EPL* 93 (2011) 57009.
30. C.W. Cheng, E.J. Sie, B. Liu, C.H.A. Huan, T.C. Sum, H. D. Sun, H.J. Fan, *Appl. Phys. Lett.* 96 (2010) 071107.
31. W. Lai, J. An, H.C. Ong, *Appl. Phys. Lett.* 86 (2005) 251105.
32. A. Dev, J.P. Richters, J. Sartor, H. Kalt, J. Gutowski, T. Voss, *Appl. Phys. Lett.* 98 (2011) 131111.
33. M. Mahanti, T. Ghosh, D. Basak, *Nanoscale* 3(2011), 4427–4433.
34. M. Mahanti, D. Basak, *Chem. Phys. Lett.* 542 (2012) 110–116.
35. F. Li, Y. Yuan, J. Luo, Q. Qin, J. Wu, Z. Li, X. Huang, *Appl. Surf. Sci.* 256 (2010) 6076–6082.
36. H. Zhu, D. Yang, H. Zhang, *Inorganic Materials* 42 (2006) 1210–1214.
37. B. Nikoobakht, M.A. El-sayed, *Langmuir* 17 (2001) 6368–6374.
38. S. Tascioglu, *Tetrahedron*, 52 (1996) 11113–11152.

39. N.R. Jana, L. Gearheart, C.J. Murphy, *Chem. Commun.* (2001) 617–618.
40. X.H. Liu, X.H. Luo, S.X. Lu, J.C. Zhang, W.L. Cao, *J. Colloid Interface Sci.* 307 (2007) 94–100.
41. M.M. Husein, E. Rodil, J.H. Vera, *J. Nanoparticle Res.* 9 (2007) 787–796.
42. N.R. Yogamalar, R. Srinivasan, A.C. Bose, *Opt. Mater. (Amst)*. 31 (2009) 1570–1574.
43. T.C. Damen, S.P.S. Porto, B. Tell, *Phys. Rev.* (1966) 570–574.
44. Y. Zhang, H.B. Jia, R.M. Wang, C.P. Chen, X.H. Luo, D.P. Yu, *Appl. Phys. Lett.* 83 (2003) 4631.
45. G. Naja, P. Bouvrette, S. Hrapovic, J.H. Luong, *Analyst.* 132 (2007) 679–686.
46. A. Ahern, R. Garrell, *Anal. Chem.* (1987) 2813–2816.
47. T.M. Herne, A.M. Ahern, R.L. Garrell, *Anal. Chim. Acta.* 246 (1991) 75–84.
48. M. Zhu, G. Qian, G. Ding, Z. Wang, M. Wang, *Mater. Chem. Phys.* 96 (2006) 489–493.
49. S. Xu, Z.H. Li, Q. Wang, L.J. Cao, T.M. He, G.T. Zou, *J. Alloys Compd.* 465 (2008) 56–60.
50. K. Vanheusden, W.L. Warren, C.H. Seager, D.R. Tallant, J.A. Voigt, B.E. Gnade, *J. Appl. Phys.* 79 (1996) 7983–7990.
51. J. Yguerabide, E.E. Yguerabide, *Anal. Biochem.* 262 (1998) 137–156.
52. C.W. Lai, J. An, H.C. Ong, *Appl. Phys. Lett.* 86 (2005) 251105.
53. D. Zhang, P. Wang, R. Murakami, X. Song, *Appl. Phys. Lett.* 96 (2010) 233114.

## **Chaper 3 Synthesis and Characterization of Pd Octahedral and Pd Spherical Nanocrystals on Graphene Oxide used as Anode Material for Direct Methanol Fuel Cells**

### 3.1 Introduction

Noble metal nanocrystals have engrossed much research attention for their use in photonics, sensing, thermal, and magnetic as wells catalytic properties <sup>[1-3]</sup>. Their physical and chemical properties can easily be altered by controlling the size and shape. Size determines the ratio of surface to bulk atoms specifically and surface area. Shape controls the facets and thus the surface structure of a nanocrystal, as well as the segments of atoms at the corners and edges. Moreover, shape has more importance than the size and other parameters and it offers greater flexibility in tuning the catalytic properties of a nanocrystal, especially when the atoms at different facets have different activities <sup>[4]</sup>. Although, for face-centered cubic (fcc) metals, the morphology and surface of their nanocrystals are closely connected issues of matter, nevertheless, their properties depend differently upon the morphology and surface structure of the nanocrystals <sup>[5,6]</sup>. For example, as a superficial property, catalysis of noble metal nanocrystals are concerned more of their surface structure <sup>[7,8]</sup>. Previously, a number of different synthetic chemical strategies have been established to control the morphology of noble metal nanocrystals <sup>[9]</sup>. State-of-the-art, solution based methods have been developed as a versatile methodology for controlled synthesis of noble metal nanocrystals and their alloys, where it is essential to produce zero valent noble metal through reduction of the metal precursor ions in the presence of surfactants and stabilizing agents. For Pd, many different shapes have been developed and applied by controlling the thermodynamics parameters or kinetics of the reactants involved in the growth of nanocrystals. When the progression is under thermodynamic control, the reaction product will have the lowest surface energy. In this situation, the capping agents play an important role in influencing the shaping of the final products by altering the order of surface energies for different facets completed through selective adsorption and consequently their growth rates <sup>[10]</sup>. However, the product of a kinetically controlled synthesis can knowingly diverge from the thermodynamically preferred structure that contains high index facets or concave surfaces <sup>[11]</sup>.

For Pd and Pt nanocrystals, currently, the surface adsorption method has also been recognized in which robust and precise surface adsorption of small adsorbates as reducing agents has seemed as a leading method to control the surface structure of their nanocrystals [12,13]. Particular adsorption of small adsorbates controls only the surface structure of Pd and Pt nanocrystals, other reasons extra than the specific adsorption have been employed to develop the morphology of noble metal nanocrystals. An extensive range of reducing agents have been used to make noble metal nanoparticles, including hydrogen and carbon monoxide gases, metal hydrides, hydrazine, hydroxyl amine, ascorbic acid, citric acid and vitamin B [14]. Hydrogen gas in particular is an operational reducing agent for noble metal precursor salts in aqueous or non-aqueous solutions. Prominently, it offers a clean, reducing atmosphere with no destructive by-products created during the reactions [15]. Furthermore, the usage of hydrogen decouples the influence of the reducing agent and stabilizing agent on the nucleation and any preferred directional growth of the particles. In recent times, hydrogen has been used in an aqueous media as a reducing agent in decorating various 2D nanostructures with Pd, Ru and Pt nanoparticles [16]. CO has also been used most influential reducing and shaping agent in the last era. Its adsorption properties have been inspected on different faces of metal nanocrystals. In the case of Pt, co-adsorption of CO and amines makes Pt {100} surface more actively stable than Pt {111} surface and thus stimulates the creation of Pt nanocubes [17,18]. CO errands to adsorb on Pd {111} surface and assists the growth of ultrathin Pd nanosheets having {111} as the main disclosure surface and presenting unique optical properties [19,20]. Two current examples are (1) the favored growth of micrometer lengthy five-fold linked Pd nanowires over Pd nanocubes under slow reduction and (2) the fabrication of corolla-like Pd mesocrystals in the co-existence of  $\text{Fe}^{3+}$  as the oxidative etchant and CO as the surface controller [21]. In these two illustrations, the control over the surface adsorption procedure by reduction kinetics and presenting oxidative etching to interrupt the growth of seeds supplement the morphology of noble metal nanocrystals.

Gang Fu *et al.*, demonstrated that CO explicitly adsorbs on Pd (111) surface, the adsorption strength and exposure of CO on Pd surfaces can be basically varied by presenting  $\text{H}_2$  to assist the formation of single crystalline Pd tetrapod and tetrahedral nanocrystals bounded by (111) surfaces. They have prepared in the co-presence of CO and  $\text{H}_2$  prepared tetrapod and tetrahedral nanocrystals. Upon aging in air, the as prepared nanocrystals extinguish hydrogen and were transformed slowly to Pd nanocrystals. They have designed conclusion by density functional theory (DFT) calculations that the creation of palladium



hydride in the presence of H<sub>2</sub> deteriorates the chemisorption of CO and thus helps to lower the CO coverage to encourage the formation of Pd tetrapod nanocrystals [22].

In this chapter, we have evaluated the surface adsorption behavior of CO and H<sub>2</sub> by their reduction kinetics separately in the presence of same capping agent PVP to synthesize Pd octahedral and spherical NCs. Their catalytic activity as anode material for DMFCs has measured comparatively. For anode material two types of results have shown here, first for basic electrocatalytic characterization analysis such as HER performance to remove the adsorbed hydrogen on the active sites of catalyst surface and second the MOR activity. Their electrocatalytic activity for HER and MOR analysis, give interesting results with a shape difference of the two same facets. MOR activity is presented here with respect to both the scales such as specific activity and mass activity.

### 3.2 Methanol Oxidation Reaction (MOR)

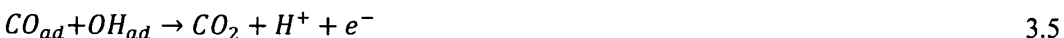
The electrooxidation of methanol on pt surfaces in acidic media has been experimentally and theoretically studied in excessive detail in the last eras [23-27] and can be written in the overall reaction as:



The adsorbed methanol is stepwise dehydrogenated by follow-on the creation of adsorbed CO<sub>ads</sub>. In addition to the adsorbed CO, also the existence of the intermediate CH<sub>3</sub>OH<sub>ads</sub> is estimated.



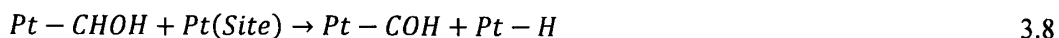
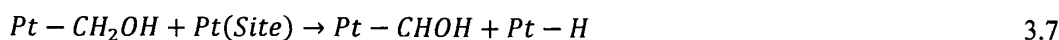
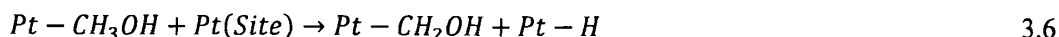
The adsorbed CO is oxidized through OH<sub>ads</sub>, which is made by the dissociative adsorption of water.



In parallel to these key reaction pathways side reactions like the backlog of formic acid [28,29] is also conceivable. But until now the elementary steps are still under investigation although a lot of studies for methanol oxidation on well-defined Pt and Pt alloy surfaces discussing the overall pathways and reaction mechanisms were performed [23,30]. The oxidation of methanol is following a dual reaction pathway via an indirect or a direct reaction to form CO<sub>2</sub>. The indirect pathway is found by the formation of adsorbed CO which is then oxidized to CO<sub>2</sub>. Depending on the potential of the adsorbed CO can block the water activation at low applied potentials. Higher potentials lead to an oxidation of CO to CO<sub>2</sub>. The

direct pathway proceeds via the formation of formaldehyde and formic acid which are soluble in the electrolyte and can be oxidized to form CO<sub>2</sub>. Both intermediates can subsequently be oxidized to CO<sub>2</sub>. As already mentioned above, the electrocatalysis of methanol has challenging tasks to solve. CO is a strong adsorbate and a stable intermediate during the methanol decomposition. Particularly the strong poisoning of the common used platinum containing electrodes in fuel cells leads to a decreasing activity <sup>[31]</sup>. The anode overpotential in a direct methanol fuel cell (DMFC) with state of the art technology is higher compared to the overpotential in a hydrogen fuel cell (PEM-FC). This results in reduced overall cell efficiency although the thermodynamic standard potentials of the hydrogen oxidation and the methanol oxidation are similar. However, the methanol oxidation is by several orders of magnitude slower compared to the hydrogen oxidation.

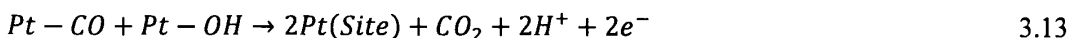
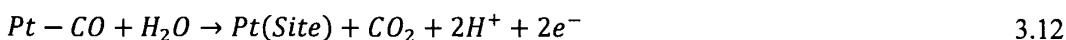
In the early seventies Bagotzky *et al.*, <sup>[24]</sup> proposed a general mechanistic scheme including all possible intermediates from methanol to CO<sub>2</sub>. Up to eight intermediates were assumed, of which CO, formic acid and formaldehyde are the most interesting ones. In addition, Lopes *et al.*, <sup>[25]</sup> found indications of a methoxy species in electrochemical systems that could further complicate the mechanistic scheme of methanol oxidation on Pt. Undoubtedly, the oxidation of methanol on Pt surfaces starts with dehydrogenation of the methanol molecule as shown by differential electrochemical mass spectrometry. The first dehydrogenation step, reaction (2), was shown to be the rate determining step on the Pt(111) and Pt(110) surfaces through measurements of the kinetic isotope effect and the Tafel slope of the reaction [15,16]. The rate determining step on the Pt(100) surface was shown to be the second dehydrogenation reaction, equation (3.8). The effect of surface structure on the electrocatalytic properties towards methanol oxidation has been demonstrated several times. For simplicity, we assume that one adsorbed molecule binds to only one surface platinum atom in the following simplified reaction scheme. According to Munk *et al.*, <sup>[26]</sup>, the complete stripping of all three methyl hydrogen atoms at lower potentials must occur on the flat terrace areas of the electrode surface, due to the fact that at least four adjacent adsorption sites are needed. Furthermore, successive dehydrogenation eventually leads to formation of adsorbed carbon monoxide:



The dehydrogenation reactions lead to formation of adsorbed hydrogen atoms, which in turn will be followed by a one-electron transfer reaction to form a proton and an electron:



Although considerable effort has been made to elucidate the exact mechanism of methanol oxidation at platinum and platinum-based electrodes, an exact description of the reaction mechanism still remains unclear. Specifically, the main issue, which remains controversial, is whether the adsorbed CO formed during methanol electrooxidation is a necessary intermediate in a serial pathway mechanism, as described by equation (3.11) and (3.12) or (3.13), or an unwanted poison in a parallel reaction mechanism that leads to a stable oxidation product (CO<sub>2</sub>, formic acid and formaldehyde) through short-lived intermediates, equations (3.14)-(3.16). However, both formic acid and formaldehyde oxidation may subsequently lead to CO<sub>ads</sub> formation.



Solving these tasks implies modifying the catalyst on which the methanol oxidation occurs. Although platinum is the catalyst with the highest reactivity towards MOR the overpotential for adequate activity is until now very high for applications with high power output. For the well-known Pt-Ru alloy<sup>[32]</sup> and its derivatives<sup>[33]</sup> a lower overpotential and an increased reactivity was found, explained by ligand or bi-functional effects. However, there are a lot of improvements to do. The activity is not as high as demanded and the compositions which are under current investigation are consisting of expensive and rare metals.

### 3.3 Experimental Procedure

#### 3.3.1 Chemicals and Materials

H<sub>2</sub>PdCl<sub>4</sub> (99.9 % metal basis) was purchased from Alfa Aesar, Poly(vinylpyrrolidone) (PVP), MW = 58000, AR) was purchased from Sinopharm Chemical Reagent Co. Ltd. (Shanghai, China). All reagents were used as received without further purification.

### 3.3.2 Synthesis of Graphene Oxide

The catalyst support, reduced graphene oxide (GO), was prepared through the reduction of graphite by  $\text{NaBH}_4$ . The graphene oxide (GO) was prepared by the modified Hummers and Offenmans method <sup>[34]</sup>. In a typical experiment 2 g of graphite powder was first added into 100 mL concentrated  $\text{H}_2\text{SO}_4$  at room temperature. Under stirring, the mixture was cooled to 5 °C using an ice bath, and the temperature of the mixture was kept to be below 5 °C for 30 min. 8 g  $\text{KMnO}_4$  was then added gradually under stirring and cooling, so that the temperature of the mixture was not allowed to reach 10 °C. 100 mL distilled water was added into the mixture, stirred for 1 h, and further diluted to approximately 300 mL with distilled water. After that, 20 mL of 30%  $\text{H}_2\text{O}_2$  was added to the mixture to reduce the residual  $\text{KMnO}_4$ . The solid was filtered, washed with 5%  $\text{HCl}$  aqueous solution to remove metal ions and with distilled water until the pH were 6. The resulting graphite oxide was dried at 50 °C for 24 h.

### 3.3.3 Synthesis of Pd Octahedral Nanocrystals on Graphene Oxide

Above synthesized GO powder was dispersed in water (1mg/1mL) and ultrasonicated for 30 minutes. Then 105 mg of PVP as capping agent and 1 mM of  $\text{H}_2\text{PdCl}_4$  solution was added in GO dispersion. Reaction flask was sealed to create high vacuum environment and heated up to 95 °C with continuous stirring and bubbling of  $\text{H}_2$  as reducing agent for 30 minutes. The resulting products were collected by centrifugation and washed several times with ethanol and acetone to remove excess amounts of PVP from nanocrystals. Pd octahedral nanocrystal is demonstrated as GO/Pd-01 in all figures.

### 3.3.4 Synthesis of Pd Spherical Nanocrystals on Graphene Oxide

For spherical nanocrystals the synthesis procedure is exactly the same as above for octahedral nanocrystals but only the difference is  $\text{CO}$  gas is used as a reducing agent instead of  $\text{H}_2$ . Pd spherical nanocrystal is demonstrated as GO/Pd-02 in all figures.

### 3.3.5 Characterization Tools

#### 3.3.5.1 Physical Characterization

After synthesis of GO, its characterizations were done to make sure the 2D structure of GO sheets, presence of C-C / C-H / C-OH bonds, characteristics of GO with transmission electron microscopy (TEM), Fourier transform infrared spectroscopy (FTIR) and UV-Vis spectroscopy, respectively. Then after synthesis of Pd nanocrystals on GO, their physical

characterizations were done by scanning electron microscopy (SEM), the powder X-ray diffraction (XRD) measurements were performed with an X'pert PRO instrument (PANalytical) using CuK $\alpha$  radiation ( $\lambda = 0.15418$  nm) and UV-Vis spectroscopy within the range of 200 to 800 nm.

### 3.3.5.2 Electrochemical Characterization

Before each electrochemical experiment, a glassy carbon (GC) electrode (0.196 cm<sup>2</sup> geometric surface area) was first polished with alumina slurries (Al<sub>2</sub>O<sub>3</sub>, 0.05  $\mu$ m) on a polishing cloth to obtain a mirror finish, followed by sonication in 0.1 M HNO<sub>3</sub>, 0.1 M H<sub>2</sub>SO<sub>4</sub>, and pure water for 10 min, successively. To prepare a catalyst-coated working electrode, 15  $\mu$ L of the 1 mg/mL suspension in pure water was drop-coated on the polished electrode surface by a microliter syringe, followed by drying in vacuum at room temperature. Afterward, the catalyst was covered with a thin layer of Nafion (0.1 wt % in water, 5  $\mu$ L) to ensure that the catalyst was tightly attached to the electrode surface during the electrochemical measurements. Voltammetry measurements were carried out with a CHI750D electrochemical workstation. The electrode prepared above was used as the working electrode. The Ag/AgCl (in 3 M NaCl, aq.) combination isolated in a double junction chamber and a Pt coil were used as the reference and counter electrodes, respectively. All the measurements were performed in electrochemical experiments with respect to standard values of reversible hydrogen electrode (RHE). Electrochemical characterizations were done by cyclic voltammetry (CV), linear sweep voltammetry (LSV) and chronoamperometry (CA).

## 3.4 Results and Discussion

### 3.4.1 Morphology, Mechanism and UV-Vis Absorption

A facile synthetic route is applied to prepare GO/Pd hybrid composites with different shape Pd nanocrystals as illustrated in the schematic diagram in Figure 3.1. For this purpose, we initially prepare GO via the Hummer's method and then reduce it by NaBH<sub>4</sub>. Since GO contains a large number of oxygen-containing functional groups, which allow GO to be well dispersed in an aqueous solution<sup>[34]</sup>. Their functional group presence is analyzed from FTIR spectra given in Figure 3.2b. The graph shows the stretching of hydroxyl group at 3450 cm<sup>-1</sup>, the C=O carbonyl stretching at 1728 cm<sup>-1</sup>, and the C–O epoxide group stretching at 1229 and

$1061\text{ cm}^{-1}$  [37]. The high intensity of the main peaks in GO confirms the presence of a large amount of oxygen functional groups after the reduction process.

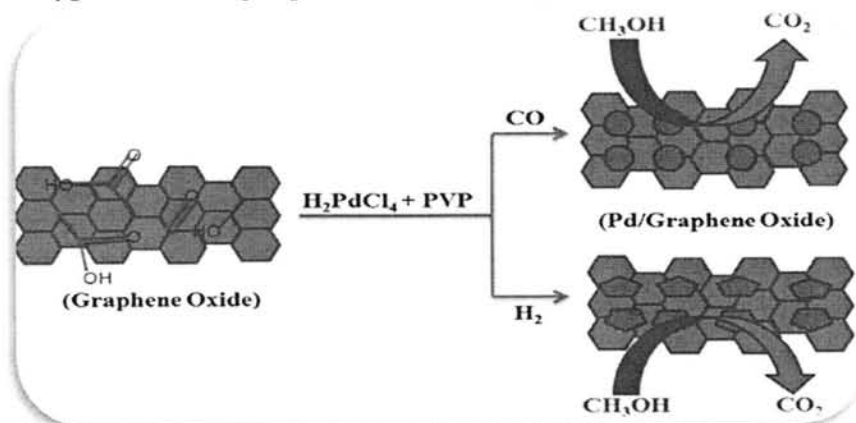


**Figure 3.1** Schematic representation of the synthesis procedure of the GO/Pd hybrid catalyst.

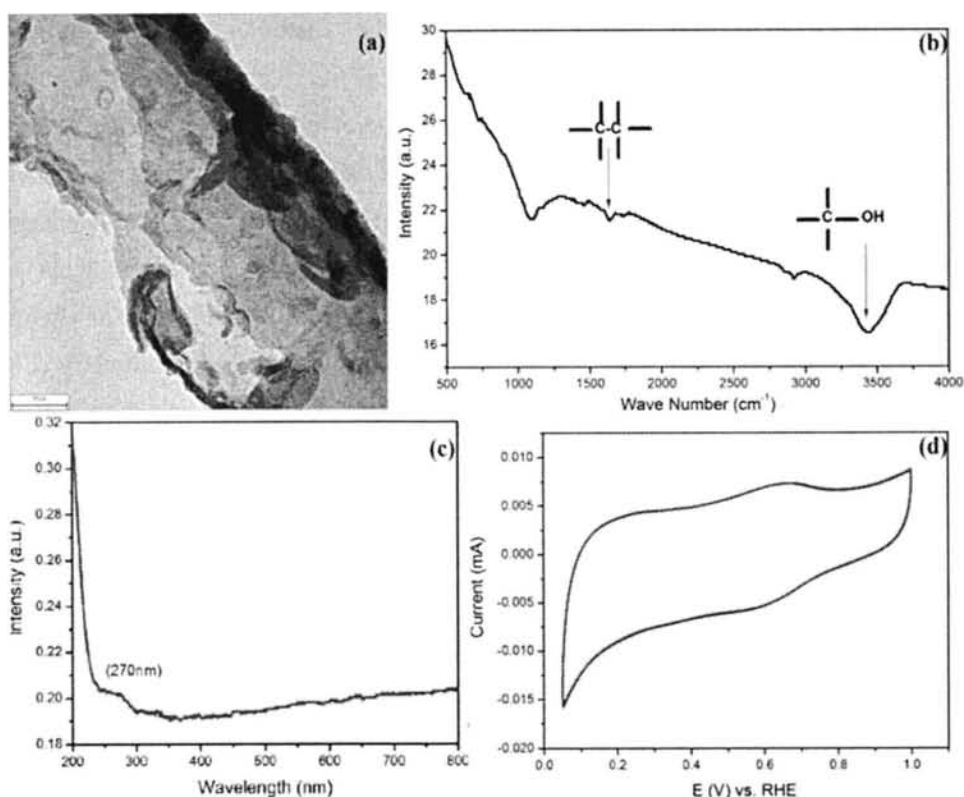


**Figure 3.2** Characterizations of synthesized Graphene Oxide (a) TEM image, (b) FTIR spectrum, (c) UV-Vis spectrum and (d) CV in 0.1M HClO<sub>4</sub> at a scan rate of 50 mV/s vs RHE.

The morphology of sheet structure of GO is analyzed from TEM (Figure 3.2a). The reduced graphene oxide exhibit typical wrinkled structure that cause sheet folding [38]. This

2D structure of GO and presence of oxygen-containing functional groups not only increases the specific contact area, which facilitates the transport of the Pd<sup>[39]</sup> ions and electrons into the inner region of the graphene sheets, but also provides more exposed active sites for the anchoring of Pd precursors and Pd nucleation. Figure 3.2c shows the UV-Vis absorption spectra of GO. The GO, maximum absorption is obtained at 270 nm wavelength, corresponding to the  $\pi$ - $\pi^*$  transition of aromatic C-C bonds. The reduced GO sample was also characterized using cyclic voltammetry (CV) for determining their suitability for application as electrode materials in direct methanol fuel cells. CVs of the cell measured in the voltage window of 0.0 to 1.0 V and scan rate of 50 mV/s in 0.1 M HClO<sub>4</sub> shown in Figure 3.2d indicate capacitive nature of the materials. The maximum current was obtained at 0.7 V for oxidation and 0.6 V for reduction.

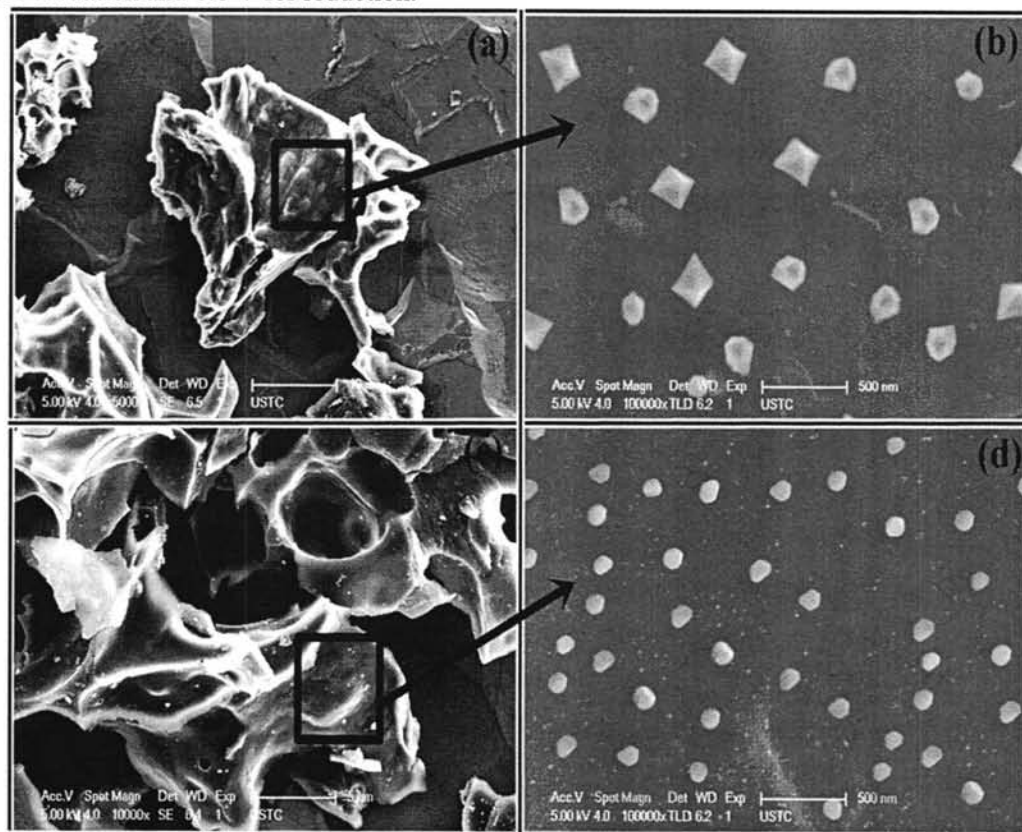


**Figure 3.3** FE-SEM images of (a) & (c) Pd nanocrystals on GO sheets, (b) & (d) High magnifications images of Pd Octahedral and Pd Spherical nanocrystals on GO sheets, respectively.

FE-SEM images of the samples GO/Pd-01 and GO/Pd-02 are shown in Figure 3.3. The FE-SEM images revealed that Pd spherical and octahedral nanocrystals with a uniform size were well-dispersed on the surfaces of the GO. It was clearly shown in FE-SEM micrographs

that spherical and octahedral Pd nanocrystals were the dominant phases. The high-magnification FE-SEM image shows that Pd octahedrons have well-defined shapes with a uniform size distribution. It can be seen that the prepared Pd nanocrystals are uniformly distributed on the GO surface. It should be noted that almost no Pd nanocrystals can be observed outside the GO sheet, indicating that GO serves here as a template for the Pd nanocrystals formation. As shown in Figure 3.3b, spherical Pd nanoparticles were deposited onto the surface of GO with greater retention of the spherical characteristics of the nanocrystals.

The obtained Pd-GO composite was characterized by a UV-Vis absorption spectrum to confirm the existence of Pd nanocrystals loaded on GO as shown in Figure 3.4. In the absorption spectrum of RGO (Figure 3.2c), the broad absorption peak centered at around 270 nm can be ascribed to the  $\pi$ - $\pi^*$  transitions of aromatic C=C bonds. For the GO/Pd hybrid composite, no obvious absorption peak was observed, showing a typical Mie exponential decay profile<sup>[40]</sup>.

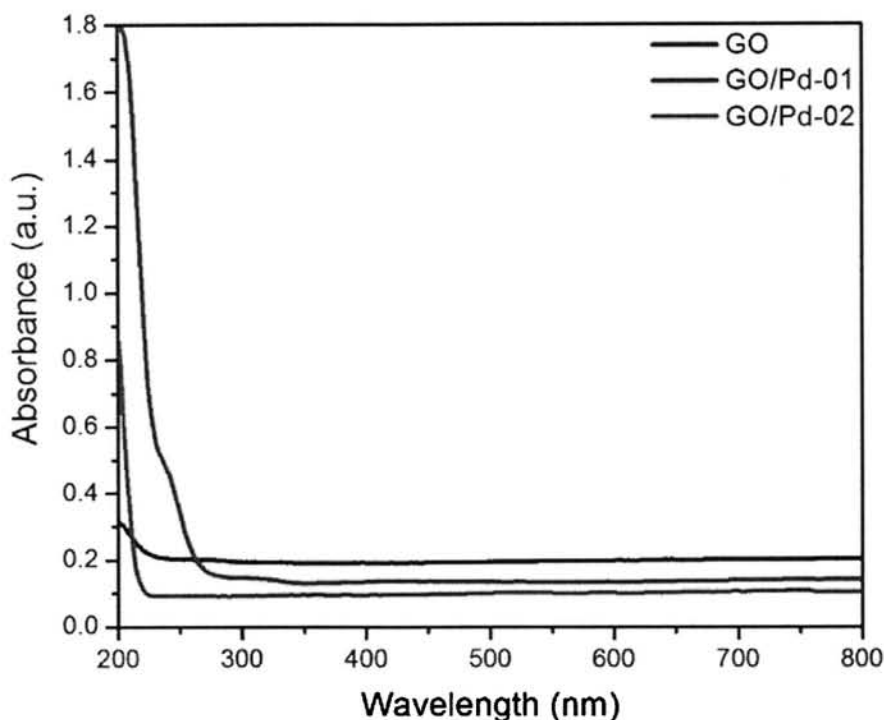


**Figure 3.4** UV-Vis spectra of Pd Octahedral (GO/Pd-01) and Pd Spherical (GO/Pd-02) nanocrystals.



### 3.4.2 Structural Characterization

GO/Pd composite was characterized by X-ray diffraction (XRD) to investigate the crystalline structure of the hybrid. As shown in Figure 3.5, the XRD pattern of Pd/GO-1 and Pd/GO-2 composites, diffraction peaks at  $40.20^\circ$ ,  $46.87^\circ$ ,  $68.56^\circ$  and  $81.93^\circ$  are ascribed to the (111), (200), (220) and (311) crystalline planes of the face centered cubic (fcc) structure of Pd, respectively. The diffraction peaks are consistent with an fcc crystalline structure of bulk Pd (JCPDS, card no. 46-1043). The relatively broad diffraction peak observed at  $10^\circ$  to  $30^\circ$  centered at  $2\theta = 24.5^\circ$  corresponds to the (002) plane of graphene. It is eminent fact that metallic Pd is catalytically active to split  $H_2$  molecules to hydrogen atoms which can completely permeate into Pd to form metal hydride <sup>[41-44]</sup>. In fact, the powder XRD measurements (Figure 3.5) on the freshly prepared Pd nanocrystals confirmed that the as-prepared octahedrons and spherical nanocrystals are completely metallic and there is no evident peak observed for  $\beta$ -PdHx. This may be due to the high vacuum environment and temperature that all the transition phases of Pd are converted into a metallic phase Pd.

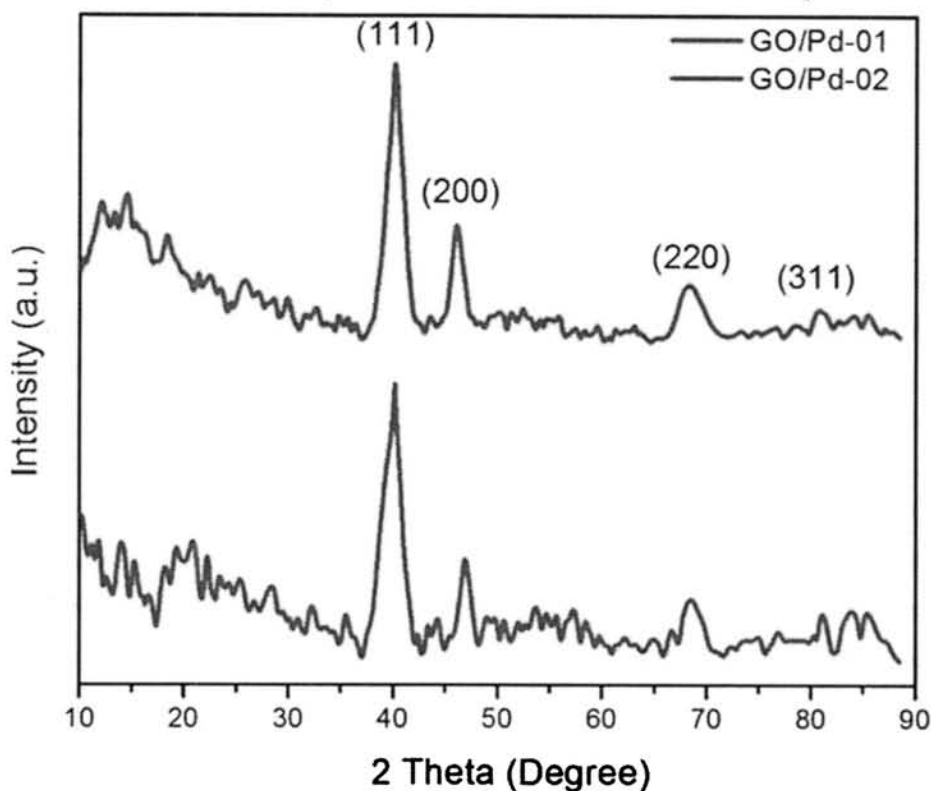


**Figure 3.5** XRD spectra of Pd octahedral (GO/Pd-01) and Pd spherical (GO/Pd-02) nanocrystals.

### 3.4.3 Electrochemical Performance

The electrochemical properties of Pd/GO hybrid composites were examined by measuring cyclic voltammograms (CVs). Before observing the electrochemical behavior of the catalysts, they were cleaned by three different methods. Because the metal surface capped with organic ligands, which served as capping agents, largely reduce their catalytic activity when they are used as catalysts. In the past few years, various methods have been applied to clean or remove these surfactants, such as thermal annealing, acetic acid washing, oxygen plasma cleaning, and UV-ozone irradiation. However, these methods require either extremely high temperature or long treatment time. At the same time, the cleaning process may cause the change in particle size and morphology, especially for the shaped nanocrystals. Therefore, it is essential to develop a simple and effective strategy to clean the surface of nanoparticles and make them catalytically active. Here, we demonstrate that CO-stripping is an efficient method to clean the particle surface over oxygen plasma cleaning and simple electrochemical cleaning and thus improve the electrocatalytic activity of the PVP- stabilized Pd nanocrystals [45-49].

Figure 3.6 and Figure 3.7 show the CVs of the Pd octahedral and spherical nanocrystals supported on a glassy carbon electrode respectively, after electrochemical, oxygen plasma and CO-stripping treatments. The hydrogen region (0-0.2 V) shows the hydrogen underpotential deposition (UPD) peaks in base electrolyte and these are suppressed in the presence of methanol due to formation of adsorbed CO on the hydrogen sites [50-54]. Compared to the all three treatments, the CO stripping-treated electrode exhibited clearer hydrogen region and oxygen region and eventually an increased electrochemically active surface area (ECSA), which further can enhance catalytic activity towards methanol oxidation. Finally, more surface atoms were exposed and became electrochemically active after CO stripping which is also characterized by CV at longer scale from 0.05 to 1.2 V vs RHE where oxidation reductions peaks are clearly visible which is given in Figure 3.8. The present result is similar to that of another recent study where the CO treated cleaned PtPd/RGO catalyst and surfactant-free Ag nanorods exhibited good characteristic CV and much enhanced electrocatalytic activity compared with the PVP-stabilized ones [55-57].

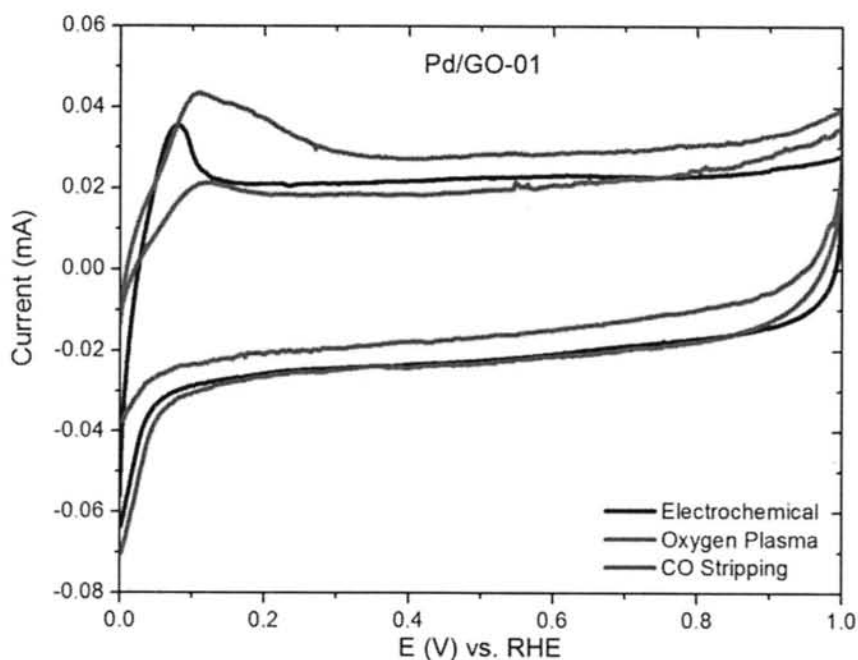


**Figure 3.6** CVs of Pd octahedral (GO/Pd-01) nanocrystals after different cleaning treatments, in 0.1M HClO<sub>4</sub> at a scan rate of 50 mV/s vs RHE.

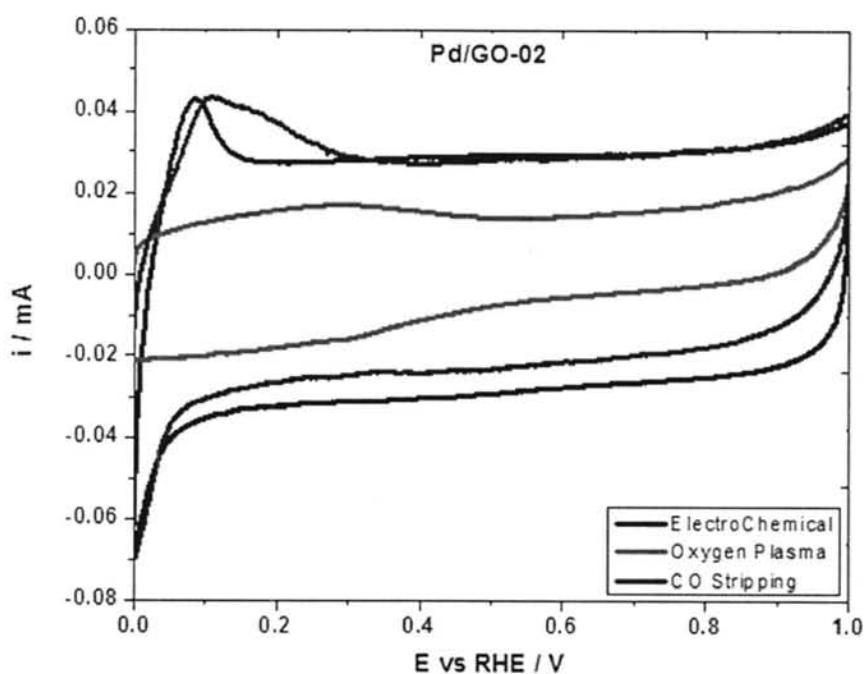


**Figure 3.7** CVs of Pd spherical (GO/Pd-02) nanocrystals after different cleaning treatments, in 0.1M HClO<sub>4</sub> at a scan rate of 50 mV/s vs RHE.

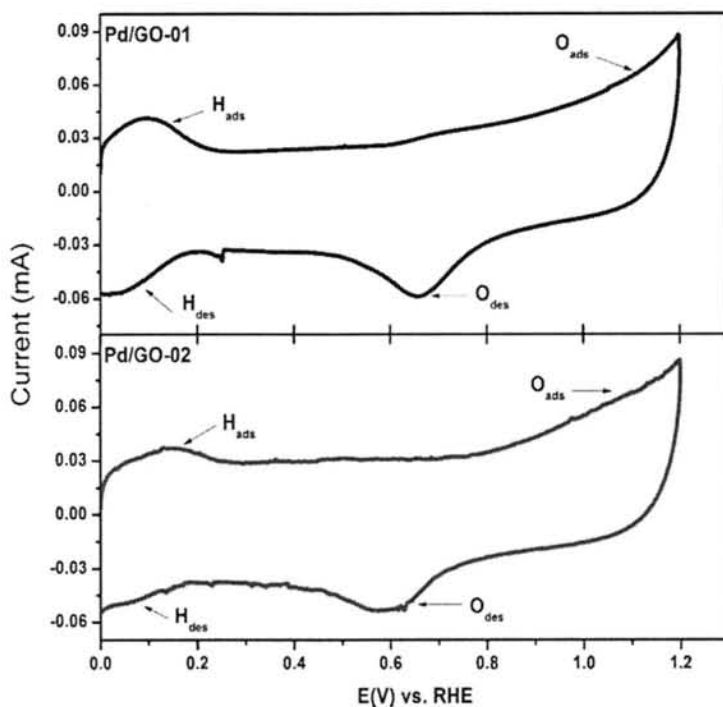


**Figure 3.8** CVs of Pd octahedral (GO/Pd-01) and Pd spherical (GO/Pd-02) nanocrystals after CO-stripping cleaning treatment in a wide potential range between 0 V to 1.2 V vs RHE to show the oxidation ( $H_{ads}$ ,  $O_{ads}$ ) reduction ( $H_{des}$ ,  $O_{des}$ ) peaks, in 0.1M  $HClO_4$  at a scan rate of 50 mV/s vs RHE.

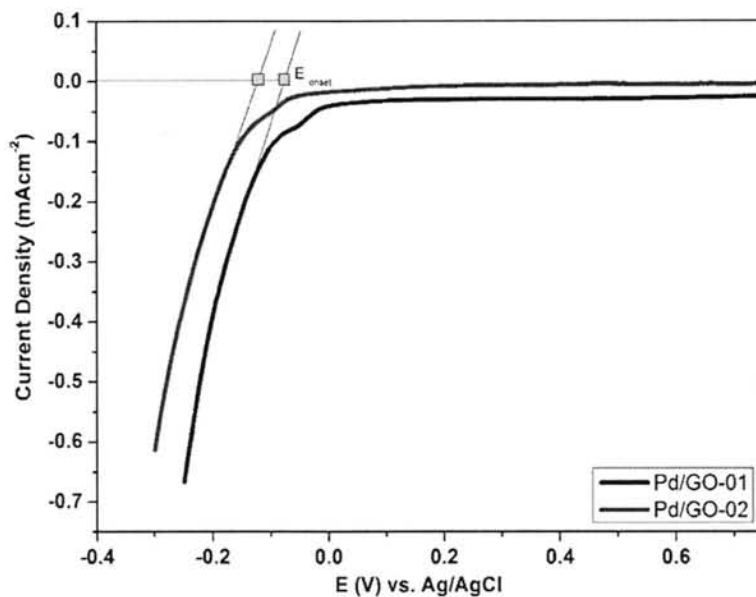


**Figure 3.9** Polarization curves for HER activity of Pd octahedral (GO/Pd-01) and Pd spherical (GO/Pd-02) nanocrystals in 0.1M  $HClO_4$  at a scan rate of 10 mV/s vs Ag/AgCl.  $E_{onset}$  for HER is measured by tangent method.

HER performance of the two composites is presented in Figure 3.9. The onset potential is measured by tangent method to evaluate the HER catalytic activity. Figure 9 shows that the onset potential for evaluation of adsorbed hydrogen on the surface active sites of the catalyst is more near towards zero for octahedral NCs than that of spherical NCs. This result concludes that octahedral NCs could show better performance as anode material for DMFCs, which is further proved by MOR measurements.

The electro catalytic activity of Pd spherical and octahedral nanocrystals towards methanol oxidation in 0.1 M HClO<sub>4</sub>+1M CH<sub>3</sub>OH solution at a scan rate of 50 mV/s is demonstrated in Figure 3.10. The current density is normalized to the geometric surface area to make a comparison of the two catalysts loaded on same diameter sized GCE. The characteristic potential regions for methanol oxidation on platinum in relationship to the behavior in HClO<sub>4</sub> alone are discussed in reference to the curves in Figure 3.10. The current for methanol oxidation commences at around 0.3 V for both the nanocrystals where the blank shows only charging of the double-layer. The oxygen source in this potential region is assumed to be adsorbed or dissociated water. At potentials below 0.40 V to 0.30 V, the oxidation current is lower, but not negligible in all voltammograms because the surface active sites are poisoned by CO<sub>ads</sub>, an intermediate from dehydrogenation of methanol. With the potential increasing, the oxidation current takes off rapidly, representing that significant methanol oxidation occurs. The main methanol oxidation peak occurs at 0.9 V for octahedral nanocrystals and for spherical nanocrystals it occurs at 0.58 V where platinum oxide formation occurs. When reversing the potential at 0.75 V for octahedral and 0.35 V for spherical nanocrystals, and performing a negative-going sweep, the current remains anodic for a little while but decrease. When the oxide is reduced, Pt sites on the electrode are again available for methanol oxidation and the current increases. The resulting oxidation peak is shifted slightly to more negative potentials than on the positive-going oxidation peak. At more negative potentials, the current decreases due to an increased coverage of adsorbed CO, which is recognized as the catalyst poison in methanol oxidation on platinum.

The increase of oxidation current at the start of the oxidation is also characterized by CA measurements up to 300 seconds at constant potentials of 0.30 V, 0.40 V and 0.50 V demonstrated in Figure 3.11. This CA measurement clearly showing the increase of oxidation current from lower potential to higher potential with maximum stability for 300 s for both the catalysts. Onset potential and current density are the two major parameters to evaluate the catalytic activity of electro catalysts. The onset potential of both the catalysts is obtained at 0.30 V vs RHE. But the current density at onset potential for Pd octahedral nanocrystals is

higher than that of Pd spherical nanocrystals, which is characterized by CA measurements. The maximum current density at positive potential or forward current is obtained for the Pd octahedral catalyst at ca.  $4.5 \text{ mA/cm}^2$  (specific activity), ca.  $5300 \text{ mA/mg}_{\text{Pd}}$  (mass activity) and for Pd spherical catalyst at ca.  $2 \text{ mA/cm}^2$  (specific activity), ca.  $1800 \text{ mA/mg}_{\text{Pd}}$  (mass activity) <sup>[59]</sup>. These results indicate that Pd octahedral offers a high electrocatalytic activity towards methanol oxidation than Pd spherical nanocrystals. The reason is that in Pd octahedral nanocrystals, (111) facets are more abundant and exposed to the surface to catalyze the methanol molecules more effectively than Pd spherical nanocrystals. In Pd octahedral nanocrystals the edges and corners of octahedral geometry are also effectively important for the oxidation of formic acid into  $\text{CO}_2$  <sup>[60]</sup>. As the formic acid is one of the intermediate in the electro oxidation mechanism of methanol. This intermediate is also catalyzed by octahedral nanocrystals but on the other hand, spherical nanocrystals became unable to oxidize this intermediate rapidly and ultimately which terminate the further oxidation of methanol.

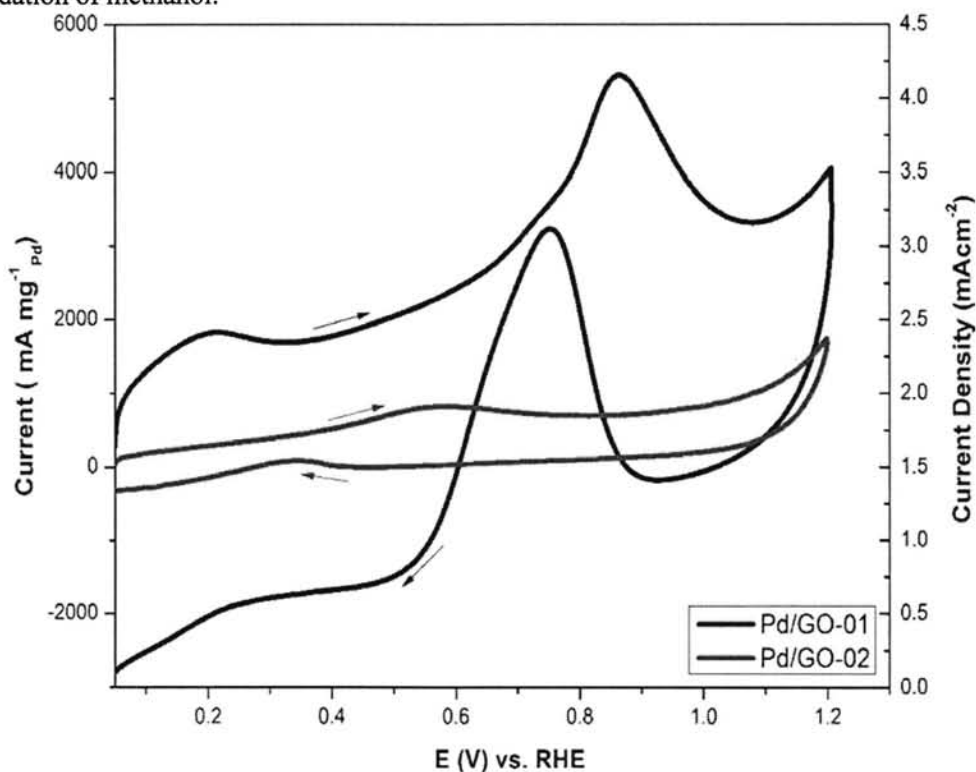


**Figure 3.10** MOR activity peaks (forward and backward scans) of Pd octahedral (GO/Pd-01) and Pd spherical (GO/Pd-02) nanocrystals in  $0.1\text{M HClO}_4 + 1\text{M CH}_3\text{OH}$  at a scan rate of  $50 \text{ mV/s}$  vs RHE.

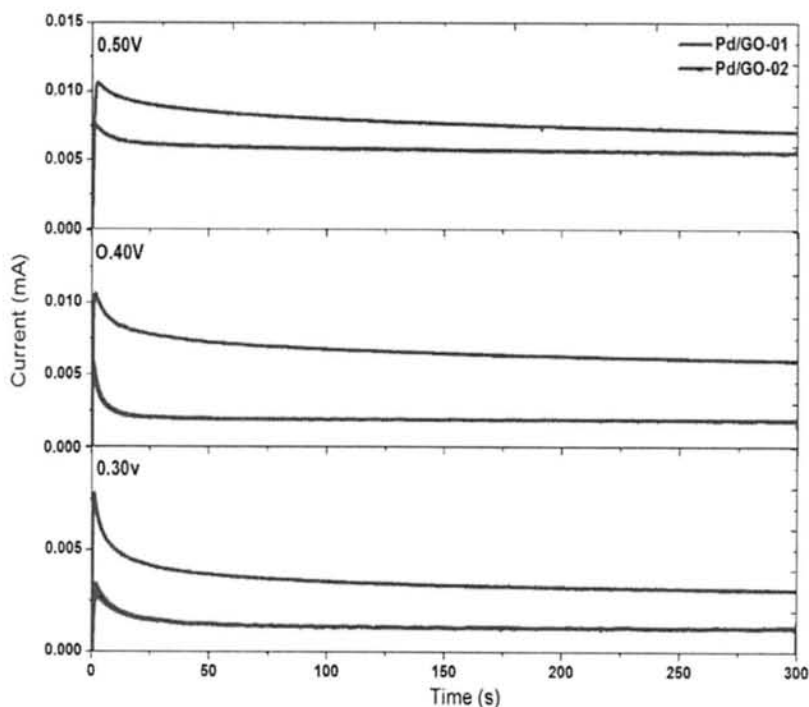


**Figure 3.11** CA results of MOR activity for Pd octahedral (GO/Pd-01) and Pd spherical (GO/Pd-02) nanocrystals in 0.1M HClO<sub>4</sub> + 1M CH<sub>3</sub>OH at constant voltage 0.30 V, 0.40 V and 0.50 V up to 300 s time.

### 3.5 Summary

In summary Palladium octahedral and spherical nanocrystals with uniform morphology were successfully synthesized in the presence of hydrogen and carbon monoxide respectively. The as-prepared Pd nanocrystals are bound with {111} facets. Hydrogen binds the octahedral sites of Pd and facilitate further atomic addition of Pd through the formation of PdH<sub>x</sub> with (111) facets to the final product of octahedral nanocrystals. More remarkably, it was also found that CO stripping is a competent method to remove the surfactants covered on the particle surface and thus improve the electrocatalytic performance of the Pd-based nanocrystals. The comparative studies of both the catalysts as anode material for direct methanol fuel cells (DMFCs) have been measured by hydrogen evaluation reaction performance and methanol oxidation reaction activity. The electrocatalytic properties of both the nanocrystals were studied in HClO<sub>4</sub> acidic media and compared with each other. Pd octahedral nanocrystals have shown the best performance as anode material, their onset potential for evaluation of hydrogen from the active sites of the catalyst is more towards zero than the spherical NCs. Moreover, Pd octahedral NCs have shown the specific MOR activity of ca. 4.3 mA cm<sup>-2</sup> and mass activity ca. 5300 mA mg<sup>-1</sup><sub>Pd</sub> much higher than that of spherical

NCs. The current work, not only gives a simple method to synthesize Pd nanocrystals with special facets on graphene oxide, but also offers a comparative analysis among both NCs. Together with the use of specific strong adsorbates to control the surface structure of Pd nanocrystals, the shape-control strategy, hydrogen evolution reaction activity and methanol oxidation reaction active catalyst reported here could provide a new research avenue to further enrich the Pd based nanocrystals.

### 3.6 References

1. T. K. Sau, A. L. Rogach, F. Jackel, T. A. Klar, J. Feldmann, *Adv. Mater.*, 22, 1805 (2010).
2. A. R. Tao, S. Habas, P. Yang, *Small*, 4, 310 (2008).
3. T. Teranishi, M. Hosoe, T. Tanaka, M. Miyake, *J. Phys. Chem. B*, 103, 3818 (1999).
4. Y. N. Xia, Y. J. Xiong, B. Lim, S. E. Skrabalak, *Angew. Chem., Int. Ed.*, 48, 60 (2009).
5. T. K. Sau, A. L. Rogach, *Adv. Mater.*, 22, 1781 (2010).
6. Z. Y. Zhou, N. Tian, J. T. Li, I. Broadwell, S. G. Sun, *Chem. Soc. Rev.*, 40, 4167 (2011).
7. D. Astruc, F. Lu, J. R. Aranzaes, *Angew. Chem., Int. Ed.*, 44, 7852 (2005).
8. R. Narayanan, M. A. El-Sayed, *J. Phys. Chem. B*, 109, 12663 (2005).
9. Z. M. Peng, H. Yang, *Nano Today*, 4, 143 (2009).
10. Y. Sun, Y. Xia, *Science*, 298, 2176 (2002).
11. H. Zhang, M. Jin, Y. Xia, *Angew. Chem., Int. Ed.*, 51, 7656 (2012).
12. M. Chen, B. Wu, J. Yang, N. Zheng, *Adv. Mater.*, 24, 862 (2012).
13. X. Huang, S. Tang, H. Zhang, Z. Zhou, N. Zheng, *J. Am. Chem. Soc.*, 131, 13916 (2009).
14. T. K. Sau, A. L. Rogach, *Complex-shaped Metal Nanoparticles: Bottom-up Synthesis and Applications*, John Wiley & Sons, Germany, 2012.
15. L. D. Rampino, F. F. Nord, *J. Am. Chem. Soc.*, 63, 2745 (1941).
16. W. Zhang, X. Chen, R. A. Boulos, J. Toster, C. L. Raston, *Chem. Commun.*, 50, 15167 (2014).
17. B. Wu, N. Zheng, G. Fu, *Chem. Commun.*, 47, 1039 (2011).
18. G. Chen, Y. Tan, B. Wu, G. Fu, N. Zheng, *Chem. Commun.*, 48, 2758 (2012).
19. Y. Xiong, Y. Xia, *Adv. Mater.*, 19, 3385 (2007).
20. X. Huang, S. Tang, X. Mu, Y. Dai, G. Chen, Z. Zhou, F. Ruan, Z. Yang, N. Zheng, *Nat. Nanotechnol.*, 6, 28 (2011).



21. X. Huang, S. Tang, J. Yang, Y. Tan, N. Zheng, *J. Am. Chem. Soc.*, 133, 15946 (2011).
22. Y. Dai, X. Mu, Y. Tan, K. Lin, Z. Yang, N. Zhen, G. Fu, *J. Am. Chem. Soc.*, 134, 7073 (2012).
23. N. M. Markovic and P. N. Ross, *Surf. Sci. Rep.*, 45 (2002) 121.
24. M. J. Janik, C. D. Taylor, and M. Neurock, *Top. Catalysis*, 46 (2007) 306.
25. T. Iwasita, *Electrochim. Acta*, 47 (2002) 3663.
26. R. Parsons and T. Vandernoot, *J. Electroanal. Chem.*, 257 (1988) 9.
27. E. Herrero, K. Franaszczuk, and A. Wieckowski, *J. Phys. Chem.*, 98 (1994) 5074.
28. A. Hamnett, *Catal. Today*, 38 (1997) 445.
29. G. T. Burstein, C. J. Barnett, A. R. Kucernak, and K. R. Williams, *Catal. Today*, 38 (1997) 425.
30. D. Kardash, C. Korzeniewski, and N. Markovic, *J. Electroanal. Chem.*, 500 (2001) 518.
31. T. D. Jarvi and E. M. Stuve, in the Science of Electrocatalysis on Bimetallic Surfaces (J. Lipkowski and P. Ross, eds.), Wiley-VCH, New York, 1998, p. 75.
32. O. A. Petrii, *J. Solid State Electrochem.*, 12 (2008) 609.
33. P. Strasser, Q. Fan, M. Devenney, W. H. Weinberg, P. Liu, and J. K. Nørskov, *J. Phys. Chem. B*, 107 (2003) 11013.
34. W. S. Hummers, R. E. Offeman, *J. Am. Chem. Soc.*, 80, 1339 (1958).
35. D. Li, C. Wang, D. Tripkovic, S. Sun, N. M. Markovic, V. R. Stamenkovic, *ACS Catal.*, 2, 1358 (2012).
36. M. Crespo-Quesada, J. M. Andanson, A. Yarulin, B. Lim, Y. Xia, L. Kiwi-Minsker, *Langmuir*, 27, 7909 (2011).
37. S. Thakur, N. Karak, *Carbon*, 50, 5331 (2012).
38. H. Zhang, P. X. Feng, *Carbon*, 48, 359 (2010).
39. X. M. Chen, G. Wu, J. Chen, X. Chen, Z. Xie, X. Wang, *J. Am. Chem. Soc.*, 133, 3693 (2011).
40. Y. J. Song, M. Wang, X. Y. Zhang, J. Y. Wu, T. Zhang, *Nanoscale Res. Lett.*, 9, 17 (2014).
41. M. Tüshaus, W. Berndt, H. Conrad, A. M. Bradshaw, B. Persson, *Appl. Phys. A: Mater. Sci. Process.*, 51, 91 (1990).
42. M. K. Rose, T. Mitsui, J. Dunphy, A. Borg, D. F. Ogletree, M. Salmeron, P. Sautet, *Surf. Sci.*, 512, 48 (2002).
43. E. Herrero, K. Franaszczuk, A. J. Wieckowski, *Phys. Chem.*, 98, 5074 (1994).

44. S. Schauer mann, J. Hoffmann, V. Johane k, J. Hartmann, J. Libuda, H. J. Freund, *Angew. Chem., Int. Ed.*, 41, 2532 (2002).
45. Z. M. Peng, H. J. You, H. Yang, *ACS Nano*, 4, 1501 (2010).
46. A. Eichler, *Surf. Sci.* 498, 314 (2002).
47. C. J. Zhang, P. J. Hu, *J. Am. Chem. Soc.*, 123, 1166 (2001).
48. G. A. Somorjai, Y. Li, *Introduction to Surface Chemistry and Catalysis*, 2nd ed.; John Wiley & Sons: Hoboken, NJ, 2010; Chapter 9, p 615.
49. M. Morkel, G. Rupprechter, H. J. Freund, *Surf. Sci.*, 588, 209 (2005).
50. J. I. Cerdá, B. Santos, T. Herranz, J. M. Puerta, J. de la Figuera, K. F. McCarty, *J. Phys. Chem. Lett.*, 3, 87 (2011).
51. J. E. Jr Worsham, M. K. Wilkinson, C.G. Shull, *J. Phys. Chem. Solids*, 3, 303 (1957).
52. W. Chen, J. R. Davies, D. Ghosh, M. C. Tong, J. P. Konopelski, S. W. Chen, *Chem. Mater.*, 18, 5253 (2006).
53. W. Palczewska, *Adv. Catal.*, 24, 245 (1975).
54. M. V. Goltsova, *Int. J. Hydrogen Energy*, 31, 223 (2006).
55. L. L. Jewell, B. H. Davis, *Appl. Catal. A*, 310, 1 (2006).
56. W. Drexel, A. Murani, D. Tocchetti, W. Kley, I. Sosnowska, D. K. Ross, *J. Phys. Chem. Solids*, 37, 1135 (1976).
57. Y. Z. Lu, Y. C. Wang, W. J. Chen, *J. Power Sources*, 196, 3033 (2011).
58. Y. Lu, Y. Jiang, H. Wu, W. Chen, *J. Phys. Chem. C*, 117, 2926 (2013).
59. D. Hao, S. Xue-Zhao, S. Cheng-Min, H. Chao, X. Zhi-Chuan, L. Chen, T. Yuan, W. Deng-Ke, G. Hong-Jun, *Chin. Phys. B*, 19, 10, 106104 (2010).
60. M. Jin, H. Zhang, Z. Xieb, Y. Xia, *Energy Environ. Sci.*, 5, 6352 (2012).

## Chaper 4 Preparation and Characterization of Pd-Pt Bimetallic Alloy on Graphene oxide and its Electrocatalytic Properties

### 4.1 Introduction

In recent years, great attention has been paid to develop renewable, clean and effective energy due to the increasing depletion of fossil energy and the gravity of environmental pollution. A great deal of work has been carried out extensively on the direct methanol fuel cells (DMFCs) due to their unique advantages, such as its high specific energy, portability and environmentally safe. The selection of anodic catalyst is exceptionally essential for the performance of the DMFCs. Considering extraordinary catalytic activity and stabilized chemical properties, platinum is the most important catalyst for the electrooxidation of low carbon chain aliphatic alcohol such as methanol and ethanol in DMFCs [1,2]. Pt has been widely used in fuel cell technology, where it acts as the most effective electrocatalyst for the electrooxidation of fuel (e.g., methanol) at the anode and electroreduction of oxygen at the cathode [3]. But, the catalyst made of a single Pt component can rarely meet the increasing demands of industrial applications at low costs due to its extreme shortage and high price [4]. It is also very challenging to enhance the mass activity of the monometallic catalyst of Pt because only the outmost few layers of Pt atoms in the catalyst are actually needed in catalyzing a reaction [5]. Furthermore, its vulnerability towards reaction poisons (e.g., CO poison) usually happening in the presence of Pt remains its serious limitation to many applications [6,7]. In order to address these problems, great efforts have been focused on the development of bimetallic structures that combine Pt with another metal having relatively cost-effective and plentiful features [8-10]. Among various metals, Pd has been identified as a promising candidate to form bimetals with Pt because they share the same facets structure and almost identical lattice constant (with a mismatch of only 0.77%) [11,12]. Both features are beneficial to the formation of bimetals with single crystallinity. Considerably, the incorporation of Pd into Pt-based bimetals cannot only significantly cut the cost of the catalysts by reducing the amount of Pt, but also exceedingly facilitate the enhancement or combined effect of the catalytic properties due to a strong coupling between these two metals [13-15].

The electrocatalytic properties of nano-sized metal alloy materials are sensitively dependent on size and composition [16]. This is why an accurate intrinsic correlation of alloy

particle composition with catalytic activity requires the availability of vigorous and preferably facile preparation techniques that provide independent control over composition [17]. Practically all physical or wet-chemical alloys nanoparticle synthesis techniques reported up till now fail to independently and precisely control size and composition and therefore often require pragmatic trial and error procedures to arrive at desired size or composition values [18]. Here, a facile CO-assisted synthesis of alloy nanoparticles are reported and represented using the PdPt bimetallic system. The synthesis is performed in Milli-Q water at elevated pressures of CO, but without the use of any long-chain expensive organic capping ligands. We show that the CO alone can be used to precisely control the alloy particle size and composition with just changing the precursor concentrations.

To this end, we have demonstrated the facile synthesis of PdPt bimetallic alloys and their enhanced activity for the preferential oxidation of methanol at the anodic end and reduction of oxygen at the cathodic end of a complete fuel cell. This work has been published in the Journal of Power Sources.

## 4.2 Oxygen Reduction Reaction (ORR)

The oxygen reduction reaction (ORR) is one of the most important and fundamental reactions due to its significance in e.g. fuel cell applications and metal air battery systems. ORR in acidic aqueous solutions occurs mainly by two pathways.

The direct 4-electron reduction pathway:



An indirect pathway occurs via hydrogen peroxide in two two-electron processes:



In the latter case hydrogen peroxide is made as an intermediate, which partly diffuses in the electrolyte phase. In direct methanol fuel cells (DMFCs), ORR is the reaction taking place at the cathode. In general, the ORR kinetics is very slow. In order to speed up the ORR kinetics to touch a practical usable level in a fuel cell, a cathode ORR catalyst is required. At the current stage in the market and technology, platinum based materials are the most practical and usable catalysts. The reaction pathways described earlier depends on the pH of the electrolyte, the presence or absence of adsorbing anions and on the catalyst material. A series reaction pathway is observed on graphite, most carbon materials as well as gold and mercury. Parallel existence of both the direct and the series pathway is found on Pt, Pt alloys, Pd, Pt-like metals, and Ag. Heterogeneous decomposition of peroxide is attained with Pt, Ag,

spinel, and perovskites. Generally in alkaline electrolyte the series pathway is improved compared to the direct pathway. It is more important here to note that in an acidic media, carbon materials do not show satisfactory catalytic activity for either of the pathways<sup>[19,20]</sup>. The most frequently used techniques for ORR catalysis studies are steady state polarization, cyclic voltammetry (CV) and rotating disk electrode (RDE). A steady state polarization curve defines the correlation between the electrode potential and the current density, which is recorded by either holding the electrode potential and recording the stable current response, or holding the current density and recording the stable potential response. The criteria to assess a polarization curve depend on its application. The procedure to describe the RDE method is governed by the Koutecky-Levich equation, which is as follows<sup>[21]</sup>.

$$\frac{1}{I} = \frac{1}{I_k} + \frac{1}{I_{lev}} \quad 4.4$$

where  $I$  is the disk current density,  $I_k$  is the kinetic current density, and  $I_{lev}$  is the Levich current density or diffusion current density.  $I_k$  can be further expressed as

$$I_k = nFAK_{O_2}C_{O_2}\Gamma_{catalyst} \quad 4.5$$

where  $n$  is the overall electron transfer number,  $A$  is the electrode area,  $C_{O_2}$  is the concentration of dissolved  $O_2$ , and  $\Gamma_{catalyst}$  is the surface concentration of the catalyst loading.

$I_{lev}$  can be expressed as

$$I_{lev} = 0.201nFAC_{O_2}^{\frac{2}{3}}D_{O_2}^{\frac{2}{3}}\nu^{-\frac{1}{6}}\omega^{\frac{1}{2}} \quad 4.6$$

where  $D_{O_2}$  is the diffusion coefficient of  $O_2$ ,  $\nu$  is the kinematic viscosity of the electrolyte solution, and  $\omega$  is the rotation rate represented by rpm.

For rotation disk electrode data study, three non-electrochemical kinetic parameters, such as the diffusion coefficient of  $O_2$ , the kinematic viscosity of the electrolyte solution, and the solubility of  $O_2$  must be known accurately. These parameters are all temperature dependent.

The ORR was well investigated on single crystal surfaces of various metals<sup>[21-23]</sup>. Research on the electrocatalytic activity of nanostructured and bimetallic surfaces has also been done<sup>[24-32]</sup>, but a comprehensive understanding is still missing. Therefore, ORR electrocatalysts with defined parameters are necessary to understand the origin of the catalytic properties. It is well described in the literature<sup>[21-26]</sup> that crystallographic orientation, morphology, and chemical composition are correlated to the catalytic activity. Grgur *et al.*,<sup>[26]</sup> reported an increased ORR activity from (111) < (100) < (110) orientation of Pt single crystals in aqueous  $H_2SO_4$ . Compared to pure Pt crystals a new possible approach for effective catalysts is to introduce 3d metals into the bulk or on the surface. Bimetallic systems such as Pt-Fe alloys were reported for the first time from Toda *et al.*,<sup>[30]</sup> here the ORR

activity is influenced by a so called Pt skin effect. The activity for ORR was found under definite circumstances to be twenty-five times higher compared to pure Pt. It was shown that the surface of such alloys consists of pure Pt and the reactivity decreases with increasing thickness of the skin layer. This effect is explained by a modified electronic structure of the skin layer compared to bulk Pt.

Stamenkovic *et al.*,<sup>[33-35]</sup> proposed bimetallic systems such as Pt<sub>3</sub>Ni, Pt<sub>3</sub>Ti, Pt<sub>3</sub>Fe, Pt<sub>3</sub>Co etc. Due to change in the electronic properties of Pt, the metal oxygen binding energy to bimetallic surfaces can be beneficially modified. These results were explained by different states of adsorbed oxygen resulting in different activation energies. Paulus *et al.*<sup>[27]</sup> reported experimental results which show an increase of the catalytic activity per Pt atom for different Pt alloys. Research by Schmidt *et al.*,<sup>[36]</sup> showed superior ORR electrocatalytic activity with Pd modified Au and Pt single crystals. Naohara *et al.*,<sup>[24,25]</sup> found a similar performance for the ORR for thin Pd overlayers on Au single crystals. Pd monolayer and alloy catalysts were also investigated by Shao *et al.*,<sup>[28,37]</sup>. He found higher catalytic activity for alloys and Pd monolayer supported on Ru, Rh, Pt and Au. The origin of this effect is described by a d-band center shift of the deposited overlayer<sup>[37]</sup>. Greeley *et al.*,<sup>[38]</sup> combined in recent study theoretical predictions of the experimental results by examining Pt alloyed with transition metals such as Sc and Y. An encouraging effect on the ORR activity, showed by positive half wave potential shift of up to 60mV, was found for polycrystalline Pt<sub>3</sub>Sc and Pt<sub>3</sub>Y electrodes which were also calculated to be a stable binary alloy.

## 4.3 Experimental Procedure

### 4.3.1 Chemicals and Materials

H<sub>2</sub>PdCl<sub>4</sub> (99.9 % metal basis, from Alfa Aesar), H<sub>2</sub>PtCl<sub>6</sub> (40% from Fluka), HClO<sub>4</sub> (from Sigma Aldrich), CH<sub>3</sub>OH (99.9% from J.T. Baker) and CO gas (99.9% purity). All reagents were used as received without further purification.

### 4.3.2 Synthesis of Graphene Oxide

The graphene oxide (GO) was prepared by the modified Hummers method<sup>[40]</sup> and reduced by NaBH<sub>4</sub>. The whole procedure is described in section 3.3.2.

### 4.3.3 Synthesis of Clean PdPt Alloy Nanocrystals on Graphene Oxide

The synthesized reduced graphene oxide (GO) powder was dispersed in water (1mg/1mL) and ultrasonicated for 30 minutes. Then  $\text{H}_2\text{PdCl}_4 + \text{H}_2\text{PtCl}_6$  solutions were added in GO dispersion with required atomic ratios (given in Table 1). Reaction flask was sealed and heated at  $90\text{ }^\circ\text{C}$  with continuous stirring and bubbling of CO as reducing and capping agent for 30 minutes. For comparison and to evaluate the effect of Pt addition with Pd, only clean Pd nanocrystals were also synthesized with the same method as adopted for alloys. The resulting product of clean Pd-Pt alloy nanocrystals were obtained and used as such for catalytic applications. There was no need to wash the nanoparticles because no any organic ligand or reducing chemical were used in synthesis, only CO was used as both reducing and capping agent. The adsorbed CO on the catalysts surface was removed by potential cycling in electrochemical experiments.

### 4.3.4 Characterization

The crystallite structure, size and morphology of the synthesized composites were studied by transmission electron microscopy (TEM), powder X-ray diffraction (XRD) (the measurements were performed with an X'pert PRO instrument, PANalytical, using Cu  $K\alpha$  radiation  $\lambda = 0.15418\text{ nm}$ ) and X-ray photoelectron spectroscopy (XPS) (the measurement were carried out using SPeCS system (PHOIBOS 150, Germany) with Al  $K\alpha$  radiation ( $h\nu = 1486.6\text{ eV}$ )).

### 4.3.5 Electrochemical Experiments

Before each electrochemical experiment, a glassy carbon (GC) electrode ( $0.196\text{ cm}^2$  geometric surface area) was first polished with alumina slurries ( $\text{Al}_2\text{O}_3$ ,  $0.05\text{ }\mu\text{m}$ ) on a polishing cloth to obtain a mirror finish, followed by sonication in  $0.1\text{ M HNO}_3$ ,  $0.1\text{ M H}_2\text{SO}_4$ , and pure water for 10 min, successively. To prepare a catalyst-coated working electrode,  $15\text{ }\mu\text{L}$  of the  $1\text{ mg/mL}$  suspension in pure water was drop-coated on the polished electrode surface by a microliter syringe, followed by drying in vacuum at room temperature. Afterward, the catalyst was covered with a thin layer of Nafion ( $0.1\text{ wt \%}$  in water,  $5\text{ }\mu\text{L}$ ) to ensure that the catalyst was tightly attached to the electrode surface during the electrochemical measurements. Voltammetry measurements were carried out with a CHI750D electrochemical workstation. The electrode prepared above was used as the working electrode. The Ag/AgCl (in  $3\text{ M NaCl}$ , aq.) combination isolated in a double junction chamber and a Pt coil was used as the reference and counter electrodes, respectively.

All the measurements were performed in electrochemical experiments with respect to standard values of reversible hydrogen electrode (RHE). Electrochemical experimental work was done by potential cycling method.

#### 4.3.6 Electrocatalytic Applications

Methanol oxidation reaction (MOR), oxygen reduction reaction (ORR) and methanol tolerant oxygen reduction reaction (MORR) applications were measured for all the synthesized catalysts.

### 4.4 Results and Discussion

#### 4.4.1 Morphology

The TEM images of the GO/Pd and GO/PdPt composites are shown in Figure 4.1. It is clearly observed from Figure 4.1a that well-dispersed Pd nanoparticles with an average size of 8 nm were successfully attached to the surfaces of GO. As the concentration of Pt increases in the GO/Pd composite system, a small aggregation of nanoparticles occur in the form of small clusters (Figure 4.1b, 4.1c, 4.1d), which makes a bimetallic alloy of PdPt. These clusters of bimetallic nanoparticles are homogeneously nucleated and dispersed on the GO sheets. The composition of the PdPt NPs was tuned by the amounts of precursors  $\text{H}_2\text{PdCl}_4$  and  $\text{H}_2\text{PtCl}_6$  added in the synthesis as shown in Table 1. In our experimental setup for the synthesis of mixed phase PdPt bimetallic alloys, there is a co-reduction of  $[\text{PdCl}_4]^{2-}$  and  $[\text{PtCl}_6]^{2-}$  ions with CO as reducing and capping agent. It is clear that the formation of these bimetallic nanoparticles can be attributed to the preferential chemisorption of CO on {111} rather than other facets.<sup>[41]</sup> As the amount of the Pt precursors was increased, the size of bimetallic nanoparticles increased due to a co-reduction overgrowth process. The chemisorption behavior of CO as a capping agent for Pd & Pt, in many catalytic studies caused poisoning due to the strong adsorption of CO on their surfaces, which could prevent other catalytic molecules from accessing to the catalytic surfaces. Surface scientists have frequently studied the adsorption of CO on various surfaces of Pd under vacuum conditions and also drawn the conclusion that CO exhibits strong adsorption on Pd and Pt surfaces and preferentially binds (111) facets<sup>[42,43]</sup>. During the reduction process CO molecules adsorbed on PdPt can be removed by applying a high temperature or an electrochemical oxidation potential, which makes it easy to clean the surface of the as-prepared CO-capped nanocrystals.



**Table 4.1** Table illustrating the composition and the electrochemical performance of different electrocatalysts towards methanol oxidation reaction (MOR).

Sample	Pd:Pt			<sup>a</sup> ECSA (m <sup>2</sup> .g <sup>-1</sup> )	<sup>b</sup> E <sub>onset</sub> (V) vs RHE	<sup>c</sup> If <sub>max</sub> (i/mA.cm <sup>-2</sup> ) w.r.t GSA
	Atomic ratio					
	Experimental	EDX	XPS			
GO/Pd	100:0			25.62	0.64	0.086
GO/Pd-Pt-01	83:17	86:14	84.61:15.39	32.51	0.60	0.397
GO/Pd-Pt-02	66:34	65:35	63.88:36.12	43.24	0.55	0.846
GO/Pd-Pt-03	40:60	38:62	36.58:63.42	55.89	0.50	4.35
GO/Pt	0:100			39.42	0.62	0.987

<sup>a</sup>ECSA = Electrochemical Active Surface Area, <sup>b</sup>E<sub>onset</sub> = Onset Potential for MOR activity, <sup>c</sup>If<sub>max</sub> (i/mAcm<sup>-2</sup>)  
<sup>2</sup>) w.r.t GSA= Maximum current for forward scan of MOR activity w.r.t Geometric Surface Area

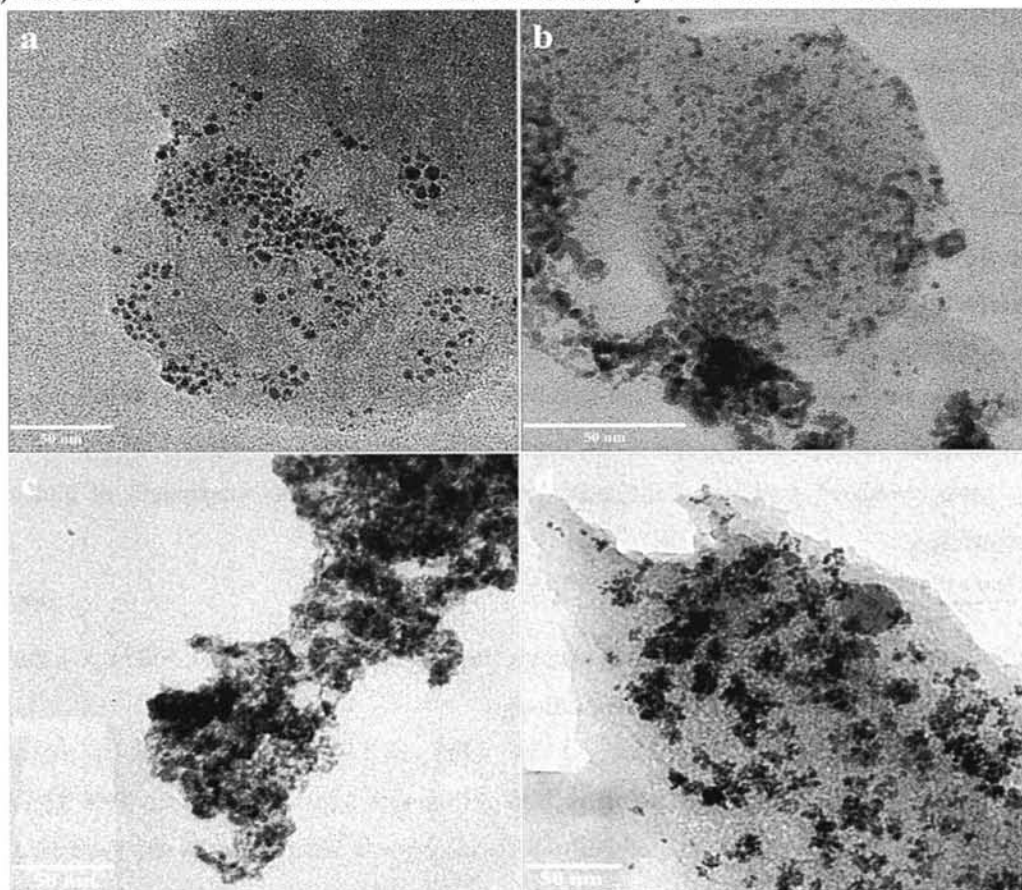


**Figure 4.1** TEM images of the (a) GO/Pd (b) GO/PdPt-01 (c) GO/PdPt-02 and (d) GO/PdPt-03 composites. The scale bar is 50 nm.

#### 4.4.2 Structural Characterization

The structural and crystalline phases of GO/Pd and GO/PdPt composites were identified by X-ray diffraction studies. As shown in Figure 4.2 the XRD patterns of GO/Pd composite, diffraction peaks at  $40.12^\circ$ ,  $46.06^\circ$  and  $68.45^\circ$  are ascribed to the (111), (200), and (220) crystalline planes of the face centered cubic (FCC) structure of Pd. The diffraction peaks are consistent with an FCC crystalline structure of bulk Pd (JCPDS, card no. 46-1043). Figure 4.2 also shows the X-ray diffraction patterns of GO/PdPt composites, which exhibit diffraction peaks of (111), (200) and (220) planes with an FCC crystalline structure. The relatively broad diffraction peak observed in all the samples at  $10^\circ$  to  $30^\circ$  centered at  $2\theta = 24.5^\circ$  corresponds to the (0 0 2) plane of graphene. All the peak positions of GO/PdPt composites are found to be slightly shifted to lower diffraction angles compared with that of GO/Pd composite. From the diffraction pattern of Pt (JCPDS, card no 04-0802), (111) peak is located at  $2\theta = 39.73^\circ$ . Considering the peak position of (111) more closely, it is evident that the peak position is changed from  $40.12^\circ$  (GO/Pd) to  $39.79^\circ$  (GO/PdPt-03) by increasing the concentration of Pt. For GO/PdPt composites, the diffraction peak values of (111) i.e.,  $39.96^\circ$ ,  $39.85^\circ$  and  $39.79^\circ$  is in between those of GO/Pd ( $40.12^\circ$ ) and Pt nanoparticles ( $39.73^\circ$ ). These results could be attributed to the addition of Pt to Pd for the difference in atomic size ( $Pt > Pd$ ) and also an indication that Pd and Pt nanoparticles are well-mixed and form alloy nanoparticles.<sup>[44,45]</sup> Alloying degrees of the bimetallic GO/PdPt composite were calculated from XRD using Vegard's law.

$$a_{(PdPt)} = a_{(Pd)} - kx_{(Pt)} \quad 4.7$$

where  $a_{(PdPt)}$  and  $a_{(Pd)}$  are the lattice parameters of PdPt/GO alloy and Pd/GO,  $k$  and  $x_{(Pt)}$  lattice constant and atomic fraction of Pt, respectively. The lattice parameters of GO/PdPt alloy were calculated from the (220) peak position ( $\theta_{max}$ ) and the wavelength of  $CuK_\alpha$  radiation ( $\lambda_{k\alpha}$ ).

$$a = \frac{\lambda(h^2 + k^2 + l^2)^{\frac{1}{2}}}{2\sin\theta} \quad 4.8$$

where  $a$ ,  $\lambda$ ,  $\theta$  and  $(hkl)$  are the lattice parameters, the wavelength of X-ray ( $1.54056 \text{ \AA}$ ), the peak position and the planes of atoms, respectively.

The lattice parameters obtained were 3.894, 3.903 and 3.914  $\text{\AA}$  for GO/PdPt-01, PdPt-02 and PdPt-03, respectively. The atomic fraction of Pt inserted into Pd calculated from XRD data was 16.5. The alloying degree of PdPt in the catalysts is determined by the following equation.

$$\text{Alloying degree} = \frac{x_{Pt}}{1 - x_{Pt}(\frac{Pt}{Pd})_{actual}} \quad 4.9$$

where  $(\text{Pt/Pd})_{\text{actual}}$  is the actual atomic ratio. The alloying degrees calculated for GO/PdPt-01, PdPt-02 and PdPt-03 were 65, 71, and 84%, respectively.

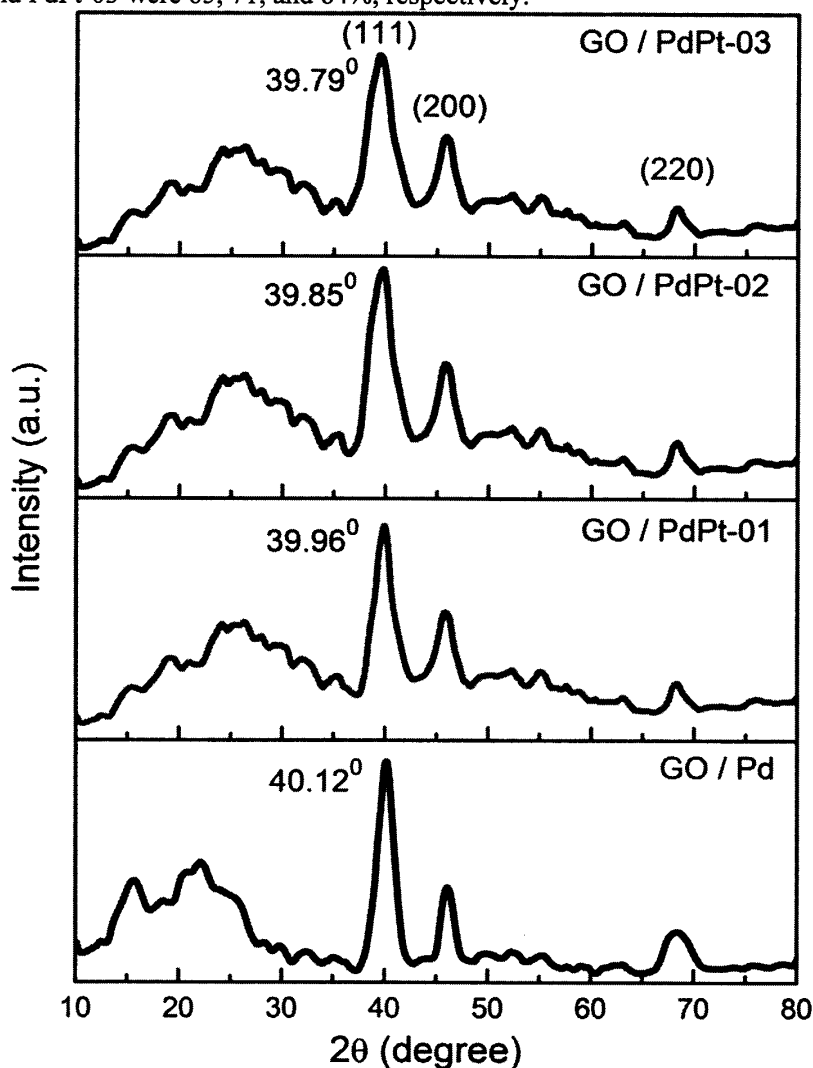
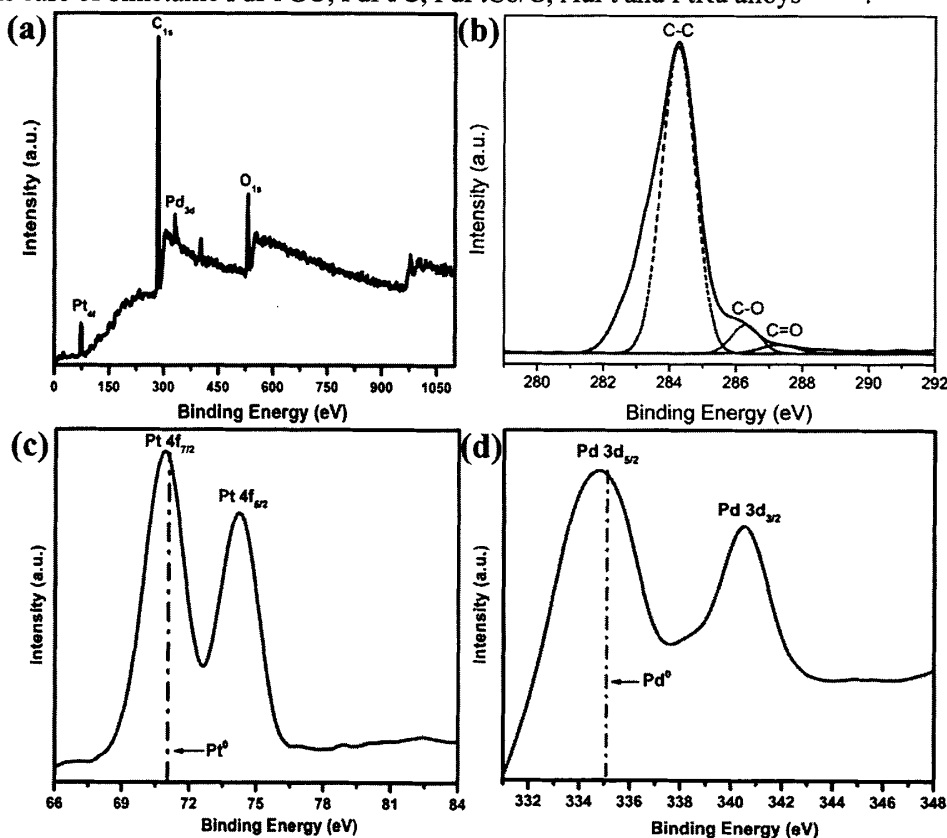


Figure 4.2 XRD patterns of GO/Pd and GO/PdPt composites.

XPS was employed to determine the surface elemental composition of the bimetallic GO/PdPt-03 composite as shown in Figure 4.3. As displayed in Figure 4.3a, the XPS survey-spectrum indicates only platinum, palladium, oxygen, nitrogen and carbon. The C1s XPS results shown in Figure 4.3b reveal the formation of various surface groups on the obtained composite. The spectra could be reasonably deconvoluted into three main components corresponding to the following carbon functional groups: C-C (284.5 eV), C-O (286.5 eV) and C=O (287.9 eV) [46,47]. The peak intensity associated with C-C bonds indicates that the  $\text{sp}^2$ -hybridized graphitic structure is predominant in the graphene support, while the peak

composed of oxygenated functional groups was substantially reduced. The XPS profile of the GO/PdPt-03 composite also shows signatures for both Pt and Pd (Figure 4.3c and 4.3d). The spectrum of  $4f_{5/2}$  and  $4f_{7/2}$  electrons of Pt appeared at 74.6 eV and 71.8 eV, respectively, with an asymmetric nature, corresponding to the metallic Pt(0) state. Similarly, the spectrum of  $3d_{5/2}$  and  $3d_{3/2}$  electrons for Pd appears at 334.9 eV and 340.6 eV, respectively, corresponding to the metallic Pd(0) state. Compared to the standard metallic Pt(0) and Pd(0) states, these values are slightly shifted to lower binding energies, suggesting that the electrons transfer to Pt and Pd metals. Due to the large  $\pi$ - $\pi$  conjugation on graphene, it can be rationally presumed that these electrons were from graphene, which would be evidence of a significant interaction between the bimetallic PtPd alloy nanoparticles and graphene. The shifts in the binding energy of Pt and Pd in bimetallic PtPd catalysts indicate a change in the electronic structure of Pt and Pd, which could be attributed to the electronic interactions between Pt and Pd atomic orbitals, leading to electron transfer from Pd to Pt due to the higher electronegativity of Pt, (2.28) compared to Pd (2.20). Such a variation has been also observed in the literature in the case of bimetallic PdPt/GO, PdPt/C, PdPtCo/C, AuPt and PtRu alloys [48-51].



**Figure 4.3** XPS spectra of (a-d) GO/PdPt-03 sample. Observed regions were (b) C1s with deconvolution results, (c) Pt4f and (d) Pd3d.

The surface composition of catalysts can be evaluated by XPS and EDX. Both techniques allow the estimation of the chemical composition, but while for the EDX the penetration depth of the X-ray probe is usually in the micrometer range, for the XPS the penetration depth is normally within the first nanometers. Thus, we can assume that by using both techniques we can differentiate between the bulk and the near-surface chemical composition with in the 10-20 nm range particle size. The EDX and XPS results are summarized in Table 1. As shown in Table 1, the surface Pd/Pt atomic ratio of GO/PdPt composites are smaller than that of the bulk atomic ratio determined by EDX, indicating that all of GO/PdPt composites had Pt rich surfaces.

#### 4.4.3 Electrochemical Performance

The as-synthesized mixed phase alloys with different Pd/Pt atomic ratios were evaluated as electrocatalysts for methanol oxidation (MOR), oxygen reduction reaction (ORR), methanol tolerant oxygen reduction reaction (MORR). In order to calculate the electrochemical active surface area (ECSA), the cyclic voltammograms (CVs) curves of GO/Pd, GO/Pt and GO/PdPt were recorded at room temperature in  $N_2$  purged 0.1 M  $HClO_4$  aqueous solution at a sweep rate of  $50 \text{ mV s}^{-1}$ . As shown in Figure 4.4, there is hydrogen adsorption/desorption region (0.05-0.3 V) and surface metal oxidation/reduction region (0.4-0.8 V) on the CV curves for all the three catalysts. From these CVs, their ECSAs were determined by integrating the area bounded by the hydrogen adsorption curve and the baseline in the range of 0.05-0.4 V (see Table 1). The ECSA value can be calculated by  $Q_H/mq$ , where  $Q_H$  is the total electric charge of hydrogen adsorption and desorption on the PtPd nanoparticles,  $m$  is the catalyst loading on the glassy carbon electrode in g and the charge of each actual active area assumed to be  $210 \mu\text{Ccm}^{-2}$  [52,53]. Figure 4.4 and Figure 4.5 compare the base CVs and LSV, respectively, of these catalysts in 0.1M  $HClO_4$  solution at a scan rate of  $50 \text{ mV s}^{-1}$ . The value of ECSA calculated for GO/PdPt-03 was found to be  $55.89 \text{ m}^2\text{g}^{-1}$ , which is higher than GO/Pd, GO/Pt and other GO/PdPt composites. The increase in ECSA should be attributed to optimized dispersion and size distribution of the PdPt NPs on GO.

The electrocatalytic behaviors of GO/Pd and GO/PdPt catalysts toward methanol oxidation were characterized by cyclic voltammogram measurement shown in Figure 4.6. The CV measurements of the samples were carried out initially in  $N_2$ -purged 0.5 M  $HClO_4$  containing 1 M  $CH_3OH$  aqueous solution at a sweep rate of  $50 \text{ mVs}^{-1}$ . As shown in Figure 6, each of curves includes a methanol oxidation peak during the forward scan at around 0.7-1.1

V and another anodic peak during the reverse scan related to the removal of incompletely oxidized carbonaceous species such as CO formed in the forward scan.

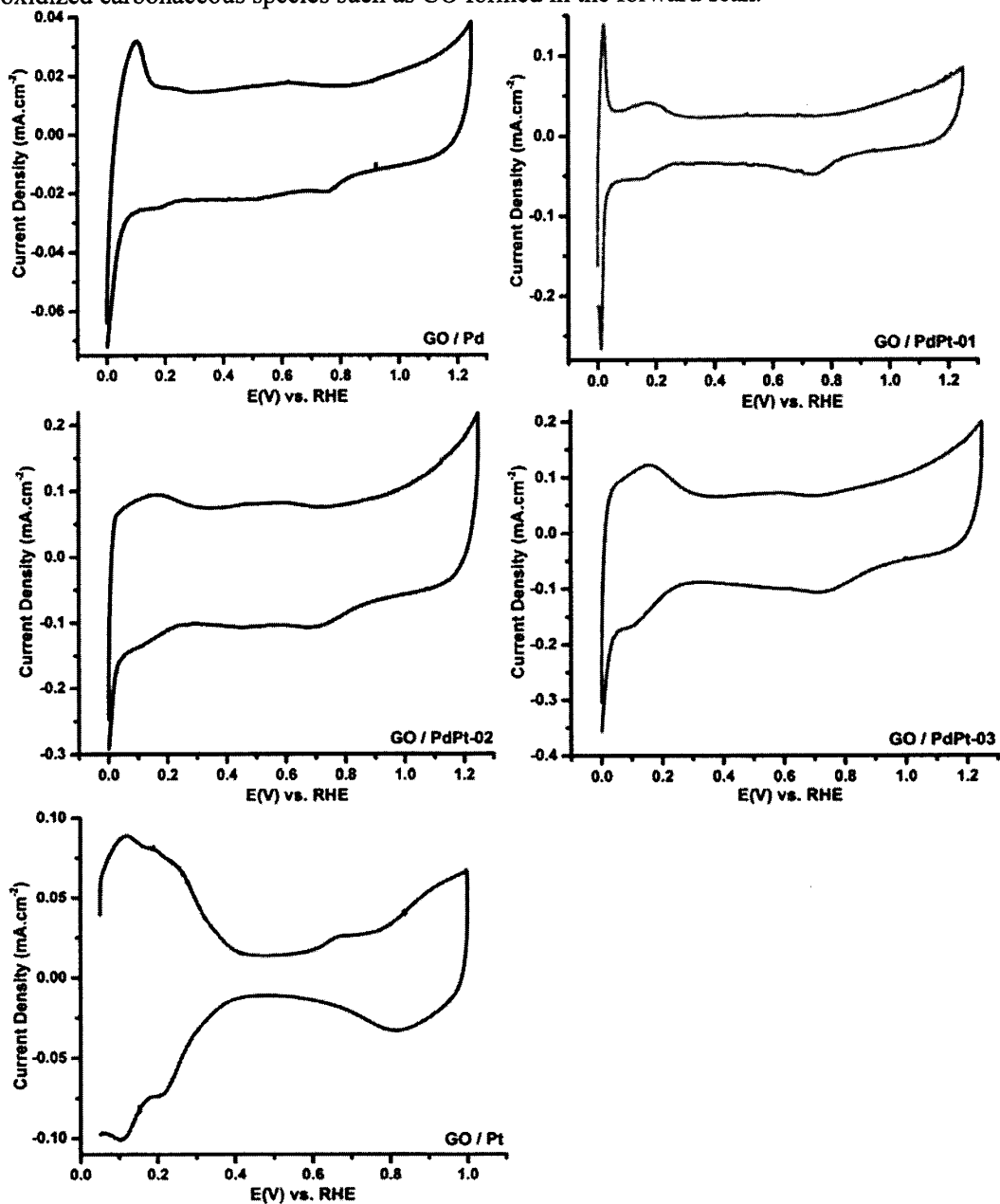


**Figure 4.4** Base CVs of GO/Pd, GO/Pt and GO/PdPt composites in 0.1 M HClO<sub>4</sub> at a scan rate of 50 mV/s vs RHE.

The onset potential of methanol oxidation observed with GO/PdPt-03 was 0.50 V, while that for GO/Pd and GO/Pt was 0.64V and 0.62 V, respectively. The onset potential with respect to the electro-oxidation mechanism of alcohol on Pt catalysts is basically related to

the breaking of C-H bonds and subsequent removal of intermediates such as  $\text{CO}_{\text{ad}}$  by the oxidation with  $\text{OH}_{\text{ad}}$  supplied by Pt-OH sites or other sources to the electro-oxidation mechanism of alcohol on Pt catalysts [54,55]. This result indicates that the bimetallic GO/PdPt demonstrated better performance for the promotion of C-H breaking and  $\text{CO}_{\text{ad}}$  tolerance in the methanol electro-oxidation. The maximum current density observed for GO/PdPt-03 was  $4.35 \text{ mA cm}^{-2}$  in the forward scan, while for GO/Pd and GO/Pt, it was 0.086 and  $0.987 \text{ mA cm}^{-2}$ , respectively. This maximum current density and enhanced catalytic activity of bimetallic PdPt alloy over pure Pd and Pt metals could be attributed to the bi-functional mechanism. (1) The synergistic effect between Pt and Pd metals, which has also been confirmed in the literature and to (2) the ligand effect. According to the d-band theory of Hammer Nørskov, the d-band center of Pd will be shifted upward when it is combined with Pt because the lattice constant of Pt ( $3.92 \text{ \AA}$ ) is larger than that of Pd ( $3.89 \text{ \AA}$ ), which is consistent with the XPS observations of the negative shift of the binding energy for Pd in binary PtPd catalysts [56]. The increased electron density around Pt would then cause partial filling of Pt 5d bands, resulting in the downward shift of the d-band center and the weakening of CO adsorption on Pt and potentially decreasing the CO poisoning effect, thus enhancing the activity towards methanol oxidation.

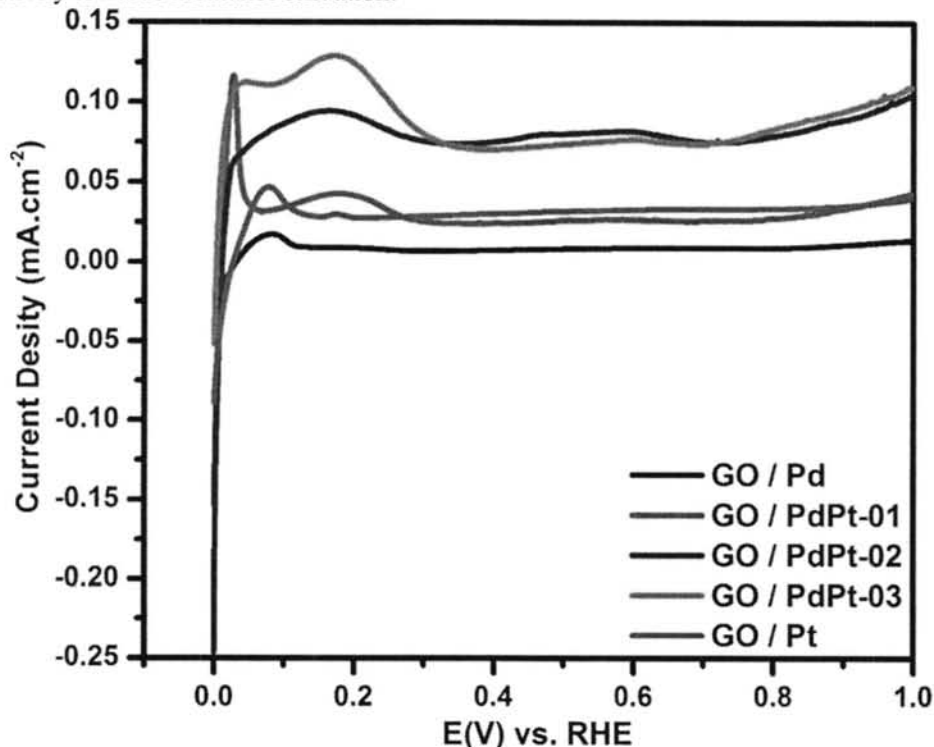


**Figure 4.5** LSV peaks of GO/Pd, GO/Pt and GO/PdPt composites in 0.1 M  $\text{HClO}_4$  at a scan rate of 50  $\text{mV/s}$  vs RHE.

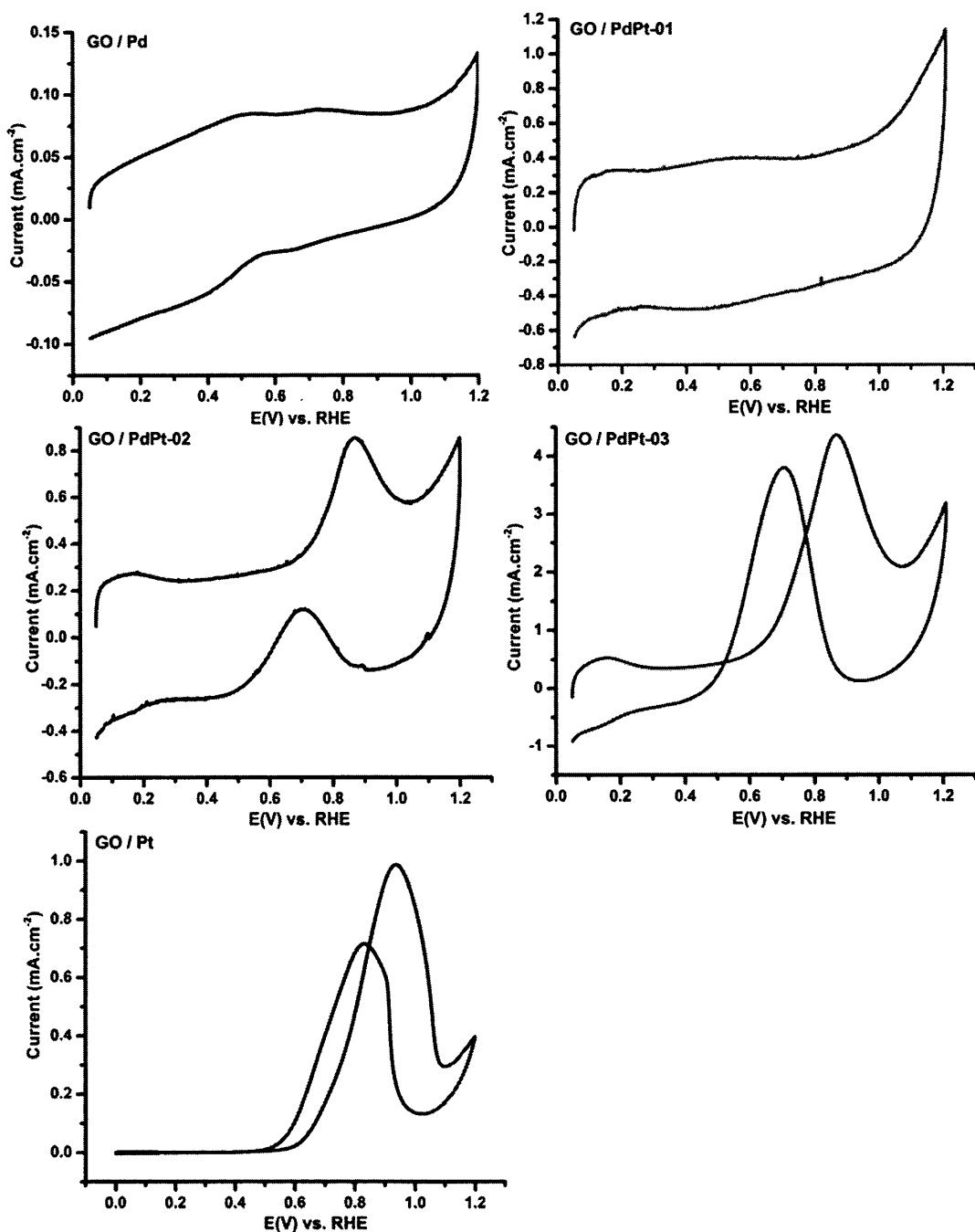


**Figure 4.6** MOR activity peaks (forward and backward scans) of GO/Pd, GO/Pt and GO/PdPt composites w.r.t geometric surface area in 0.1 M HClO<sub>4</sub> + 1M CH<sub>3</sub>OH at a scan rate of 50 mV/s vs RHE.

The half-wave potential ( $E_{1/2}$ ) of GO/PdPt-03 has been determined to be 0.609 V, which is 60 and 68 mV higher than that of GO/Pt and GO/Pd catalysts, respectively. The diffusion-limiting currents were obtained in the potential region below 0.4 V, whereas a mixed kinetic-



diffusion control region occurs between 0.4 and 0.8 V. The kinetic current can be calculated based on the Koutecky-Levich equation:

$$\frac{1}{i} = \frac{1}{i_k} + \frac{1}{i_d} \quad 4.10$$

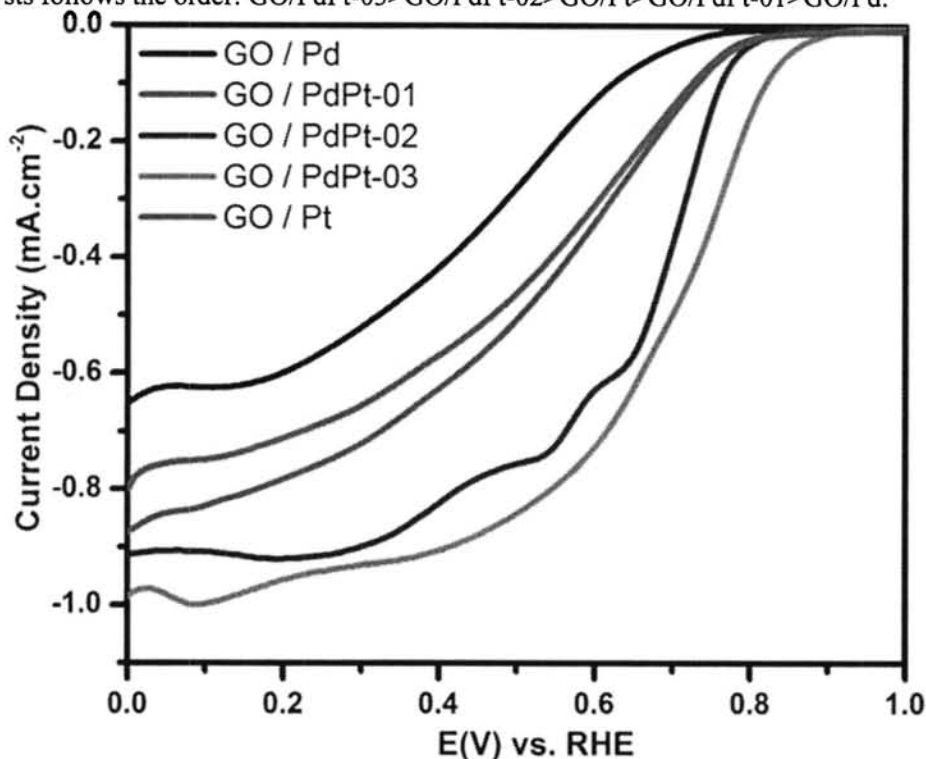
where  $i$  is the experimentally measured current,  $i_d$  is the diffusion-limiting current, and  $i_k$  is the kinetic current. Thus, the kinetic current can be calculated by the following equation.

$$i_k = \frac{i \times i_d}{i_d - i} \quad 4.11$$

$$\text{mass activity} = \frac{i_k}{m} \quad 4.12$$

where  $m$  is the amount of the catalyst loading.

The diffusion-limiting currents assumed to be strongly affected by the structure of the catalyst support material. The kinetic current calculated to be 0.85 V. The ORR activities were calculated at 0.85 V vs. RHE with a rotation speed of 900 rpm. Among the three GO/PdPt catalysts, GO/PdPt-03 exhibits the highest ORR activity and the ORR of all the catalysts follows the order: GO/PdPt-03 > GO/PdPt-02 > GO/Pt > GO/PdPt-01 > GO/Pd.



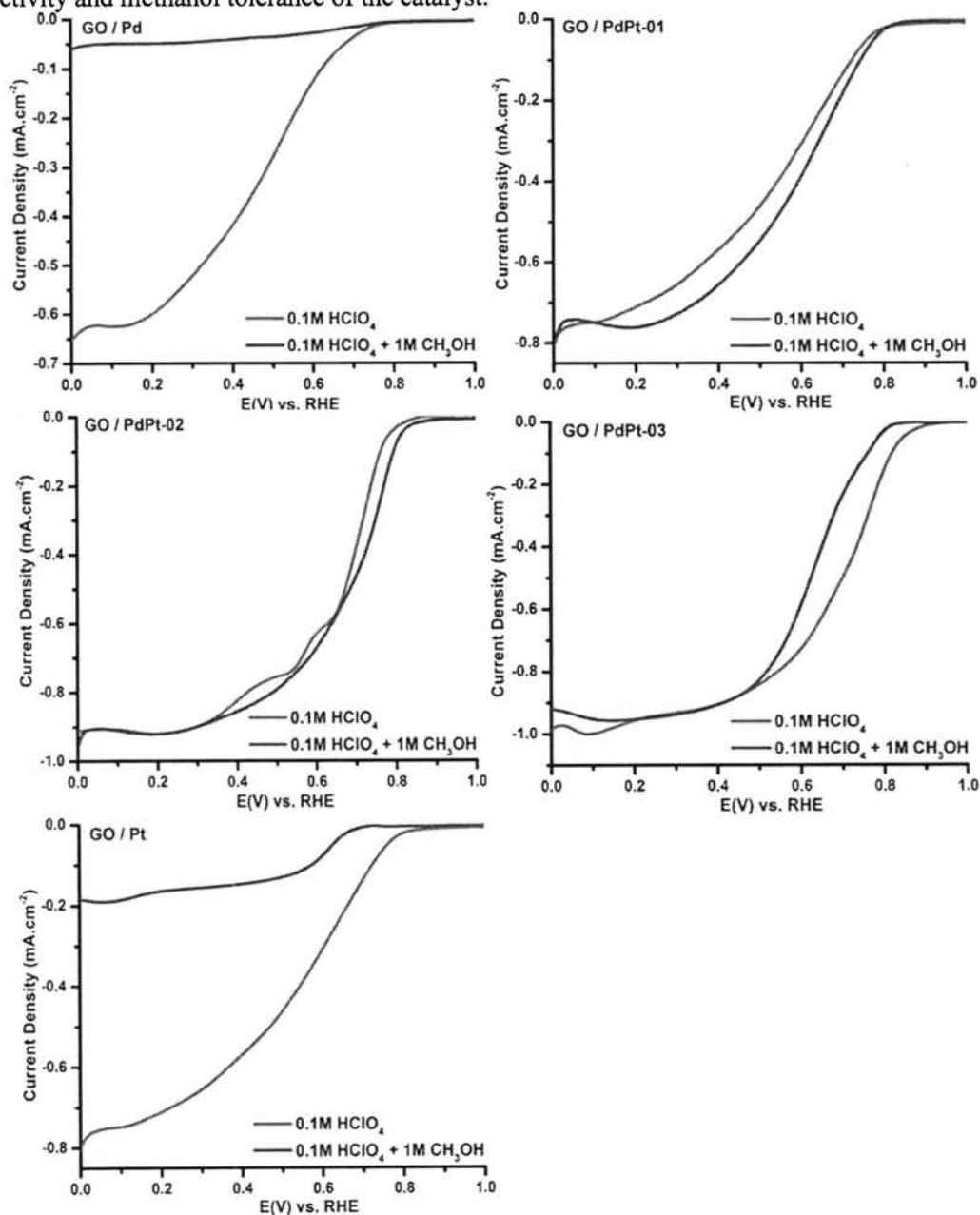
**Figure 4.7** ORR polarization curves of GO/Pd and GO/PdPt composites in 0.1M HClO<sub>4</sub> at a scan rate of 50 mV/s vs RHE.

Figure 4.7 shows a comparison for the ORR of all the synthesized catalysts under similar experimental conditions. On the other hand, although the polarization curves of the Pd catalyst showed a well-defined current density in the diffusion-limited region, but its onset

potential for ORR is much more positive than PdPt alloy catalysts. Therefore, the ORR activity order is as follows: Pd catalyst is characterized by lower intrinsic activity for ORR compared to PdPt bimetallic catalysts. This is a clear indication of a better specific activity due to a larger occurrence of active sites from PdPt collectively on the surface and lower interaction with the support that provides a larger availability of catalytic sites for the ORR. The open circuit potential of GO/PdPt alloy catalysts in oxygen saturated solution is slightly higher than that of GO/Pd, suggesting that the oxygen adsorption on the alloy surface is more favored than that of Pd. Such evidence indicates that the activity of GO/PdPt alloys may be further increased by adding optimum composition of both the metals. The fuel cell tests done in the literature with Pt catalysts supported on GO, used as cathode material, have shown lower performance than the Pt catalysts supported on C. It was believed that the ORR diffusion-limiting currents were strongly affected by the structure of the catalyst supporting material [57]. Also the pure Pt based catalysts showed poisoning problems during electro experiments. To avoid from poisoning factor Pd is combined with Pt. That is also proved from the present results that PdPt bimetallic alloys have shown good ORR activity with characteristic diffusion and kinetic currents.

It is well known that the crossover of methanol from the anode to the cathode leads to the reduction of cell voltage in between 200 mV and 300 mV. Figure 4.8 shows the MORR activity GO/Pd and GO/PdPt catalysts in the absence and presence of 1 M methanol. Methanol tolerance seems to be common with all GO/PdPt catalysts. A cathodic shift of 100 mV in the onset potential of GO/PdPt composites is observed, which may be attributed to the small influence of methanol. The high activity of these GO/PdPt methanol-tolerant catalysts for oxygen reduction could be ascribed to the surface composition effect and the disordered surface structure of the GO/PdPt catalysts. Of course, a uniform dispersion of the GO/PdPt catalysts in this work can also be an important factor in determining their activity for ORR in the presence of methanol. Among the three GO/PdPt catalysts, GO/PdPt-03 exhibits the highest tolerance to methanol and the methanol tolerance of all the catalysts follows the order: GO/PdPt-03>GO/PdPt-02>GO/PdPt-01>GO/Pt>GO/Pd. Methanol tolerance of the catalysts could also be maintained by irreversible adsorption of Pd from the solution to catalysts surface [58]. The GO/PdPt-03 catalyst is found to be methanol-tolerant and exhibits higher mass activity in the presence of methanol. However, it is interesting to note that no methanol oxidation peak appeared in the oxygen reduction polarization curves of GO/PdPt-03, GO/PdPt-02 and GO/PdPt-01 catalysts and the half-wave potentials are shifted slightly to less cathodic values, which in principle indicated that these catalysts possess superior

selective ORR activity in the presence of methanol. Thus, Pd is an interesting system to have a control over the activity of the surface for methanol oxidation reaction and ORR. These Pd-containing catalysts showed an oxygen reduction to the same extent both in the presence and absence of methanol although Pd is more oxophilic than Pt. It is likely that some other factors that we do not understand at this time may also influence the balance between the ORR activity and methanol tolerance of the catalyst.



**Figure 4.8** MORR polarization curves of GO/Pd and GO/PdPt composites in 0.1M HClO<sub>4</sub> + 1M CH<sub>3</sub>OH at a scan rate of 50 mV/s vs RHE.

## 4.5 Summary

We have demonstrated a novel and facile route for the anchoring of bimetallic PdPt nanoparticles of different compositions on graphene sheets. Structural and morphological characterizations of GO/PdPt composites are performed using X-ray diffraction, X-ray photoelectron spectroscopy analysis and transmission electron microscopy. It is found that PdPt bimetallic nanoparticles are successfully synthesized and uniformly attached on the graphene sheets. The electrocatalytic and electrochemical properties of GO/PdPt composites including methanol oxidation reaction (MOR), oxygen reduction reaction (ORR) and methanol tolerant oxygen reduction reaction (MTORR) are studied in HClO<sub>4</sub> aqueous solution. The as-synthesized GO/PdPt composites showed higher electrocatalytic activity, higher specific ORR activity and excellent poisoning tolerance for the methanol electro-oxidation compared with graphene supported monometallic catalyst (GO/Pd), due to the combined effect of the composite with unique properties of graphene and alloying of Pd with Pt. In particular, the prepared GO/PdPt composites with an (Pd:Pt) atomic ratio of 40:60 exhibits higher methanol oxidation activity with a larger ECSA, lower onset potential, higher  $I_F/I_B$  ratio and high peak current density. The results can be attributed to the collective effects of the PdPt nanoparticles and the enhanced electron transfer of graphene. Furthermore, our synthetic approach can be universally applied to decorate high quality graphene with different combination of alloys, which demonstrated much larger ECSA, improved efficiency for methanol oxidation to carbon dioxide and long-term stability.

## 4.6 References

1. O. Winjobi, Z. Zhang, C. Liang, W. Li, *Electrochimica Acta* 55 (2010) 4217-4221.
2. Y.W. Lee, M. Kim, Y. Kim, S.W. Kang, J. Lee, S.W. Han, *Journal of Physical Chemistry C* 114 (2010) 7689-7693.
3. M. Debe, *Nature* 486 (2012) 43-51.
4. J. Wu and H. Yang, *Acc. Chem. Res.* 46 (2013) 1848-1857
5. N. Porter, H. Wu, Z. Quan, J. Fang, *Acc. Chem. Res.* 46 (2013) 1867-1877
6. P. Ferrin, A. Nilekar, J. Greeley, M. Mavrikakis, J. Rossmeisl, *Surf. Sci.* 602 (2008) 3424-3431.
7. J. Gu, Y. Zhang, F. Tao, *Chem. Soc. Rev.* 41 (2012) 8050-8065.
8. J. Wu, P. Li, Y. Pan, S. Warren, X. Yin, H. Yang, *Chem. Soc. Rev.* 41 (2012) 8066-9074.

9. D. Wang, Y. Li, *Adv. Mater.* 23 (2011) 1044-1060.
10. M. Liu, R. Zhang, W. Chen, *Chem. Rev.* 114 (2014) 5117-5160.
11. B. Lim, M. Jiang, P. Camargo, E. Cho, J. Tao, X. Lu, Y. Zhu, Y. Xia, *Science* 324 (2009) 1302-1305.
12. K. Sasaki, H. Naohara, Y. Cai, Y. Choi, P. Liu, M. Vukmirovic, J. Wang, R. Adzic, *Angew. Chem. Int. Ed.* 49 (2010) 8602-8607.
13. V. Stamenkovic, B. Mun, M. Arenz, K. Mayrhofer, C. Lucas, G. Wang, P. Ross, N. Markovic, *Nat. Mater.* 6 (2007) 241-247.
14. J.K.Norskov, T. Bligaard, J. Rossmeis, C.H. Christensen, *Nat. Chem.* 1 (2009) 37-46.
15. Y. Lu, Y. Jiang, X. Gao, X. Wang, H. Wu, W. Chen, *J. Am. Chem. Soc.* 136 (2014) 11687-11697.
16. V.R. Stamenkovic, B. Fowler, B.S. Mun, G.F. Wang, P.N. Ross, C.A. Lucas, N.M. Markovic, *Science* 315 (2007) 493-497.
17. C. Cui, L. Gan, M. Heggen, S. Rudi, P. Strasser, *Nat. Mater.* 12 (2013) 765-771.
18. C. Wang, N.M. Markovic, V.R. Stamenkovic, *Acs Catalysis* 2 (2012) 891-898.
19. E. Yeager, *Electrochim. Acta*, 29 (1984) 1527.
20. E. Yeager, *J. Mol. Catal.*, 38 (1986) 5.
21. N. M. Markovic and P. N. Ross, *Surf. Sci. Rep.*, 45 (2002) 121.
22. N. M. Markovic, R. R. Adzic, B. D. Cahan, and E. B. Yeager, *J. Electroanal. Chem.*, 377 (1994) 249.
23. N. M. Markovic, H. A. Gasteiger, and P. N. Ross, *J. Phys. Chem.*, 99 (1995) 3411.
24. H. Naohara, S. Ye, and K. Uosaki, *J. Electroanal. Chem.*, 500 (2001) 435.
25. H. Naohara, S. Ye, and K. Uosaki, *Electrochim. Acta*, 45 (2000) 3305.
26. B. N. Grgur, N. M. Markovic, and P. N. Ross, *Can. J. Chem.*, 75 (1997) 1465.
27. U. A. Paulus, A. Wokaun, G. G. Scherer, T. J. Schmidt, V. Stamenkovic, N. M. Markovic, and P. N. Ross, *Electrochim. Acta*, 47 (2002) 3787.
28. M. H. Shao, P. Liu, J. L. Zhang, and R. Adzic, *J. Phys. Chem. B*, 111 (2007) 6772.
29. V. Stamenkovic, B. S. Mun, K. J. J. Mayrhofer, P. N. Ross, N. M. Markovic, J. Rossmeisl, J. Greeley, and J. K. Nørskov, *Angew. Chem., Int. Ed.*, 45 (2006) 2897.
30. T. Toda, H. Igarashi, H. Uchida, and M. Watanabe, *J. Electrochem. Soc.*, 146 (1999) 3750.
31. T. J. Schmidt, V. Stamenkovic, M. Arenz, N. M. Markovic, and P. N. Ross, *Electrochimica Acta*, 47 (2002) 3765.

32. K. Sasaki, Y. Mo, J. X. Wang, M. Balasubramanian, F. Uribe, J. McBreen, and R. R. Adzic, *Electrochimica Acta*, 48 (2003) 3841.
33. V. Stamenkovic, B. S. Mun, K. J. J. Mayrhofer, P. N. Ross, N. M. Markovic, J. Rossmeisl, J. Greeley, and J. K. Nørskov, *Angew. Chem. Int. Edn*, 45 (2006) 2897.
34. V. R. Stamenkovic, B. Fowler, B. S. Mun, G. F. Wang, P. N. Ross, C. A. Lucas, and N. M. Markovic, *Science*, 315 (2007) 493.
35. V. R. Stamenkovic, B. S. Mun, M. Arenz, K. J. J. Mayrhofer, C. A. Lucas, G. F. Wang, P. N. Ross, and N. M. Markovic, *Nat. Mater.*, 6 (2007) 241.
36. T. J. Schmidt, V. Stamenkovic, M. Arenz, N. M. Markovic, and P. N. Ross, *Electrochim. Acta*, 47 (2002) 3765.
37. M. H. Shao, T. Huang, P. Liu, J. Zhang, K. Sasaki, M. B. Vukmirovic, and R. R. Adzic, *Langmuir*, 22 (2006) 10409.
38. J. Greeley, I. E. L. Stephens, A. S. Bondarenko, T. P. Johansson, H. A. Hansen, T. F. Jaramillo, J. Rossmeisl, I. Chorkendorff, and J. K. Nørskov, *Nat. Chem.*, 1 (2009) 552.
39. Bard AJ, Faulkner LR. *Electrochemical methods: fundamentals and applications*. New York: Wiley, 1980.
40. W.S. Hummers, R.E. Offeman, Preparation of graphitic oxide, *J. Am. Chem. Soc.* 80 (1958) 1339-1339.
41. H. Zhang, M. Jin, J. Wang, W. Li, P. Camargo, M. Kim, D. Yang, Z. Xie, Y. Xia, *J. Am. Chem. Soc.* 133 (2011) 6078-6089.
42. J. Szanyi, W. K. Kuhn, D. W. Goodman, *J. Vac. Sci. Technol.* 11 (1993) 1969-1974.
43. A.B. Anderson, M. K. Awad, *J. Am. Chem. Soc.* 107 (1985) 7854-7857.
44. J. Datta, A. Dutta, S. Mukherjee, *Journal of Physical Chemistry C* 115 (2011) 15324-15334.
45. Y. Zhang, G. Chang, H. Shu, M. Oyama, X. Liu, Y. He, *J. Power Sources* 262 (2014) 279-285.
46. T.I.T. Okpalugo, P. Papakonstantinou, H. Murphy, J. McLaughlin, N.M.D. Brown, *Carbon* 43 (2005) 153-161.
47. K.R. Lee, K.U. Lee, J.W. Lee, B.T. Ahn, S.L. Woo, *Electrochem. Commun.* 12 (2010) 1052-1055.
48. Y. Lu, Y. Jiang, H. Wu, W. Chen, *J. Phys. Chem. C* 117 (2013) 2926-2938.
49. C.-W. Yi, K. Luo, T. Wei, D.W. Goodman, *J. Phys. Chem. B.* 109 (2005) 18535-18540.
50. C. Xu, L. Wang, X. Mu, Y. Ding, *Langmuir* 26 (2010) 7437-7443.
51. Y. Lu, Y. Jiang, W. Chen, *Nanoscale* 6 (2014) 3309-3315.

52. X. Huang, H. Zhang, C. Guo, Z. Zhou and N. Zheng, *Angew. Chem., Int. Ed.* 48 (2009) 4808-4812.
53. Y. Xiong, H. Cai, B. Wiley, J. Wang, M. Kim and Y. Xia, *J. Am. Chem. Soc.* 127 (2007) 3665-3675.
54. Y. Liu, M. Chi, V. Mazumder, K. More, S. Soled, J. Henao and S. Sun, *Chem. Mater.* 23 (2011) 4199-4203.
55. Z. Liu, X. Ling, X. Su and J. Lee, *J. Phys. Chem. B* 108 (2004) 8234-8240.
56. J. Rossmesl, P. Ferrin, G. Tritsarlis, A. Nilekar, S. Koh, S. Bae, S. Brankovic, P. Strasser, M. Mavrikakis, *Energy Environ. Sci.*, 5 (2012) 8335-8342.
57. A.H.A. Monteverde Videla, L. Zhang, J. Kim, J. Zeng, C. Francia, J. Zhang, S. Specchia, *Journal of Applied Electrochemistry* 43 (2013) 159-169.
58. G.A. Attard, A. Bannister, *J. Electroanal. Chem.*, 300 (1991) 467-485.

## Chaper 5 Synthesis and Characterization of MoS<sub>2</sub>/GO-CNT Composite for Electrocatalytic Application of Hydrogen Evolution Reaction

### 5.1 Introduction

Hydrogen is considered to be the cleanest and a promising next generation fuel resource. Utilization of hydrogen as a promising candidate of future energy requires environment friendly, economical and efficient H<sub>2</sub> production. Hydrogen production from water splitting is the most reliable and cost effective method and has attracted great importance and attention in the last decade <sup>[1-4]</sup>. The most effective catalyst for electrochemical hydrogen evolution reaction (HER) should have the minimum potential to reduce the overpotential and increase the efficiency of this significant electrochemical process <sup>[5-12]</sup>. Up till now, Pt is considered to be one of the most promising electrocatalyst for the production of hydrogen from water splitting reactions <sup>[13]</sup>. But, the catalyst made of a Pt component can rarely meet the increasing demands of industrial applications at low costs due to its extreme shortage and high price <sup>[14-16]</sup>. In order to change Pt with a new catalyst that are most abundant in nature and cost effective is a challenging part of the research.

To this end, researchers have proposed a number of efficient electrocatalysts for HER reactions involving carbides, <sup>[17]</sup> metal alloys, <sup>[18]</sup> and transition-metal chalcogenides <sup>[19]</sup>. Among these catalysts, two-dimensional MoS<sub>2</sub> with exposed edges demonstrated very promising electrocatalytic activity towards HER and is a hot topic in the recent years <sup>[4,20,21]</sup>. However, many functions of MoS<sub>2</sub> have been limited by its low electrical conductivity and insufficient number of active sites <sup>[20]</sup>. To circumvent these problems, MoS<sub>2</sub> was hybridized with carbon materials such as active carbon, carbon paper, reduced graphene oxide (GO) and carbon nanotubes (CNTs). Specifically, reduced graphene oxide with a high surface area can serve as a matrix material for catalytically active MoS<sub>2</sub> nanoparticles and enhance the electrocatalytic HER efficiency <sup>[22-25]</sup>. Furthermore, MoS<sub>2</sub> is hybridized with multiwall CNTs to increase its electrical conductivity and the prepared catalysts presented good performance towards HER. <sup>[20]</sup> To enhance the electrocatalytic HER performance of a catalyst, it is important to increase either the surface area of the catalyst loading or making a binder free film and 3D electrode structure <sup>[26,27]</sup>. This can be achieved by making a hybrid composite of



GO and MWCNTs, which leads to the formation of the catalyst with high surface area and 3D nanostructure.

GO has been used extensively due to its excellent physical and chemical properties [28,29]. The existence of functional groups on GO makes them easy to composite with other nanomaterials such as nanoparticles, conducting polymers and carbon nanotubes. It may be regarded as an amphiphilic molecule, since it possesses not only a six-membered aliphatic ring on its planar sides and edges, but also sp<sup>2</sup>-bonded aromatic carbon regions [30,31]. The oxygen containing functional groups makes GO hydrophilic and dissolvable in water, while the aromatic regions offer active sites to make it possible to interact with other aromatic molecules through  $\pi$ - $\pi$  supramolecular interactions [32,33]. As a result, GO is very suitable to suspend CNTs in water and this leads to the development of a new strategy for making GO-CNT composites.

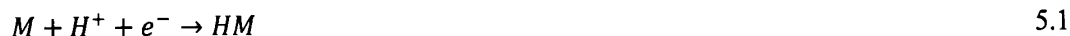
This chapter describes a facile method for the synthesis of a high-performance ternary MoS<sub>2</sub>/GO-CNT composite catalyst through a wet-chemical strategy by depositing MoS<sub>2</sub> onto a reduced graphene oxide-multi-walled carbon nanotube support. The author characterizes the resultant samples using field emission scanning electron microscopy (FESEM), transmission electron microscopy (TEM), micro-Raman spectroscopy, X-ray photo electron spectroscopy and X-ray diffraction (XRD) in order to prove the high quality nature of the as obtained composite and to determine the reaction mechanisms. Up till now, Peng *et al.*, has made a composite of CoS<sub>2</sub>/GO-CNT with excellent electrocatalytic performance towards HER and our group is the first to make a composite of MoS<sub>2</sub>/GO-CNT for HER [34]. The synthesis technique in our work is based on a hydrothermal process by mixing aqueous dispersion of GO and CNT to make a 3D hybrid GO-CNT composite. Then, MoS<sub>2</sub> was grown on the surfaces of GO-CNT substrate hydrothermally which leads to the formation of 3D hybrid MoS<sub>2</sub>/GO-CNT composite. The ideal combination of MoS<sub>2</sub> and the 3D GO-CNT composite provide the resultant robust MoS<sub>2</sub>/GO-CNT hybrid with integrated properties, such as large specific surface area, high electrical conductivity, good stability and durability. Therefore, the as-prepared hybrid MoS<sub>2</sub>/GO-CNT composite exhibited excellent performance towards the electrochemical hydrogen evolution (HER) with low overpotential and high current densities.

## 5.2 Hydrogen Evolution Reaction

A hydrogen evolution reaction is the production of hydrogen through the process of water electrolysis. The hydrogen evolution reaction (HER) is intensively explored by

experimental as well as theoretical research groups due to its simplest reaction mechanism. In order to better understand the kinetics of cathodic HER, it is essential to determine the mechanism of the reaction. This is usually done by characterizing the adsorption performance and surface coverage of kinetically adsorbed intermediates such as hydrogen during hydrogen evolution. The fundamental steps involved in the HER reaction is as follows.

Discharge reaction of a proton to form an adsorbed hydrogen atom, known as Volmer reaction<sup>[35]</sup>



- Combination of an adsorbed hydrogen atom with a proton and an electron to form molecular hydrogen, known as Heyrovsky reaction<sup>[36]</sup>



- Combination of two adsorbed hydrogen atoms to form molecular hydrogen, known as Tafel reaction<sup>[37]</sup>



The overall reaction will be



This reaction can occur in two different reaction pathways, the Tafel-Volmer<sup>[35,37]</sup> and the Heyrovsky-Volmer<sup>[35,36]</sup> pathway. Molecular hydrogen is formed by the recombination of two adsorbed hydrogen atoms in the Tafel-Volmer reaction. The Heyrovsky-Volmer reaction describes the formation of molecular hydrogen from one adsorbed hydrogen atom and one proton from the electrolyte which is discharged at the adsorbed hydrogen atom on the surface. Therefore the adsorption of atomic hydrogen is the important issue.

A common and most fundamental representation of the polarization of an electrode supporting one specific reaction is given in the Butler-Volmer equation:

$$i_{reaction} = i_0 \left\{ \exp\left(-\beta \frac{nF}{RT} \eta_{reaction}\right) - \exp\left((1 - \beta) \frac{nF}{RT} \eta_{reaction}\right) \right\} \quad 5.5$$

where  $i_{reaction}$  is the anodic or cathodic current,  $i_0$  is the exchange current,  $\beta$  is the charge transfer barrier coefficient for the anodic or cathodic reaction, usually close to 0.5,  $n$  is the number of contributing electrons,  $R$  is the gas constant ( $8.314 \text{ J mol}^{-1} \text{ K}^{-1}$ ),  $T$  is the absolute temperature (K) and  $F$  corresponds to  $96485 \text{ C/mole of electrons}$ .

When  $\eta_{reaction}$  is cathodic, i.e. -ive, the second term in the Butler-Volmer equation turn out to be negligible and the cathodic current density ( $i_c$ ) can be stated by a simpler equation and its logarithm on both sides.

$$i_{reaction} = i_c = i_0 \exp\left(-\frac{\beta nF}{RT} \eta_{reaction}\right) \quad 5.6$$

$$\eta_{reaction} = \eta_c = b_c \log_{10} \left(\frac{i_c}{i_0}\right) \quad 5.7$$

where  $b_c$  is the cathodic Tafel coefficient pronounced in the equation that can be attained from the slope of a plot of  $\eta$  against  $\log |i|$ , with the intercept yielding a value for  $i_0$ .

$$b_c = -2.303 \frac{RT}{\beta n F} \quad 5.8$$

In the same way, when  $\eta_{\text{reaction}}$  is anodic, then

$$b_a = 2.303 \frac{RT}{\beta n F} \quad 5.9$$

The electrocatalytic activity can be described by the exchange current density  $j_0$ , which is reliant on the electrode material and the concentration of educts and products. A classical representation is the plot of  $\log j_0$  versus the adsorption energy  $\Delta G_{\text{ad}}$  of the hydrogen to the metal resulting in the so called Volcano plot [38]. Both branches of the plot end in a vertex where  $\Delta G_{\text{ad}} \approx 0$  [39]. Typically, noble metal catalysts such as Pd, Pt, etc. or alloys of these metals are situated near the top of the volcano (Figure 5.1). They display a neither too strong nor too weak interaction of the respective metal with hydrogen ( $\Delta G_{\text{ad}} \approx 0$ ).

A suitable value to compare the activity of the different systems is the exchange current density  $j_0$  which describes the electrocatalytic activity of the surface and is dependent on the surface structure as well as the concentration of educts and products. Conway and Bockris [40] reported a correlation of the exchange current density  $j_0$  to the electronic work function  $\phi$ , which defines the binding energy between electrons near the Fermi level and the material. For HER, it was also shown that the logarithm of  $j_0$  increases as the d character of the material increases. The latter was explained by the fact that as the d character increases, more electrons have paired spins and hence they require more energy to extract them resulting in a decrease of  $\Delta H$  of adsorbed hydrogen atoms.

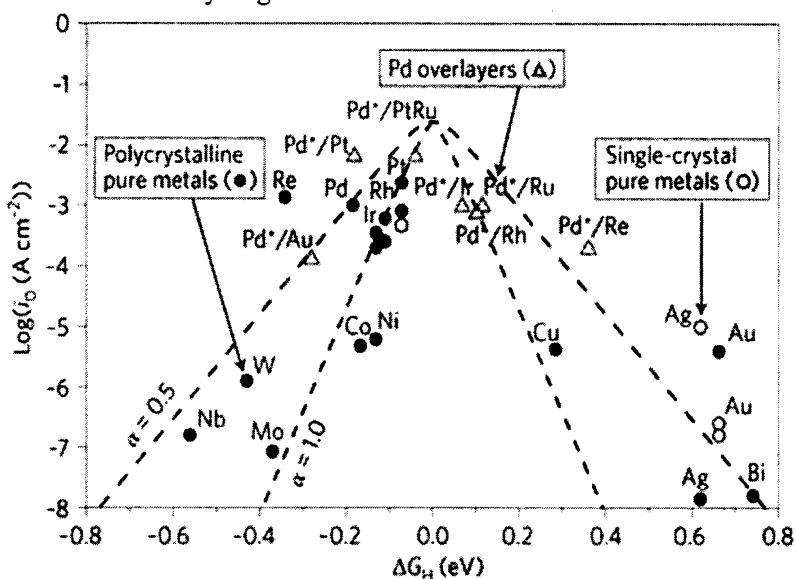


Figure 5.1 Volcano plot for various pure metals and metal overlayers [41].

Parsons<sup>[39]</sup> studied the relationship between exchange current density and the ability of the electrode to adsorb atomic hydrogen in terms of the standard free energy  $\Delta G_H$ . His theoretical studies showed that  $\log j_0$  reaches a maximum when  $\Delta G_H \approx 0$ . Metals such as Pt, Pd, Rh, and Ir that adsorb moderately hydrogen have high values of  $j_0$ .

Trasatti<sup>[38]</sup> achieved two properly parallel lines for the exchange current density  $j_0$  being plotted versus the work function. The rate and mechanism of HER depends on the bond strength between metal and hydrogen atom (M-H). A pass through a maximum is suggested and a similar volcano shape curve was reported by Krishtalik and Delahay<sup>[42]</sup>. Pt is close to the top of the volcano curve where the Pt-H bond is neither too strong nor too weak.

Layered materials have been broadly used in catalysis in their pure forms as well as doped and composite forms. MoS<sub>2</sub> nanostructures have been normally used as catalysts in catalytic reactions such as hydrodesulphurization and more lately for hydrogen evolution reactions. The catalytic activity is generally attributed to the unsaturated sites at the particle edge surfaces, parallel to the hexagonal axis of lamellar MoS<sub>2</sub> structures. For HER, a systematic investigation of surface sites on MoS<sub>2</sub> nanoparticles of Au (111) have revealed that hydrogen evolution correlates linearly with the number of edge site on the MoS<sub>2</sub> catalyst.<sup>[43]</sup> Hence, the key factors for optimization of the HER activity in MoS<sub>2</sub> are increasing the catalytic activity of the active sites, enhancing the number of active sites (MoS<sub>2</sub> layer edges, therefore the applications of structures such as nanoribbons are advised) and increasing the electrical contact to the active sites (which is provided by the planar routes for electrons within the 2D structure). The integration of layered MoS<sub>2</sub> with the morphologically compatible graphene has also shown promise in increasing the catalytic activity. The addition of graphene to MoS<sub>2</sub> increases the electronic conductivity of the electrode, thereby improving the overall activity. Li *et al.*, have confirmed that few layered MoS<sub>2</sub> structures synthesized on graphene sheets show improved electrocatalytic activity in HER which has been attributed to the abundance of exposed MoS<sub>2</sub> edges on graphene and their excellent electrical coupling<sup>[4]</sup>.

## 5.3 Experimental Procedure

### 5.3.1 Materials

Natural graphite powder and multi-walled carbon nanotubes (MWCNTs) were purchased from Alfa Aesar; ammonium thiomolybdate ((NH<sub>4</sub>)<sub>2</sub>MoS<sub>4</sub>) (99%) was purchased from Sigma Aldrich; N<sub>2</sub>H<sub>4</sub>·H<sub>2</sub>O and N, N-dimethylformamide (DMF) were purchased from

Sinopharm Chemical Reagent Co. (China). All reagents were of analytical grade and were used as received without further purification.

### 5.3.2 Synthesis of GO

The graphene oxide (GO) was prepared as mentioned in Chapter 3.

### 5.3.3 Synthesis of COOH-Functionalized MWCNTs

In a typical process, 500 mg MWCNTs were refluxed in 60% HNO<sub>3</sub> (50 mL) solution for 24 hours. After cooling to room temperature the MWCNT-COOH mixture was first diluted with 100 mL deionised (DI) water and then vacuum filtered through a 0.45 μm PTFE Millipore membrane and thoroughly washed with DI water until pH become neutral. The filtered solid was then dried under vacuum for 24 hours at 50 °C.

### 5.3.4 Synthesis of GO-CNT Composite

From the above synthesized GO powder 15 mg was dispersed in DI water and ultrasonicated for 30 minutes. Then, 30 mg of acid treated MWCNTs was added to GO aqueous dispersion under sonication for approximately 30 min. The mixture was subsequently sealed in a 50 mL Teflon-lined autoclave and maintained at 200 °C for 24 h. After the mixture was cooled in room-temperature with natural convection, a black precipitate was obtained. The as-obtained precipitate was freeze-dried overnight for use in subsequent experiments.

### 5.3.5 Synthesis of MoS<sub>2</sub>/GO-CNT Composite

In a typical synthesis of MoS<sub>2</sub>/GO-CNT composite, 12 mg of GO-CNT powder were dispersed in 20 mL DMF by ultrasonication for 30 min. Then, 32 mg of (NH<sub>4</sub>)<sub>2</sub>MoS<sub>4</sub> was added to it and ultrasonically dispersed at room temperature for another 30min in the DMF solution until a clear and homogeneous solution is achieved. After that, 0.2 mL of N<sub>2</sub>H<sub>4</sub>·H<sub>2</sub>O was added. The reaction solution was further sonicated for 15min before transferred to a 50 mL Teflon-lined autoclave. It was heated in an oven at 210 °C for 24 h, and was cooled down to room temperature naturally. The black precipitate was collected by centrifugation at 12000 rpm for 10 min, washed with DI water several times until all of the DMF was removed and dried overnight at 50 °C. The synthesis procedure of pristine MoS<sub>2</sub> was similar to that described above, but without adding GO-CNT and replacing the DMF with water. The synthetic mechanism is shown in Figure 5.1.

### 5.3.6 Characterizations

The morphology and microstructure of the samples were characterized by field emission scanning electron microscopy (FESEM), transmission electron microscopy (TEM), X-ray diffraction (XRD), Raman spectroscopy and X-ray photoelectron spectrometry (XPS). The surface morphology of the samples was examined by using FESEM (JEOL, JSM-6700F). The microstructure, morphology and electron diffraction pattern of the products was also studied by transmission electron microscope (HRTEM, JEM-2010). The Compositional analysis and concentration of elements were achieved by energy dispersive X-ray spectroscopy (EDX) attached with FESEM. X-ray diffraction (XRD) was carried out on a Rigaku powder X-ray diffractometer. X-ray photoelectron spectroscopy (XPS) spectrum was collected using SPECS system (PHOIBOS 150, Germany) with Al K $\alpha$  radiation ( $h\nu = 1486.6$  eV). Raman spectrum of powder samples were recorded on using LabRAM HR Raman microscope having Nd-YAG laser with a 532 nm excitation source.

### 5.3.7 Electrochemical Measurements

Before each electrochemical experiment, a glassy carbon (GC) electrode (0.196 cm<sup>2</sup> geometric surface area) was first polished with alumina slurries (Al<sub>2</sub>O<sub>3</sub>, 0.05  $\mu$ m) on a polishing cloth to obtain a mirror finish, followed by sonication in 0.1 M HNO<sub>3</sub>, 0.1 M H<sub>2</sub>SO<sub>4</sub>, and pure water for 10 min, successively. Then the catalyst in pure water was drop-coated on the polished electrode surface by a microliter syringe, followed by drying in vacuum at room temperature. Afterward, the catalyst was covered with a thin layer of Nafion (0.1 wt % in water, 5  $\mu$ L) to ensure that the catalyst was tightly attached to the electrode surface during the electrochemical measurements. Voltammetry measurements were carried out with a CHI750D electrochemical workstation. To measure the HER activity, 0.1M HClO<sub>4</sub> solution was bubbled for 30 minutes with N<sub>2</sub> gas. Then, the catalyst loaded with GC electrode was immersed and rotated with 1000 rpm using rotating disk electrode work station at 5 mV/s scan rate by linear sweep voltametric (LSV) method with continuous purging of N<sub>2</sub> gas. Durability test for HER was also carried out with similar conditions as above for HER in 0.1M HClO<sub>4</sub> solution at a scan rate of 10 mV/s scan rate with 1000 rpm rotation speed up to 1000 cycles.

## 5.4 Results and Discussion

### 5.4.1 Morphology and Mechanism

The strategy for the synthesis of ternary hybrid MoS<sub>2</sub>/GO-CNT composite is illustrated in Figure 5.2. For this purpose, we initially prepare GO via the Hummer's method which contains a large number of oxygenated functional groups that allow GO to be well-dispersed in water. In addition, we also prepare MWCNTs and they were functionalized with COOH. FESEM analysis was performed on GO and MWCNTs and the results are reported in Figure 5.3. A representative sheet structure of GO is shown in Figure 5.3a. The reduced graphene oxide demonstrates typical wrinkled structure that produced sheet folding. As shown in Figure 5.3b, the nanotubes have a long, tubular topology with smooth surface and they are held together into bundles.

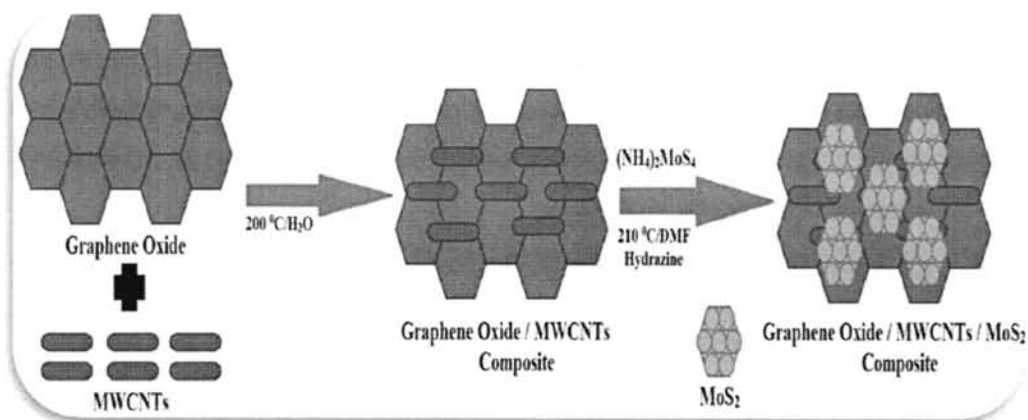


**Figure 5.2** FESEM images of (a) GO and (b) COOH-functionalized MWCNTs.

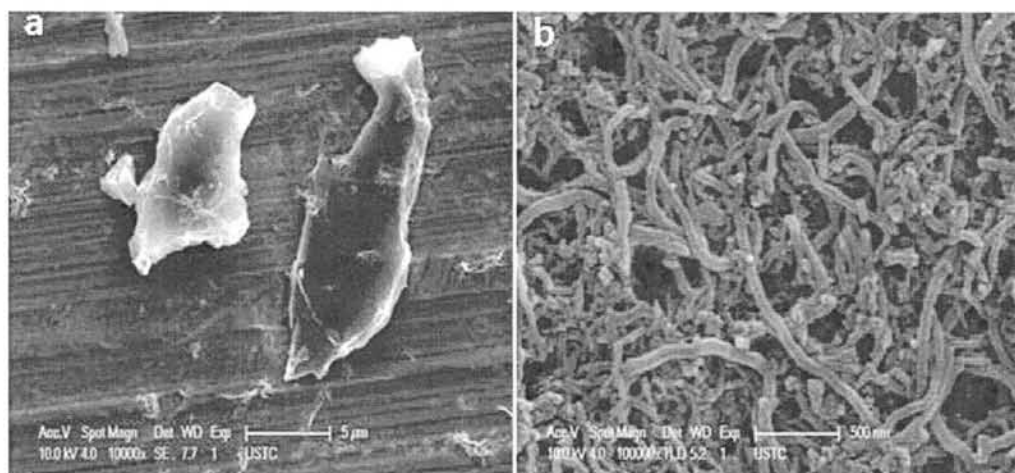


**Figure 5.3** Schematic illustration of the synthesis of MoS<sub>2</sub>/GO-CNT composite.

The amphiphilic nature of GO sheets can serve as surfactant; CNTs can be dispersed into individual ones after ultrasonication and adsorbed onto the GO surface. This results in the adsorption of CNTs onto the surface of GO through  $\pi$ - $\pi$  attractions<sup>[32]</sup>. Further treatment of the GO and CNT aqueous dispersion hydrothermally leads to the formation of reduced GO-CNT composite via weak interactions, such as  $\pi$ - $\pi$  stacking, van-der Waals forces, hydrogen bonding and additional interactions<sup>[44]</sup>. The as-prepared GO-CNT composite has well-defined and interconnected 3D porous microstructure, and the CNTs are randomly distributed inside the graphene sheets (Figure 5.4). The ternary MoS<sub>2</sub>/GO-CNT composite was obtained by the in-situ growth of MoS<sub>2</sub> onto the surfaces of GO-CNT composite through a simple hydrothermal process. In this method, the use of reduced GO together with MWCNTs not only increases the specific contact area, which enables the transport of the ions and electrons, but also offers more exposed active sites for the anchoring of MoS<sub>2</sub> precursors and further MoS<sub>2</sub> nucleation<sup>[4,34,45]</sup>. The growth of MoS<sub>2</sub> on GO-CNT composite can improve the effective interaction between the active materials and the liquid electrolyte, which in result gives excellent electrocatalytic HER properties. In other words, it maintains a good connection between the catalyst and a carbon electrode, and a strong electrical connection within the entire electrode structure.

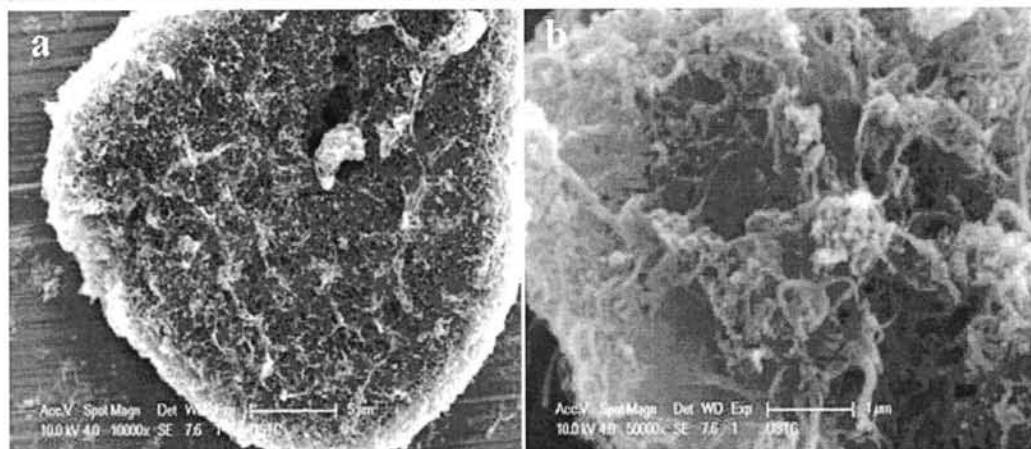


**Figure 5.4** (a) Low and (b) high magnification FESEM images of GO-CNT composite.

The morphology of the MoS<sub>2</sub>/GO-CNT composite samples and pristine MoS<sub>2</sub> were observed using FESEM and TEM, and the results are shown in Figure 1. Figure 1a shows FESEM image of the pristine MoS<sub>2</sub> with a spherical morphology mainly consisted of 2D sheet-like petals in random orientations. Figure 5.5b, 5.5c and 5.5d show FESEM images of MoS<sub>2</sub>/GO-CNT composite. It reveals that GO-CNTs surfaces have been uniformly decorated with MoS<sub>2</sub> nanoparticles. These hybrid nanocomposites have a clear and interconnected three



dimensional porous network. The partial coalescing or overlapping of graphene sheets results in the formation of cross-linking sites of the framework of hybrid, and the pore sizes of the network are in the range of several submicrometer to micrometers. The high magnification SEM image in Figure 5.5d revealed that most of the CNTs and GO sheets are well-decorated with MoS<sub>2</sub> nanoparticles.

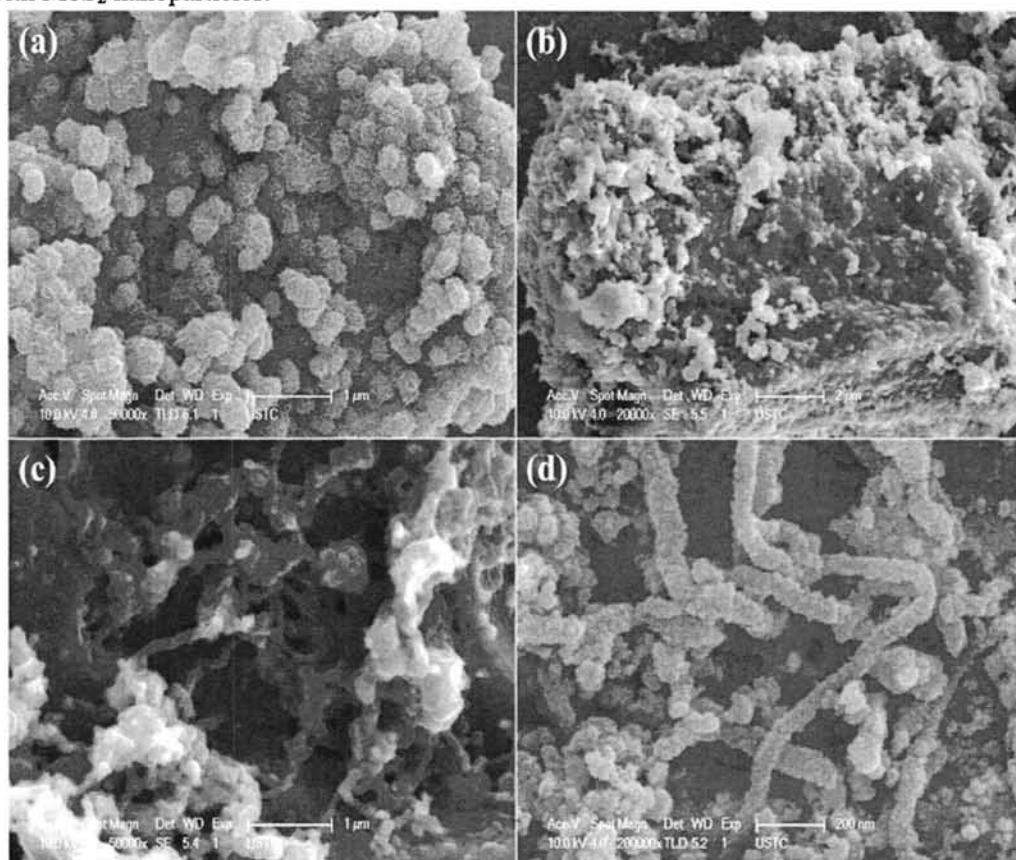


**Figure 5.5** FESEM images of (a) pristine MoS<sub>2</sub> and MoS<sub>2</sub>/GO-CNT composite. (b) Low, (c) and (d) high magnification images of MoS<sub>2</sub>/GO-CNT composite.

TEM has further been employed to characterize the nanostructure of MoS<sub>2</sub>/GO-CNT hybrid. Figure 5.6a and b display that MoS<sub>2</sub>, GO and MWCNTs are randomly oriented having a disordered structure. The creation of MoS<sub>2</sub> sheets on GO-CNT surface is greatly bothered by the oxygenated and carboxyl functional groups in GO and MWCNTs. In the development of the hydrothermal process, MoS<sub>2</sub> may grow via precursors on these highly active sites to form seeds on the CNT and GO surfaces<sup>[46]</sup>. Therefore, the creation of the MoS<sub>2</sub>/GO-CNT composite structure went through many nucleation and growth processes on the relevant sites of GO and MWCNTs and thus, creating an assembly of MoS<sub>2</sub> on GO-CNT matrix with randomly oriented and disordered 3D structure. In order to further investigate the

structural information of MoS<sub>2</sub>/GO-CNT, HRTEM were carried out, as presented in Figure 5.6c. It can be clearly seen that the samples is made up of a few-layered MoS<sub>2</sub> nanosheets. The interlayer distance measured from HRTEM image is 0.62 nm, which can be assigned to the (002) plane of MoS<sub>2</sub>. This result coincides well with the results of XRD.

The elemental composition of the GO-CNT and MoS<sub>2</sub>/GO-CNT composites were carried out using energy dispersive X-ray spectroscopy (EDS) integrated with FESEM instrument, as expected in Figure 5.7. From the EDS measurements, it can be seen that molybdenum, sulfur and carbon are present in the hybrid composite. It is also noted that the concentration of carbon is decreased while the concentration of oxygen is increased in the ternary composite as compare to GO-CNT composite.

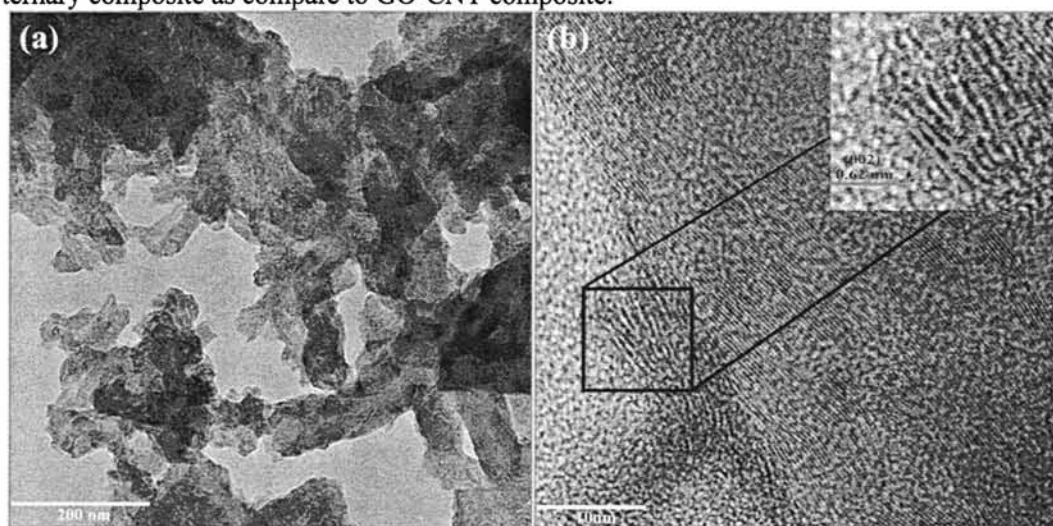


Figure 5.6 (a) TEM and (b) HRTEM images of MoS<sub>2</sub>/GO-CNT composite.

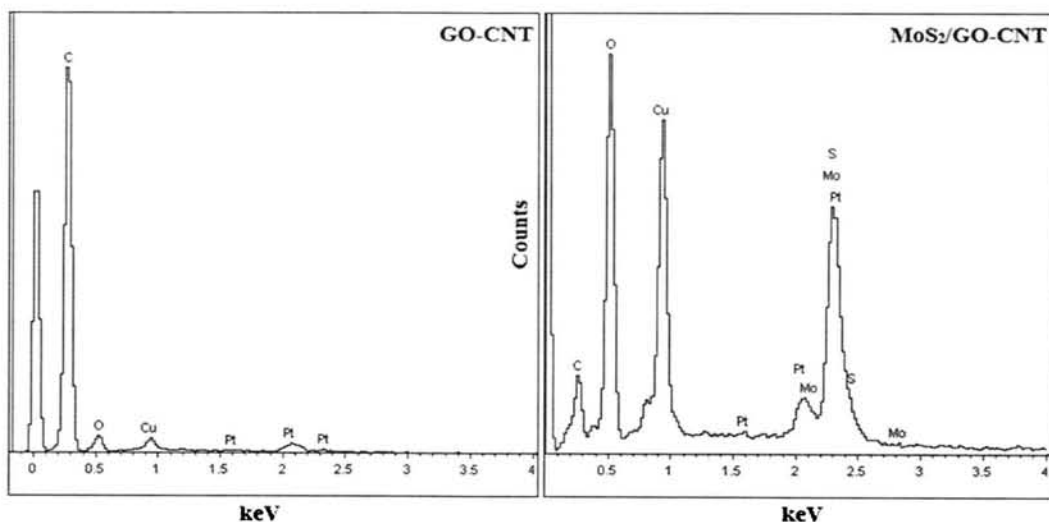


Figure 5.7 EDS spectra of GO-CNT and MoS<sub>2</sub>/GO-CNT composites.

### 5.4.2 Structural Characterization

The structural and crystalline phases of the MoS<sub>2</sub>/GO-CNT composite and pristine MoS<sub>2</sub> are characterized by X-ray diffraction (XRD), which is shown in Figure 5.8. The diffraction peaks observed at  $2\theta = 14.2^\circ$ ,  $33.2^\circ$  and  $59.0^\circ$ , which correspond to (002), (100) and (110) planes of MoS<sub>2</sub>. The diffraction peaks are consistent with an orthorhombic phase of MoS<sub>2</sub> (JCPDS no. 37-1492). The strong and more broadened diffraction (002) peak around  $14.2^\circ$  with 0.62 nm spacing indicates the natural layered structure of MoS<sub>2</sub> along the c-axis. All the peak positions of the MoS<sub>2</sub>/GO-CNT composite are found to be slightly shifted to lower diffraction angles and also the intensity of the peaks become more weaker compared with that of pristine MoS<sub>2</sub>, representing that the incorporation of GO-CNT can further suppress the stacked natural layers of MoS<sub>2</sub>. Additionally, the more intense peak observed in the XRD spectra of MoS<sub>2</sub>/GO-CNT at  $2\theta = 26.1^\circ$  corresponds to the (002) plane of graphene [47].

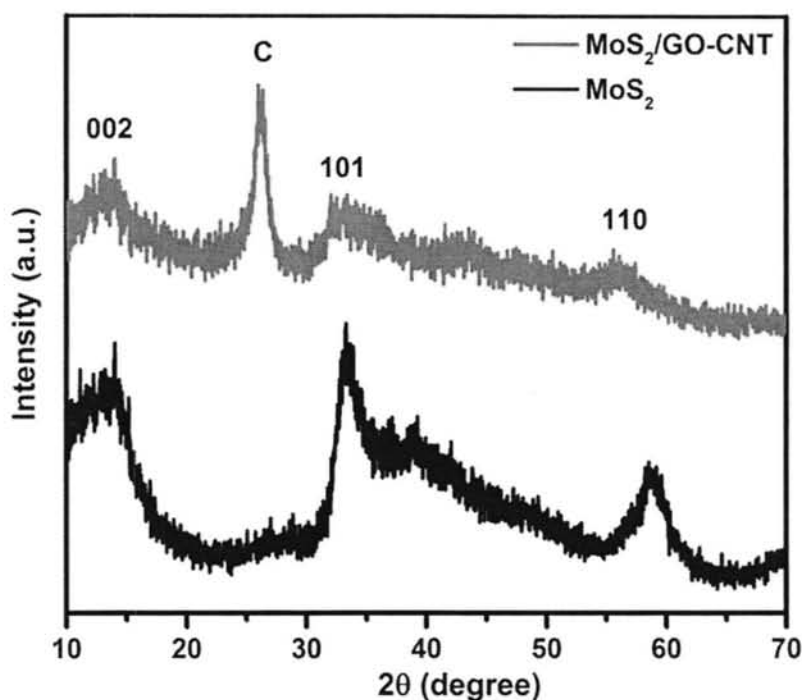
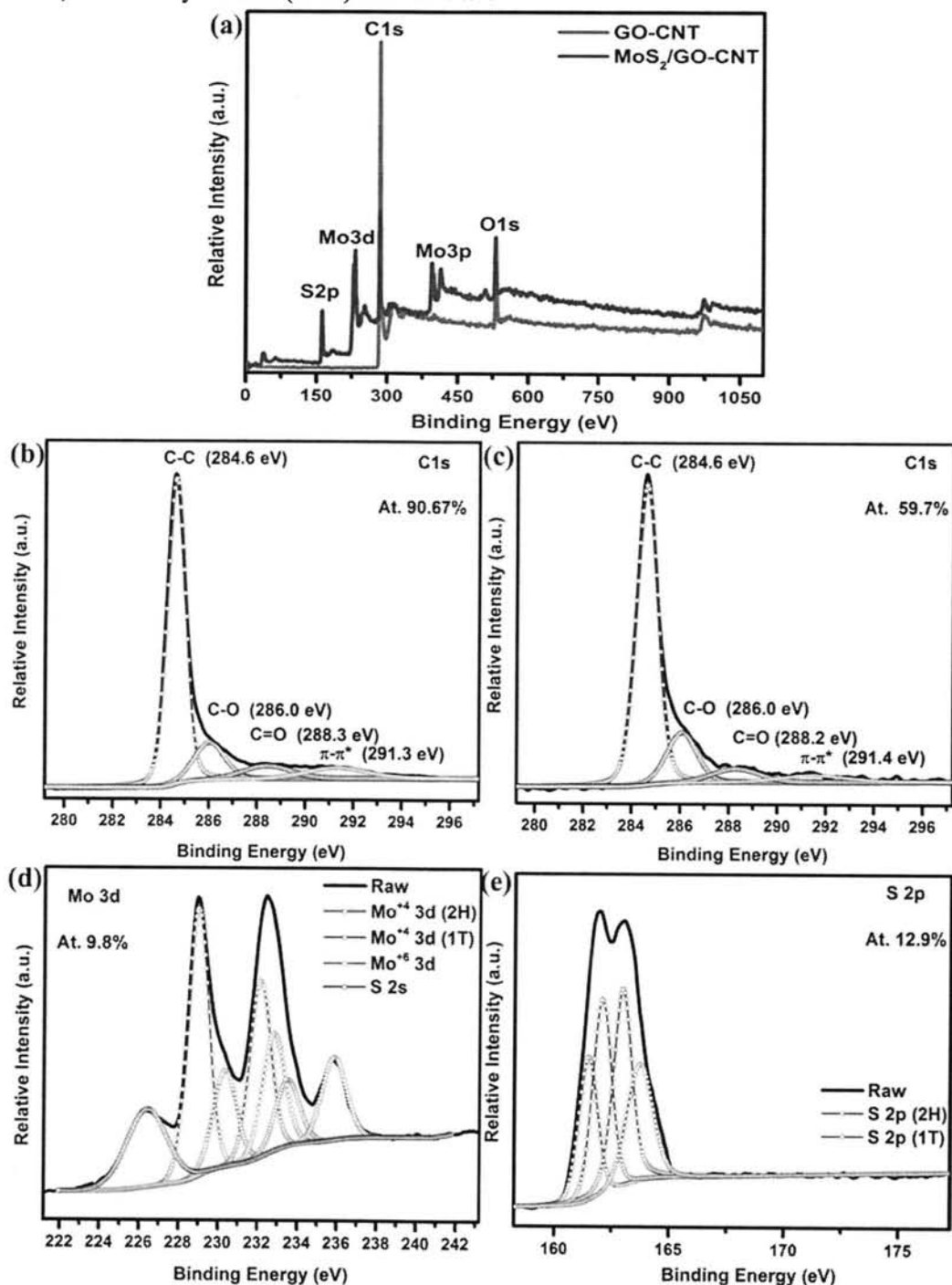


Figure 5.8 XRD spectra of pristine MoS<sub>2</sub> and MoS<sub>2</sub>/GO-CNT composite.

XPS was employed to determine the chemical state, type, and extent of the surfaces of the MoS<sub>2</sub>/GO-CNT and GO-CNT composites (Figure 5.9). As shown in Figure 5.9a, the XPS survey-spectrum indicates only molybdenum, sulfur, oxygen, and carbon elements. The C1s XPS results shown in Figure 5.9b reveal the formation of various surface groups on the obtained composite. The peaks of C1s spectra are assigned to three components that

correspond to carbon atoms in the respective functional groups: the C-C bonds, the C-O bonds, the carbonyl carbon (C=O) and the  $\pi$ - $\pi^*$ .<sup>[48,49]</sup>



**Figure 5.9** (a) X-ray photoemission spectroscopy (XPS) profiles of GO-CNT and MoS<sub>2</sub>/GO-CNT hybrid samples. (b) Curve fit of the C1s peak of GO-CNT. (c) Curve fit of the C1s peak of MoS<sub>2</sub>/GO-CNT. (d) Curve fit of Mo3d peak of MoS<sub>2</sub>/GO-CNT. (e) Curve fit of S2p peak of MoS<sub>2</sub>/GO-CNT.

The peak intensity associated with C-C bonds indicates that the sp<sup>2</sup>-hybridized graphitic structure is predominant in both the composites, while the peak composed of oxygenated functional groups was substantially reduced (Figure 5.9b-c) after the hydrothermal process. Moreover, after the formation of MoS<sub>2</sub> onto the surfaces of GO-CNT, the peak intensity of oxygenated functional groups slightly increased, and peaks corresponding to the binding energies of Mo3d and S2p appeared. The deconvolution of Mo3d spectra in Figure 5.9d reveals the two doublets 3d5/2 and 3d3/2 at 229 eV and 232.1 eV, respectively, representing the 2H phase of MoS<sub>2</sub>, while the peaks observed at 230.3 eV and 233.5 eV, respectively, representing the two doublets (3d5/2 and 3d3/2) of 1T phase of MoS<sub>2</sub> [50]. The peak positions of 1T phase of MoS<sub>2</sub> are lower shifted compared to 2H phase of MoS<sub>2</sub>.

In addition, some more peaks were observed at 232.8 eV and 235.9 eV, respectively, indicating the presence of the oxide phase of Mo (MoO<sub>3</sub>) [51]. The S2p band in Figure 5.9e exhibits a main peak comprised of two Sp1/2 and Sp3/2 doublets. The first doublet, with peaks located at 161.5 and 162.9 eV are attributed to the 2H phase of MoS<sub>2</sub>. The second couple, with peaks located at 162 and 163.8 eV is attributed to the 1T phase of MoS<sub>2</sub> [20]. From the intensity and area of Mo3d and S2p spectra, it is obviously understood that 2H is the dominant phase in MoS<sub>2</sub>/GO-CNT composite [52]. In conclusion of the XPS results, it is a significant fact that there appears an interaction between MoS<sub>2</sub> and GO-CNT in the composite, which is derived from the electron transfer between closely contacted MoS<sub>2</sub> and GO-CNT surfaces, thus the interaction of electrons between MoS<sub>2</sub> and GO-CNT can efficiently increase the conductivity of the ternary hybrid.

Raman spectroscopy was used to investigate the structural features of the formation of MoS<sub>2</sub>/GO-CNT composite. Figure 5.10 shows the Raman scattering of the composite sample compared with that of the pure MoS<sub>2</sub>. In the range from 350 to 450 cm<sup>-1</sup>, the spectra of pure MoS<sub>2</sub> and MoS<sub>2</sub>/GO-CNT composite have the identical peaks. The two dominant peaks of pure MoS<sub>2</sub> at 378 and 405 cm<sup>-1</sup> correspond to the E<sub>2g</sub><sup>1</sup> and A<sub>1g</sub> modes of the hexagonal MoS<sub>2</sub> crystal, respectively. The E<sub>2g</sub><sup>1</sup> mode involves the in-layer displacement of Mo and S atoms, whereas the A<sub>1g</sub> mode involves the out-of-layer symmetric displacements of S atoms along the c-axis [53]. The Raman spectra of MoS<sub>2</sub>/GO-CNT composite compared to the pure MoS<sub>2</sub> show in-plane E<sub>2g</sub><sup>1</sup> mode and out-of-plane A<sub>1g</sub> mode at about 381 and 407 cm<sup>-1</sup>, respectively. This result indicates a red-shift of 3 and 2 cm<sup>-1</sup>, which agrees with a classical model of coupled harmonic oscillators predicting softening of the vibrations with an increase in the number of layers. [54] Moreover, the full width of half-maxima (FWHM) of the first-order Raman modes is a good estimation for finding the effective size of the nanoparticles. The

FWHM of E<sub>2g</sub><sup>1</sup> and A<sub>1g</sub> modes were increased from 5 and 6 cm<sup>-1</sup> for pristine MoS<sub>2</sub> to 13 and 12 cm<sup>-1</sup> for MoS<sub>2</sub>/GO-CNT composite. In addition to the E<sub>2g</sub><sup>1</sup> and A<sub>1g</sub> modes, an asymmetric peak and Raman-inactive A<sub>2u</sub> mode has arisen at 452 cm<sup>-1</sup>, which is activated by the strong resonance effect and is considered as a superposition of a second-order process involving the longitudinal acoustic phonon scattering. This peak is otherwise considered to be associated with the oxidized state of Mo [55].

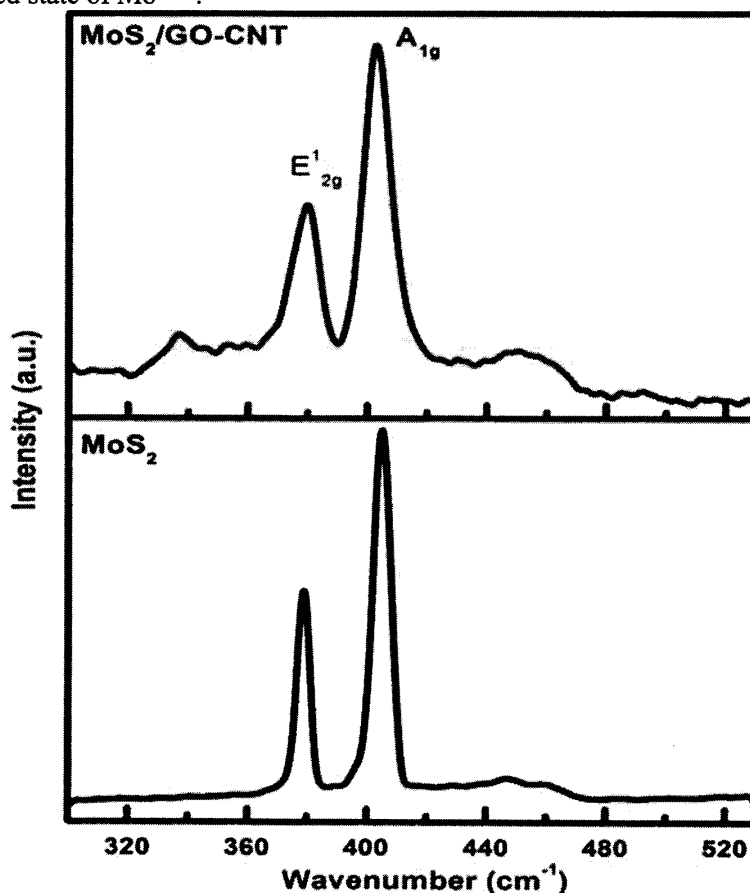


**Figure 5.10** Raman spectra of the E<sub>2g</sub><sup>1</sup> and A<sub>1g</sub> vibrational modes for pristine MoS<sub>2</sub> and MoS<sub>2</sub>/GO-CNT composite.

To detect the ordered and disordered crystalline structure of graphene, we have also measured the Raman spectra of all the samples in the region from 1100 to 1800 cm<sup>-1</sup>. Figure 5.11 shows the Raman spectra of reduced GO, COOH-functionalized MWCNTs, GO-CNT and MoS<sub>2</sub>/GO-CNT composite. In all four samples, two main peaks were detected and can be assigned to the D (E<sub>2g</sub>) and G (A<sub>1g</sub>) band, respectively. In general, the D band is ascribed to defects and disorder in the hexagonal graphitic layers, while the G band is ascribed to the vibration of sp<sup>2</sup> carbon atoms in a 2D hexagonal lattice. Therefore, the ratio of intensities of

D and G bands ( $I_D/I_G$ ) is an indication of the graphene quality [56]. The  $I_D/I_G$  ratio of reduced GO, COOH-functionalized MWCNTs, GO-CNT and MoS<sub>2</sub>/GO-CNT composite calculated are 1.15, 1.18, 1.20 and 1.25. This increase in the  $I_D/I_G$  ratio strongly suggests the formation of GO-CNT composite and MoS<sub>2</sub> layers formation on the surfaces of the GO and CNT, which promotes to increase the disorderness of GO and CNT in the composite and results in an overall increase in the  $I_D/I_G$  ratio. The FWHM of D and G band was found to enhance up and blue-shifted by the formation of MoS<sub>2</sub>/GO-CNT composite as compared to GO-CNT composite. This enhancement also indicates the increase in disorderness due to the formation of MoS<sub>2</sub> on the surfaces of GO and CNT. Therefore, the high  $I_D/I_G$  ratio and blue-shifting of the Raman bands in the composite spectrum could be assigned to the formation of covalent bonding between MoS<sub>2</sub> and GO-CNT composite.

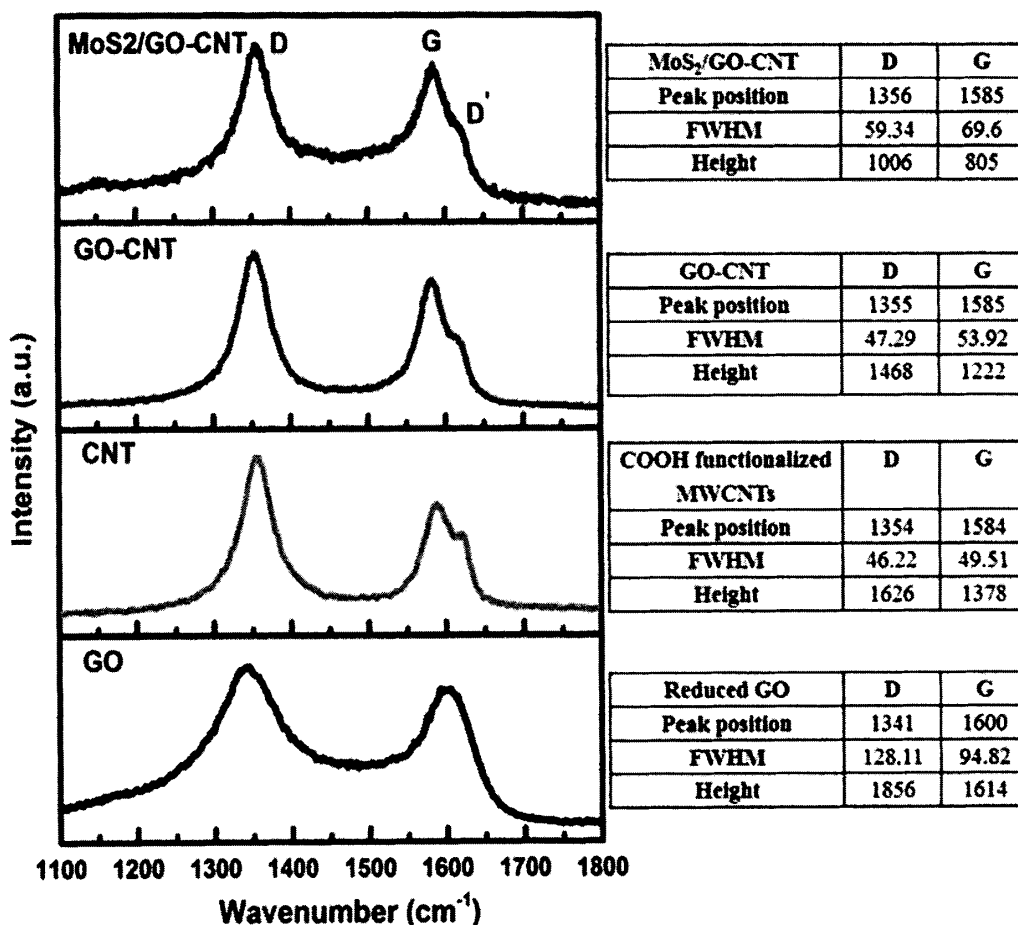
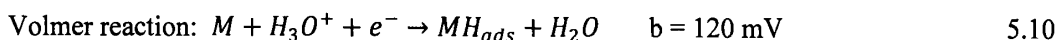


Figure 5.11 The D and G bands of the Raman vibrational modes of reduced-GO, COOH-functionalized MWCNTs, GO-CNT and MoS<sub>2</sub>/GO-CNT composite. Their corresponding peak positions, FWHM and height of D and G respectively, are also visible in the table.

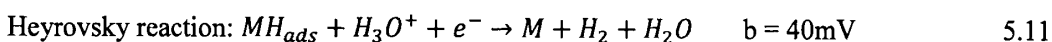
## 5.5 Electrochemical Performance

The electrocatalytic Hydrogen evolution reaction activities of MoS<sub>2</sub>/GO-CNT composite deposited on a glassy carbon electrode in 0.1 M HClO<sub>4</sub> solution using a typical three electrode setup. Figure 5.12 shows the polarization curves of the samples measured in a 0.1 M HClO<sub>4</sub> solution with a scan rate of 5 mVs<sup>-1</sup> at room temperature. For comparison, the HER activities of a commercial Pt catalyst and bulk MoS<sub>2</sub> were also measured. As expected, the commercial Pt catalyst shows higher HER activity with almost near zero overpotential. On the other hand, the polarization curve measured for MoS<sub>2</sub>/GO-CNT composite showed an onset potential of 35 mV versus a reversible hydrogen electrode (RHE), beyond which the cathodic current rose rapidly under a more negative potential (Figure 5.12a). Moreover, pristine MoS<sub>2</sub> showed an onset potential of 210 mV, which reflects much lower HER activity compared with the composite. A Tafel plot was drawn to investigate further the electrochemical properties of the material by fitting the linear portions of the Tafel plots to the Tafel equation ( $\eta = b \log j + a$ , where  $\eta$  is the overpotential,  $j$  is the current density,  $b$  is the Tafel slope). Tafel plots represented in Figure 5.12b show a small Tafel slope of ~38 mV per decade for MoS<sub>2</sub>/GO-CNT composite, much lower than ~104 mV per decade for pristine MoS<sub>2</sub> and slightly higher than 30 mV per decade for the Pt/C catalyst. By extrapolating the Tafel plot, the exchange current density of MoS<sub>2</sub>/GO-CNT composite can be calculated as  $2.02 \times 10^{-4}$  mA cm<sup>-2</sup>. The Tafel slope of MoS<sub>2</sub>/GO-CNT composite follows the mechanism of Volmer-Heyrovsky, represented as equation (1) and (2), and the rate determining step is the electrochemical desorption of hydrogen (H<sub>ads</sub>). The possible HER mechanism in high alkaline media comprised of the following three steps [57].

The first step is the electro reduction of water molecules with hydrogen adsorption;



The first step is followed either by the second step, which is the electrochemical desorption of hydrogen (H<sub>ads</sub>)



or the third step, which is the chemical desorption or the recombination of hydrogen (H<sub>ads</sub>)



In the above chemical reactions, H<sub>2</sub> is produced by the combination of either Volmer-Heyrovsky or Volmer-Tafel mechanism. Therefore, calculating the Tafel slope can provide the rate-determining step of HER. The measured Tafel slope in our work is 38 mV per decade, which is approximately near to the value of 40 mV per decade, proposing the Heyrovsky reaction operates.<sup>4</sup> Thus, the desorption step is the rate limiting step, which limits



the kinetics of HER. The mechanism of HER not only depends upon the calculated Tafel slope due to the difference of opinions in the published data, but also depends on the electrical conductivity of the catalysts. The main problem with the use of MoS<sub>2</sub> as a catalyst is the low electrical conductivity between S-Mo-S sheets bonded by van der Waals forces. The electrical conductivity of MoS<sub>2</sub> can be enhanced by modifying its structure either by making a single layer or making a composite with good conductive matrix materials. This result is evidently clear in our work, since the pristine MoS<sub>2</sub> shows an onset potential of 104 mV/dec, while the composite with GO-CNT shows an onset potential of 38 mV/dec. The high electrocatalytic HER activity of MoS<sub>2</sub>/GO-CNT in our work can be attributed to the strong chemical and electronic coupling between MoS<sub>2</sub> and GO-CNT composite with the exposed edges of MoS<sub>2</sub> in the composite materials making it as an active HER catalyst.<sup>[4,58]</sup>

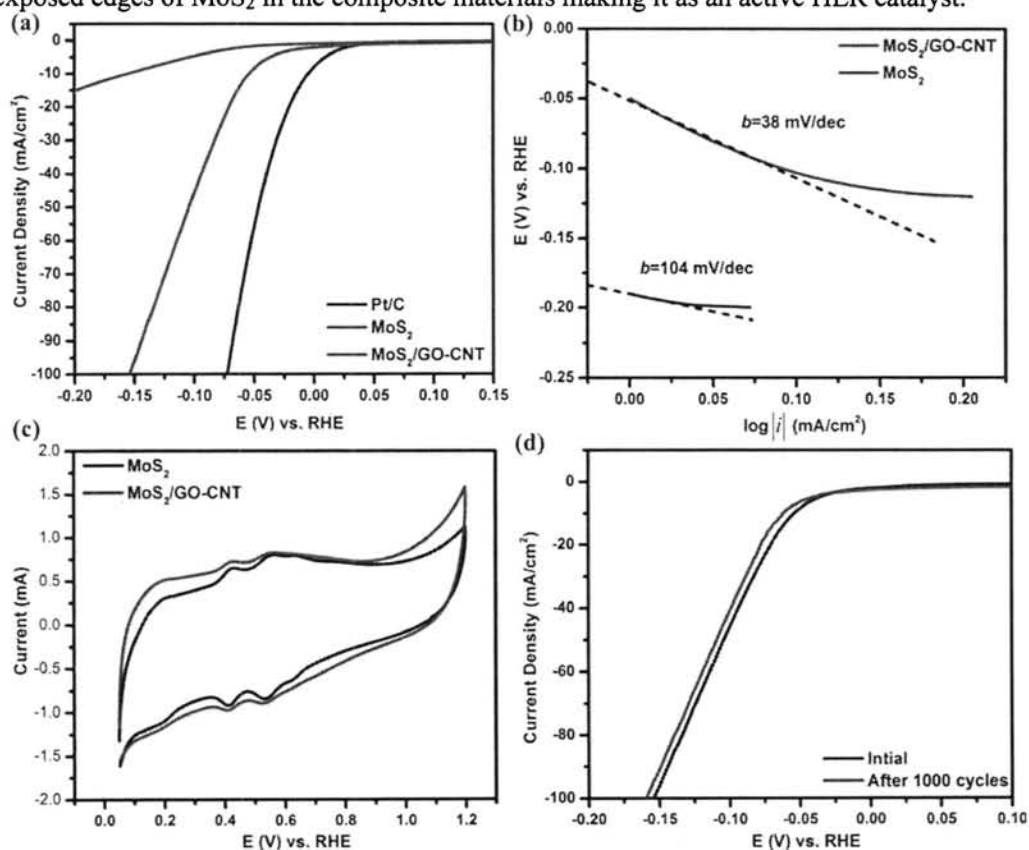


**Figure 5.12** Linear sweep voltammogram measured in a 0.1 M HClO<sub>4</sub> solution at a scan rate of 5 mVs<sup>-1</sup> and (b) corresponding Tafel slope of pristine MoS<sub>2</sub> and MoS<sub>2</sub>/GO-CNT hybrid samples. (c) Representative cyclic voltammograms of pristine MoS<sub>2</sub> and MoS<sub>2</sub>/GO-CNT composite measured in 0.1 M HClO<sub>4</sub> solution at a scan rate of 0.5 mVs<sup>-1</sup> between 0.0 V and 1.2 V. (d) A durability test of the MoS<sub>2</sub>/GO-CNT hybrid catalyst measured in 0.1M HClO<sub>4</sub> solution at a scan rate of 10 mV/s with 1000 rpm rotation speed up to

1000 cycles.

In addition, we have also measured the cyclic voltammograms (CVs) of pristine MoS<sub>2</sub> and MoS<sub>2</sub>/GO-CNT electrodes from 0 to 1.2 V (vs. RHE) measured in 0.1 M HClO<sub>4</sub> solution saturated with N<sub>2</sub> (Figure 5.12c). There were two main oxidation peaks observed during the anodic scan and two reduction peaks during the reversed scan in the CV curves. The first oxidation peak observed at about 0.43 V (vs. RHE) and the second oxidation peak was observed at about 0.56 V during the anodic scan, which was accompanied by the appearance of the two reduction peaks during the reversed scan at about 0.41 V and 0.53 V to the two oxidation peaks respectively. The peaks corresponded to the oxidation state of +4 to +6 in HClO<sub>4</sub> solution and the peaks during the reversed scan corresponded to the reduction state of +6 to +4 phases of Mo<sup>[59]</sup>.

High durability is importance for a good electrocatalyst in the practical application of HER. The stability of the MoS<sub>2</sub>/GO-CNT composite was evaluated by cyclic voltammetry (CV) sweeps between -0.2 and 0.1 V vs. RHE in the 0.5 M HClO<sub>4</sub> solution. The corresponding current density-potential curves of the CV sweeps are shown in Figure 5.12d. After the 1000th cycle, the catalyst still performed as good as the initial cycle. Only a small current degradation was observed in the final measurement.

## 5.6 Summary

In summary, we developed a three-dimensional hierarchical ternary hybrid composite of molybdenum disulfide (MoS<sub>2</sub>), reduced graphene oxide (GO) and carbon nanotubes (CNTs) prepared by a two-step process. Firstly, reduced GO-CNT composite with three-dimensional microstructure is synthesized through  $\pi$ - $\pi$  interactions by hydrothermal treatment of an aqueous dispersion of GO and CNTs and then MoS<sub>2</sub> nanoparticles is hydrothermally grown on the surfaces of GO-CNT composite. Raman analysis confirms the layered structure of MoS<sub>2</sub> and the attachment with GO-CNT composite. XPS data analysis also confirms the existence of 1T and 2H phases with 2H phase dominating in the composite. This ternary composite shows superior electrocatalytic activity and stability in the hydrogen evolution reaction (HER) with a low onset potential of only 35 mV, a Tafel slope of ~38 mV/decade and an apparent exchange current density of  $2.02 \times 10^{-4}$  mA. This excellent electrochemical performance as a catalyst for HER can be attributed to the synergistic effects of 3D nanostructured MoS<sub>2</sub> grown on GO-CNT composite, with the highly exposed edges and excellent coupling between the underlying graphene and high conductive CNTs.

## 5.7 References

1. Bard, A. J.; Fox, M. A. *Acc. Chem. Res.* 1995, 28, 141.
2. Dresselhaus, M. S.; Thomas, I. L. *Nature* 2001, 414, 332.
3. Walter, M. G.; Warren, E. L.; McKone, J. R.; Boettcher, S. W.; Mi, Q.; Santori, E. A.; Lewis, N. S. *Chem. Rev.* 2010, 110, 6446.
4. Li, Y.; Wang, H.; Xie, L. M.; Liang, Y.; Hong, G.; Dai, H. *J. Am. Chem. Soc.* 2011, 133, 7296-7299.
5. Zheng, Y.; Jiao, Y.; Zhu, Y. H.; Li, L. H.; Han, Y.; Chen, Y.; Du, A. J.; Jaroniec, M.; Qiao, S. Z. *Nat. Commun.* 2014, 5, 3783.
6. Hou, Y. D.; Laursen, A. B.; Zhang, J. H.; Zhang, G. G.; Zhu, Y. S.; Wang, X. C.; Dahl, S.; Chorkendorff, I. *Angew. Chem. Int. Ed.* 2013, 52, 3621-3625.
7. Faber, M. S.; Dziedzic, R.; Lukowski, M. A.; Kaiser, N. S.; Ding, Q.; Jin, S. *J. Am. Chem. Soc.* 2014, 136, 10053-10061.
8. Xu, Y. F.; Gao, M. R.; Zheng, Y. R.; Jiang, J.; Yu, S. H. *Angew. Chem. Int. Ed.* 2013, 52, 8546-8550.
9. Chen, W. F.; Muckerman, J. T.; Fujita, E. *Chem. Commun.* 2013, 49, 8896-8909.
10. Popczun, E. J.; Read, C. G.; Roske, C. W.; Lewis, N. S.; Schaak, R. E. *Angew. Chem. Int. Ed.* 2014, 53, 5427-5430.
11. Wang, H.; Lu, Z.; Kong, D.; Sun, J.; Hymel, T. M.; Cui, Y. *ACS Nano* 2014, 8, 4940-4947.
12. Liu, Q.; Tian, J. Q.; Cui, W.; Jiang, P.; Cheng, N. Y.; Asiri, A. M.; Sun, X. P. *Angew. Chem. Int. Ed.* 2014, 53, 6710-6714.
13. Trasatti, S. *Adv. Electrochem. Sci. Eng.* 1992, 2, 1.
14. Varpness, Z.; Peters, J. W.; Young, M.; Douglas, T. *Nano Lett.* 2005, 5, 2306-2309.
15. Fang, B.; Kim, J.; Yu, J. S. *Electrochem. Commun.* 2008, 10, 659-662.
16. Grigoriev, S. A.; Millet, P.; Fateev, V. N. *J. Power Sources* 2008, 177, 281-285.
17. Yan, Y.; Zhang, L.; Qi, X.; Song, H.; Wang, J. Y.; Zhang, H.; Wang, X. *Small* 2012, 8, 3350-3356.
18. McKone, J. R.; Warren, E. L.; Bierman, M. J.; Boettcher, S. W.; Brunschwig, B. S.; Lewis, N. S.; Gray, H. B. *Energy Environ. Sci.* 2011, 4, 3573-3583.
19. Jaramillo, T. F.; Jaramillo, Jørgensen, K. P.; Bonde, J.; Nielsen, J. H.; Horch, S.; Chorkendorff, I. *Science* 2007, 317, 100-102.
20. Laursen, A. B.; Kegnaes, S.; Dahl, S.; Chorkendorff, I. *Energy Environ. Sci.* 2012, 5, 5577-5591.

21. Ge P.; Scanlon, M. D.; Peljo, P.; Bian, X.; Vubrel, H.; O'Neill, A.; Coleman, J. N.; Cantoni, M.; Hu, X.; Kontturi, K. B.; Liu, Girault, H. H. *Chem. Commun.* 2012, 48, 6484-6486.
22. Huang, X. L.; Wang, R. Z.; XU, D.; Wang, Z. L.; Wang, H. G.; Xu, J. J.; Wu, Z.; Liu, Q. C.; Zhang, Y.; Zhang, X. B. *Adv. Funct. Mater.* 2013, 23, 4345-4353.
23. Gong, Y. J.; Yang, S. B.; Liu, Z.; Ma, L. L.; Vajtai, R.; Ajayan, P. M. *Adv. Mater.* 2013, 25, 3979-3984.
24. Bian X. J.; Scanlon, M. D.; Wang, S.; Liao, L.; Tang, Y.; Liu, B. H.; Girault, H. H. *Chem. Sci.* 2013, 4, 3432-3441.
25. Kong, D. S.; Wang, H. T.; Lu, Z. Y.; Cui, Y. *J. Am. Chem. Soc.* 2014, 136, 4897-4900.
26. Chang, Y. H.; Lin, C. T.; Chen, T. Y.; Hsu, C. L.; Lee, Y. H.; Zhang, W. J.; Wei, K. H.; Li, L. J. *Adv. Mater.* 2013, 25, 756-760.
27. Chang, Y. H.; Wu, F. Y.; Chen, T. Y.; Hsu, C. L.; Chen, C. H.; Wiryo, F.; Wei, K. H.; Chiang, C. Y.; Li, L. J. *Small* 2014, 10, 895-900.
28. Geim, A. K. *Science* 2009, 324, 1530.
29. Lv, W.; Tang, D. M.; He, Y. B.; You, C. H.; Shi, Z. Q.; Chen, X. C.; Chen, C. M.; Hou, P. X.; Liu, C.; Yang, Q. H. *ACS Nano* 2009, 3, 3730.
30. Loh, K. P.; Bao, Q. L.; Eda, G.; Chhowalla, M. *Nat. Chem.* 2010, 2, 1015.
31. Moon, I. K.; Lee, J.; Ruoff, R. S.; Lee, H. *Nat. Commun.* 2010, 1, 73.
32. Hummers, W. S.; Offeman, R. E. Preparation of graphitic oxide. *J. Am. Chem. Soc.* 1958, 80, 1339.
33. Zhou, Y.; Bao, Q. L.; Tang, L. A.; Zhong, Y. L.; Loh, K. P. Hydrothermal dehydration for the green reduction of exfoliated graphene oxide to graphene and demonstration of tunable optical limiting properties. *Chem. Mater.* 2009, 21, 2950-2956.
34. Peng, S.; Li, L.; Han, X.; Sun, W.; Srinivasan, M.; Mhaisalkar, S. G.; Cheng, F.; Yan, Q.; Chen, J.; Ramakrishna, S. *Angew. Chem. Int. Ed.* 2014, 53, 12594-12599.
35. T. Erdey-Gruz and M. Volmer, *Z. Phys. Chem.*, 150 (1930) 203.
36. J. Heyrovsky, *Recueil Des Travaux Chimiques Des Pays-Bas*, 46 (1927) 582.
37. J. Tafel, *Z. Phys. Chem.*, 50 (1905) 641.
38. S. Trasatti, *J. Electroanal. Chem.*, 39 (1972) 163.
39. R. Parsons, *Trans. Faraday Soc.*, 54 (1958) 1053.
40. B. E. Conway and J. O. Bockris, *J. Chem. Phys.*, 26 (1957) 532.
41. J. Greeley, T. F. Jaramillo, J. Bonde, I. B. Chorkendorff, and J. K. Nørskov, *Nat. Mater.*, 5 (2006) 909.

42. L. I. Krishtalik and P. Delahay, eds., *Advances in Electrochemistry and Electrochemical Engineering*, Interscience, New York, 1970.
43. T. F. Jaramillo, K. P. Jorgensen, J. Bonde, J. H. Nielsen, S. Horch, and I. Chorkendorff, "Identification of active edge sites for electrochemical H<sub>2</sub> evolution from MoS<sub>2</sub> nanocatalysts," *Science*, vol. 317, pp. 100-102, 2007.
44. Sun, T.; Zhang, Z.; Xiao, J.; Chen, C.; Xiao, F.; Wang, S.; Liu, Y.; *Sci. Rep.* 2013, 3, 2527.
45. Seo, B.; Jung, G. Y.; Sa Y. J.; Jeong, H. Y.; Cheon, J. Y.; Lee, J. H.; Kim, H. Y.; Kim, J. C. Shin, H. S.; Kwak, S. K.; Joo, S. H. *ACS Nano* 2015, DOI: 10.1021/acsnano.5b00786
46. Li, H.; Yu, K.; Fuo, H.; Guo, B.; Lei, X.; Zhou Z. *J. Phys. Chem. C* 2015, 119, 7959-7968.
47. Chang, K.; Chen, W. X. *Chem. Commun.* 2011, 47, 4252–4254.
48. Okpalugo, T. I. T.; Papakonstantinou, P.; Murphy, H.; McLaughlin, J.; Brown, N. M. D. *Carbon* 2005, 43, 153-161.
49. Lee, K. R.; Lee, K. U.; Lee, J. W.; Ahn, B. T.; Woo, S. L. *Electrochem. Commun.* 2010, 12, 1052-1055.
50. Eda, G.; Yamaguchi, H.; Voiry, D.; Fujita, T.; Chen, M.; Chhowalla, M.; *Nano Lett.* 2011, 11, 5111-5116.
51. Park, W.; Baik, J.; Kim, T.-Y.; Cho, K.; Hong, W.-K.; Shin, H.-J.; Lee, T. *ACS Nano*, 2014, 8, 4961-4968.
52. Sun, Z.; Zhao, Q., Zhang, G.; Li, Y.; Zhang, G.; Zhang, F.; Fan, X. *RSC Adv.* 2015, 5, 10352-10357.
53. Verble, J. L.; Wieting, T. J. *Phys. Rev. Lett.* 1970, 25, 362.
54. Li, Q.; Walter, E. C.; van der Veer, W. E.; Murray, B. J.; Newberg, J. T.; Bohannan, E. W.; Switzer, J. A.; Hemminger, J. C.; Penner, R. M. *J. Phys. Chem. B* 2005, 109, 3169-3182.
55. Plechinger, G.; Heydrich, S.; Eroms, J.; Weiss, D.; Schuller, C.; Korn, T. *Appl. Phys. Lett.* 2012, 101, 101906.
56. Wang, Z.; Chen, T.; Chen, W. X.; Chang K.; Ma, L.; Huang, G. C.; Chen, D. Y.; Lee, J. Y. *J. Mater. Chem. A* 2013, 1, 2202.
57. Conway, B. E.; Tilak, B. V. *Electrochim. Acta* 2002, 47, 3571.
58. Liao, T.; Sun, Z.; Sun, C.; Dou, S. X.; Searles, D. J. *Sci. Rep.* 2014, 4, 6256.
59. Ressler, T.; Wienold, R. E. J.; Gunter, M. M.; Timpe, O. *J. Phys. Chem. B* 2000, 104, 6360-6370.

## Chapter 6 Synthesis and Characterization of ZnO/PMMA Polymer Nanocomposites

### 6.1 Introduction

Polymer nanocomposites recently have got an immense interest as a demand to mix inorganic nanomaterials in organic polymers by creating new materials having excellent physical, optical, mechanical and chemical properties <sup>[1-6]</sup>. The most challenging part in the synthesis of polymer nanocomposite is to achieve a uniform filler distribution inside the host matrix. It has been understood from the literature survey that uniform distribution of inorganic nanomaterial in the polymer matrix is not possible because nanoparticles tends to agglomerate due to its high surface energy. Different strategies have been employed to circumvent the agglomeration of nanoparticles inside the host matrix. One of the methods is the ex-situ synthesis in which the nanoparticles are prepared independently, isolated and purified. Consequently, they are blended with monomer solution and in-situ polymerization is carried out <sup>[7]</sup>. The challenging part of this approach is the homogenous and good dispersion of nanoparticles inside the host matrix and long term stability against aggregation is required. The second approach is the mixing of precipitated nanoparticles inside a pre-formed polymer matrix <sup>[8]</sup>. This approach includes a common solution mixing method in which nanoparticles are dispersed and polymer matrix is dissolved separately, in a common solvent or two different solvents which are soluble in each other. Therefore, the two solutions are mixed together and thin films are achieved through spin coating or solution casting. This approach also requires a good dispersion of nanoparticles in the suitable solvent and polymer matrix. However, this requirement is fulfilled by the modification of nanoparticle surface with different surfactants. The third approach is the in-situ precipitation of nanoparticles in the organic matrix, which may consist of a bulk polymer, polymer solution or monomer <sup>[9-11]</sup>. One of the main ideas behind this method is that polymer as a host does not provide a sufficiently fluid environment to allow each nanoparticle to meet with each other by diffusion; thus, the aggregation of particles may be prevented for reasons of kinetics <sup>[12-16]</sup>. In all of the above discussed methods, solution mixing is a cost effective way to achieve nanocomposite thin films and provides more advantages than other conventional methods include better dispersion of nanoparticles in the polymer matrix and reactions performed at a very low temperature.

Poly(methyl methacrylate), or PMMA, is a key and essential thermoplastic for numerous uses and especially for optical applications due to excellent transparency in the visible region. Nevertheless, PMMA has limited properties, mainly its low toughness and poor thermal stability. ZnO is a renowned semiconductor with an extensive band gap of 3.37 eV, a large exciton binding energy of 60 meV and excellent radiation hardness<sup>[17]</sup>. It has a refractive index of 2.02 at wavelength of 589 nm, a thermal conductivity of 1.16 W.m<sup>-1</sup> K<sup>-1</sup> at a temperature of 50 °C and an electrical conductivity of 0.02 S.cm<sup>-1</sup>. All of these values are substantially higher than those of PMMA, 1.49, 0.19 W.m<sup>-1</sup>K<sup>-1</sup> and 10<sup>16</sup> S.cm<sup>-1</sup>, respectively, at the certain conditions<sup>[18-22]</sup>. By uniting these two materials, it would have several conceivable applications, such as in anti-reflection coatings, flame retardant materials, UV protecting films, transparent barrier/shielding layers and coatings

Recently, there have been reports on the preparation of PMMA/ZnO nanocomposites. Agrawal *et al.*<sup>[23]</sup> reported solution mixing of ZnO nanoparticles into PMMA and showed a improved dispersion and good thermal stability of PMMA/ZnO nanocomposite thin films. Demir *et al.* and Liu *et al.* prepared PMMA/ZnO composite films through *in-situ* polymerization of methyl methacrylate (MMA) monomers in the existence of organically modified ZnO nanoparticles<sup>[24-26]</sup>. Thermal stability and UV absorption properties were described to increase with increasing the ZnO content. Whang *et al.* and Hung *et al.* have reported on the luminescence of ZnO/poly(hydroxyethyl methacrylate) films where the ZnO particles had been formed by a sol/gel method and treated with a silane coupling agent before the polymerization was attained<sup>[27]</sup>. Liufu *et al.*, inspected the thermal degradation of polyacrylate/ZnO composites and recommended that the ZnO nanoparticles have equal role in stabilization and destabilization, depending on the temperature region<sup>[28]</sup>.

In this chapter, we emphasizes on the development of a facile solution based method to synthesize PMMA/ZnO nanocomposite via a solution mixing and casting method, and primarily investigate the structural, morphological and optical properties of the polymer nanocomposites. In this method, we, firstly, prepare ZnO nanoparticles through sol-gel method and these nanoparticles were dispersed in PMMA through solution mixing method using a common solvent N,N-dimethylacetamide (DMAc). The structural, optical, morphological and thermal properties of ZnO/PMMA nanocomposite with different ZnO content were investigated. It is found that ZnO nanoparticles with a size of 4-8 nm were homogeneously dispersed in PMMA matrix and shows a high thermal stability.

## 6.2 Optical Properties of Polymer Nanocomposites

Optical properties and applications of polymer nanocomposites may be the first known functions beginning from the earliest ages and have attracted observance for centuries. Inorganic nanoparticles, specifically metals and semiconductors, have received increasing consideration as ‘transparent nano-fillers’ for the polymer nanocomposites during the past two decades. Polymer nanocomposites for optical applications take benefit of the optical properties of materials that are hard to grow in single crystal form or that require protection from the environment and give them the ease of processing afforded many polymers. In addition, the inorganic nanoparticles can be used to achieve specific optical properties, and the polymer matrix is used just to hold the particles together and provide processability. In this chapter, the ability of inorganic nanoparticles, such ZnO, to serve as optically effective additives for polymer nanocomposites will be exploited.

The Size of the inorganic nanoparticles used as the nano-fillers is an important feature that bothers many optical properties and applications of the polymer nanocomposites. For instance, the emission spectra which includes photoluminescence of polymer and semiconductor quantum dots nanocomposites is reliant on the size of quantum dots; the color and refractive index of polymer and metal nanocomposites are also reliant on on the size of metal nanoparticles. In common, the major inevitability of inorganic nanoparticles to be used as optically effective additives for transparent polymers is a small size, which must be less than 40 nm. Rayleigh's Law can be employed to evaluate the intensity of the light loss when passing via a nanocomposite by scattering, as presented in equation 6.1:

$$\frac{I}{I_0} = \exp - \left\{ \frac{3\phi_p x r^3}{4\lambda^4} \left( \frac{n_p}{n_m} - 1 \right) \right\} \quad 6.1$$

where  $I$  is the intensity of the transmitted light and  $I_0$  is the intensity of incident light,  $\phi_p$  is the volume fraction of the nanoscale particles,  $x$  is the length of the optical,  $r$  is the radius of the sphere-shaped nanoparticles,  $\lambda$  is the wavelength of the light used,  $n_p$  is the refractive index of the particles, and  $n_m$  is the refractive index of the polymeric matrix. It can be noticeably seen from Equation 6.1 that the loss of light by scattering phenomena severely increases with particle size. Generally, 40 nm is the limiting size for nanoparticle diameters to circumvent intensity loss of transmitted light due to Rayleigh scattering [34]. The transparency/opaqueness is also reliant on the variance of the refractive index between nanoparticles and the polymer matrix, and the dispersion or accumulation of nanoparticles into the polymer matrix. When the refractive index of nanoparticles and the polymer matrix is near, transparency can also be accomplished with the bigger nanoparticles. Agglomeration of nanoparticles into matrix material will cause a proliferation in opacity. The arrangement of



nanoparticles into the polymer matrix is an additional substantial factor that bothers the optical properties of polymer nanocomposites. Disorderly distribution of separately dispersed nanoparticles helps in optical transparency, emissivity and photoluminescence, and UV absorption; well-arranged nanoparticles can lead to the iridescence; while uniaxially arranged nanoparticles can lead to dichroism.

## 6.3 Experimental Details

### 6.3.1 Chemical Reagents

All chemicals were of the highest purity available and were used as received. Polymethylmethacrylate (PMMA,  $\langle MW \rangle = 120,000$  D) was purchased from Alfa Aesar (China). Zinc acetate dihydrate [ $Zn(Ac)_2 \cdot 2H_2O$ , 99%], potassium hydroxide (KOH, 99%) and DMAc were obtained from Sigma Aldrich (China). All solvents used were of analytical grade and were also purchased from Sigma-Aldrich.

### 6.3.2 Synthesis of ZnO Nanoparticles

ZnO nanoparticles were synthesized through a typical sol-gel process using  $Zn(Ac)_2 \cdot 2H_2O$  as a precursor material. In a typical procedure, 2.195 g of  $Zn(Ac)_2 \cdot 2H_2O$  was dissolved in 100ml of deionized water under stirring in the ambient atmosphere. 1.122g of KOH was dissolved in 10ml distilled water and was added to the above solution drop wise under continuous magnetic stirring. After a few minutes, solution turn into a jelly form and a milky white solution was obtained; the mixture was then further heated for 3 hours at  $90^\circ C$ . The product was centrifuged twice and rinsed with alcohol and deionized water several times, and air dried at  $80^\circ C$  for 12 hours.

### 6.3.3 Preparation of ZnO/PMMA Nanocomposite Thin Film

PMMA/ZnO nanocomposite films were prepared through a simple solution mixing and casting method. DMAc was selected as the solvent for mixing of ZnO nanoparticles into PMMA because PMMA and ZnO nanoparticles are well dispersed in this solvent. In a typical synthesis, 1 g PMMA was dissolved in 30ml of DMAc under continuous stirring at  $70^\circ C$ . In another beaker, different ZnO contents (0.5, 1.0, 1.5, 2.0 wt%) were dissolved in 20ml of DMAc and the resulting solution was subjected to ultrasonic vibration for 30 min to break apart the agglomerates. The resultant ZnO nanoparticles solution was added to the above solution. The mixture was subsequently heated to  $70^\circ C$  and stirred for 3 hours. The product

was again sonicated for 30 min. After sonication, nanocomposite films with a thickness of 2-4  $\mu\text{m}$  were obtained through film casting at 80  $^{\circ}\text{C}$  for 3 days.

### 6.3.4 Characterization Tools

The surface morphology of the samples was examined by using a field emission scanning electron microscope (FESEM, JEOL, JSM-6700F). The X-ray diffraction (XRD) patterns of the products were recorded using Rigaku powder X-ray diffractometer with  $\text{CuK}\alpha_1$  source ( $\lambda=1.5405 \text{ \AA}$ ) in  $\theta$ -2 $\theta$  configuration. Thermogravimetric analysis (TGA) was carried out using a TGA 7 (Perkin Elmer) instrument at a heating rate of 5  $\text{K}\cdot\text{min}^{-1}$  over a 23–700  $^{\circ}\text{C}$ . Differential scanning calorimetry (DSC) measurements were performed on a DSC Q 1000 from TA Instruments at a 10  $\text{K}\cdot\text{min}^{-1}$  heating rate in a nitrogen atmosphere. Room temperature optical absorption spectra in the UV and visible wavelength regions were recorded on a Shimadzu spectrophotometer (SOLID3700). Photoluminescence (PL) emission was measured using Nd-YAG laser with a 325 nm excitation source and recording the luminescence with a spectrometer together with a photomultiplier tube.

## 6.4 Results & Discussion

### 6.4.1 Structural Characterization

The structural and crystalline phases of PMMA/ZnO nanocomposites were identified by X-ray diffraction studies. Figure 1 shows the XRD patterns for nanocomposite films loaded with different ZnO contents. All the diffraction patterns revealed the broad non-crystalline peak ( $13.38^{\circ}$ ) of PMMA and sharp diffraction peaks of ZnO nanoparticles <sup>[35]</sup>. The diffraction peak intensities of nanocomposite films have been found to increase with increasing ZnO contents in the PMMA matrix <sup>[36]</sup>. These diffraction patterns show a highly crystalline hexagonal wurtzite structure of ZnO with a lattice constant of  $a=3.245$  and  $c=5.197$  which are consistent with the standard values for bulk ZnO (JCPDS card no. 36-1451).

The average crystallite size is calculated from the XRD pattern using the Scherrer's equation <sup>[37]</sup> (Equation 6.2) with the integral widths corrected with the standard Si sample (Equation 6.3) using the Cauchy-Lorentzian fit. The crystallite size was calculated from the average of the high intensity peaks (100), (002) and (101) and (110) of the hexagonal phases of ZnO.

$$L = \frac{0.9\lambda}{\beta_{hkl}\cos\theta} \quad 6.2$$

where,  $L$  is the average crystallite size,  $\lambda$  is the wavelength ( $1.5405 \text{ \AA}$ ) of Cu  $K_{\alpha 1}$  radiation,  $\beta_{hkl}$  is the instrumental corrected FWHM in radians and  $\theta$  is the scattering angle in degree. The corrected instrumental broadening for Lorentzian is given by

$$\beta_{hkl} = \beta_{measured} - \beta_{instrumental} \quad 6.3$$

According to the data presented in Figure 6.1, the average particle size of the ZnO nanocrystals determined on the basis of Equation (6.2) for the (100), (002) and (101) diffraction peaks was found to be about 14.4nm. The incorporation of ZnO nanoparticles into PMMA produces neither new diffraction peak nor a peak shift, showing that nano ZnO filled PMMA composite consists of phase separated structures, i.e., polymer PMMA and ZnO nanoparticle.

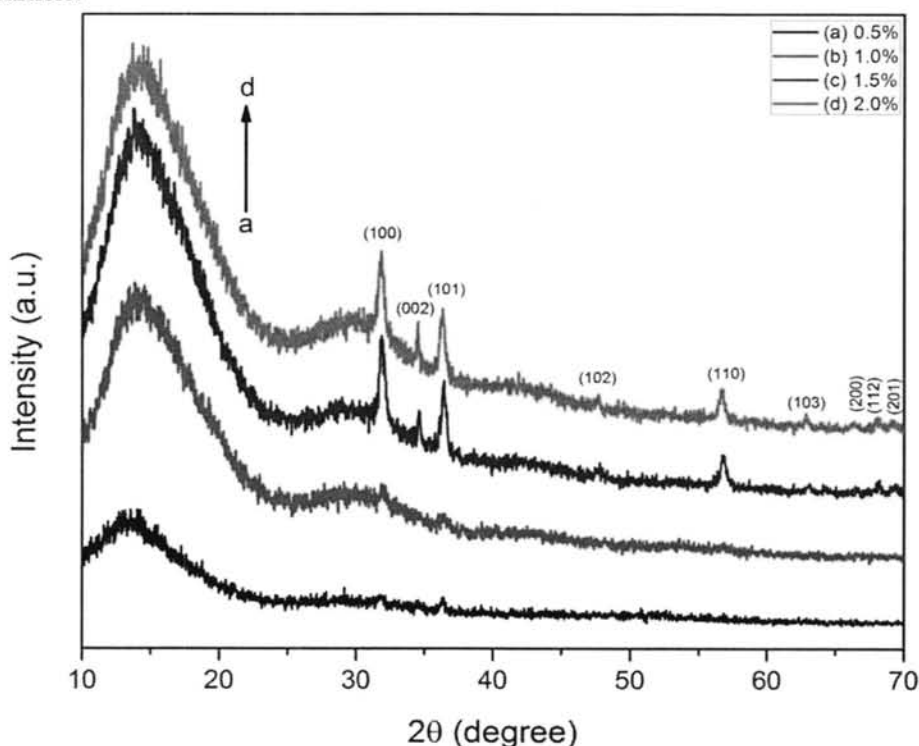


**Figure 6.1** XRD patterns of PMMA/ZnO nanocomposite films loaded with different amount of ZnO nanoparticles.

#### 6.4.2 Surface Morphology

In the nanoscale range, a morphological investigation on the prepared nanocomposites has been accomplished by analyzing SEM images of the PMMA/ZnO nanocomposites and the results are shown in Figure 6.2. Analysis of microscopy images clearly shows a nearly uniform global distribution of the ZnO nanoparticles in the polymer matrix. It can also be seen from Figure 6.2a, 6.2b and 6.2c that ZnO nanoparticle, with average particle size of 4-8

nm, uniformly dispersed in a largely amorphous phase of PMMA matrix. This uniform dispersion is due to the strong interaction of ZnO nanoparticle with the polar solvent DMAc, used as the common solvent for mixing of ZnO into the polymer matrix, which plays a vital role in breaking the agglomerates and produces the uniform dispersion of ZnO nanoparticles in the final nanocomposite films<sup>[23]</sup>. However, distinct local aggregation can also be found as the concentration of ZnO nanoparticle increases in the polymer matrix (Figure 6.2d). The size of these local aggregates ranges from 10-20nm. These local aggregates were probably found because of high surface energy of ZnO nanoparticles. It is a real and eminent fact that the efficiency of the nanoparticles in improving the properties of the polymeric materials is predominantly determined by the degree of its dispersion in the polymer matrix. The significance of the described approach lies in the fact that it offers the same or an even improved level of dispersion of ZnO nanoparticles into the polymer matrix, related to what has been attained using previously reported methods, time-consuming and costly methods [25,38,39].

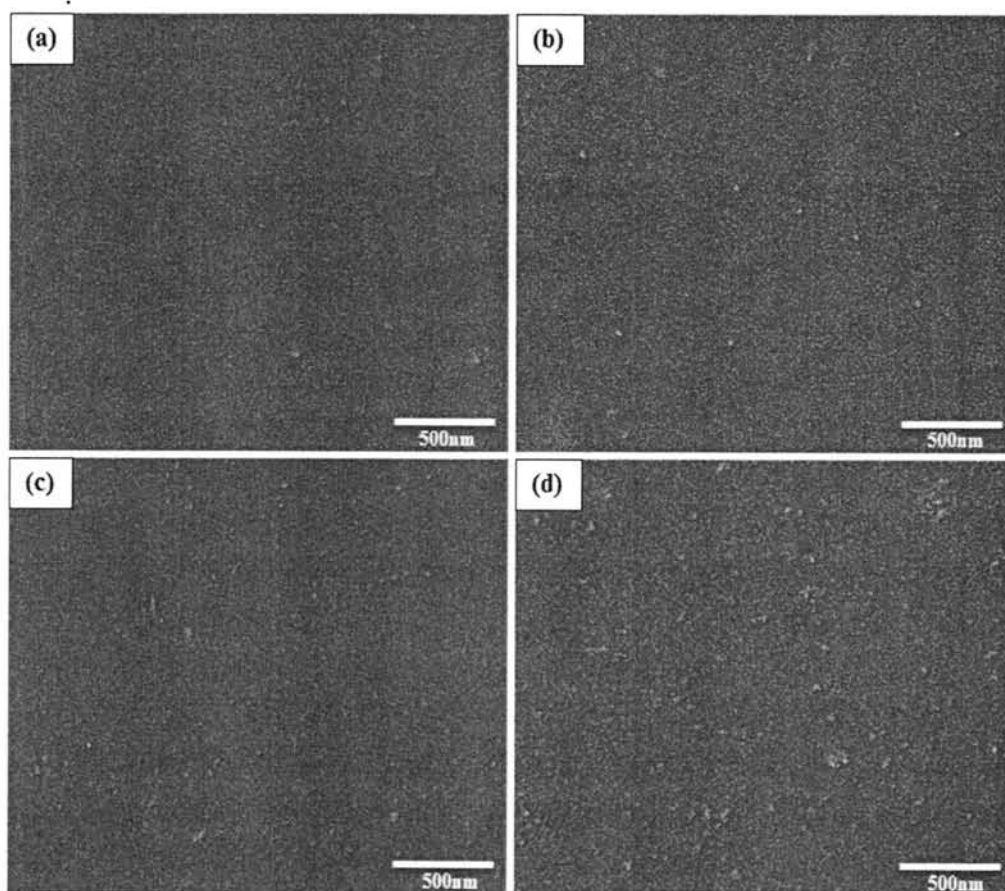


**Figure 6.2** SEM images of PMMA/ZnO nanocomposite films with (a) 0.5 wt% (b) 1.0 wt% (c) 1.5 wt% (d) 2.0 wt % filler contents.

### 6.4.3 Thermal Properties

Pure poly(methyl methacrylate) is deemed to have poor thermal behavior. A study of thermal degradation temperature of PMMA by TG exhibited that the polymer degrades in three steps at 180, 250, and 350 °C with a heating rate of 10 °C min<sup>-1</sup> [40]. The degradation mechanisms are known as the scission of H–H linkage, the scission of the vinylidene end group, and the random scission of the polymer main chain, respectively. In our study, two degradation steps were observed in the pure PMMA film, as shown in the Figure 6.3. The first degradation step is observed at 150 °C which is associated with scissions at the H-H linkage and the unsaturated end group and the second peak observed at 355 °C which is attributed by the degradation of the polymer main chain. Moreover, PMMA polymerized in the presence of oxygen environment will form sporadic peroxide linkages. In the presence of oxygen, the thermal degradation of PMMA is suppressed predominantly at low temperature [41,42]. The radical created from head-to-head scission and unsaturated end group can react with oxygen molecules and form more stable species which consequently improves the thermal stability of PMMA at low temperature.

The thermal stability of PMMA is improved by the incorporation of ZnO nanoparticles Figure 6.3 illustrates TGA scans of the pure PMMA film and PMMA/ZnO nanocomposite film loaded with different filler contents. It is clearly evident from Figure 3 that three main peaks were observed with the incorporation of ZnO content. The first degradation step occurs at 172, 175, 175 and 173 °C, while the second degradation step occurs at 279, 278, 274 and 269 °C, and the third main degradation step occurs at 370, 375, 376 and 377 °C for 0.5, 1.0, 1.5 and 2.0 wt% ZnO filler contents, respectively. The main random chain scission increases from 355 °C (neat PMMA) to 377 °C (2.0 wt %). This enhancement of the thermal stability can be attributed to the nanoparticles preventing out-diffusion of the volatile decomposition products. Two mechanisms are normally used to explain the increase in the thermal degradation temperature of the polymer nanocomposites. Both mechanisms include disruption of the physical and/or chemical environment of the polymer. The first mechanism is simply consist of steric hindrance of polymer chain motion that decreases thermally induced strain on the polymer backbone and also reduces the number of chain-scission-promoting encounters with neighboring moieties [43]. The second mechanism, which is not well recognized in the literature, addresses the chemical inducing and inhibiting effects of nanoparticle oxide surfaces. The localization of the charge arising from the carbonyl dipole and similar surface moieties may be effective in promoting bond scission, particularly as the charge destabilizes polymer units and promotes various scissions including the vinylidene

decomposition. Contradicting this mechanism is the tendency for nanoparticles to act as defect getters during the synthesis process, which reduces the concentration of H–H linkage and unsaturated end groups during polymer degradation, thus stabilizing the composite during subsequent heating [25,44].

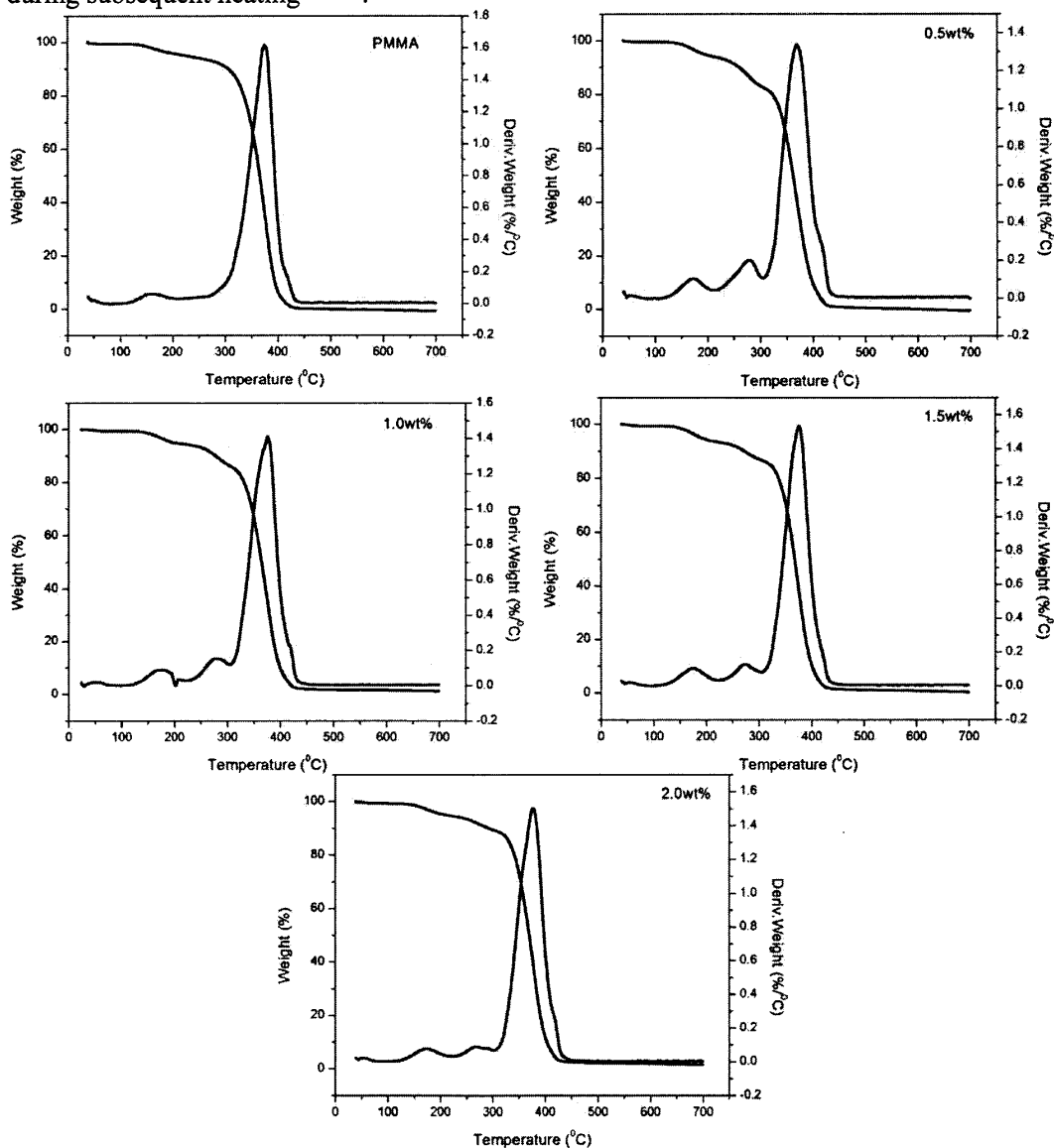


**Figure 6.3** TGA and DTG curves of PMMA films before and after the loading of different amount of ZnO nanoparticles, taken in nitrogen atmosphere.

In order to determine whether the enhancement in thermal stability is caused by chain restriction, the glass transition temperature ( $T_g$ ) of bare PMMA film and ZnO/PMMA composite film was examined, as shown in Figure 6.4. Figure 6.4(a) shows DSC scans of PMMA/ZnO composite films taken at  $10 \text{ K}\cdot\text{min}^{-1}$  heating rate in a nitrogen atmosphere. One

can observe that the incorporation of ZnO nanoparticles led to an increase in the glass transition temperature of the PMMA matrix, as apparent by the peak maxima of the heat flow curve. Since glass transition temperature ( $T_g$ ) is directly related to the polymer chain mobility. Thus, according to this concept, if nanoparticles are added to the polymer they will hinder polymer chain motion and  $T_g$  will increase. On the other hand, there are data based on studies of thin polymer films and on certain nanocomposites that show a decrease in  $T_g$  as the film thickness (or the spacing between non-functionalized nanoparticles) decreases<sup>[45]</sup>. The main point of view is that if the polymer is not constrained at its boundaries, as in a bare film or in nanocomposites of non-functionalized particles, the structural relaxation process can continue to a more stabilized state corresponding to a lower  $T_g$ . In this work, we observed the glass transition temperature values of 92.39, 106.65, 118.54, 94.97, 110.35 °C for neat PMMA, 0.5, 1.0, 1.5, and 2.0 wt% films, respectively.

Figure 6.4(b) shows the variation in glass transition temperature ( $T_g$ ) as a function of the ZnO contents and reveals that the mixing of 1.5wt% ZnO leads to a maximum shift in  $T_g$  towards higher temperature. In agreement with the TGA results, a decrease in  $T_g$  with a further increase in filler content can be ascribed to a slight increase in the degree of aggregation at a higher loading of ZnO. The existence of enormous agglomeration in the polymer matrix reduces a high free volume to the polymer chains, existing around the filler domains, proposing easiness in their mobility. An increased  $T_g$  of the PMMA/ZnO nanocomposite films appears to be affected mainly by confinement of the polymer chains near to ZnO nanoparticle rather than by tethering due to little interaction between ZnO and PMMA<sup>[46]</sup>.

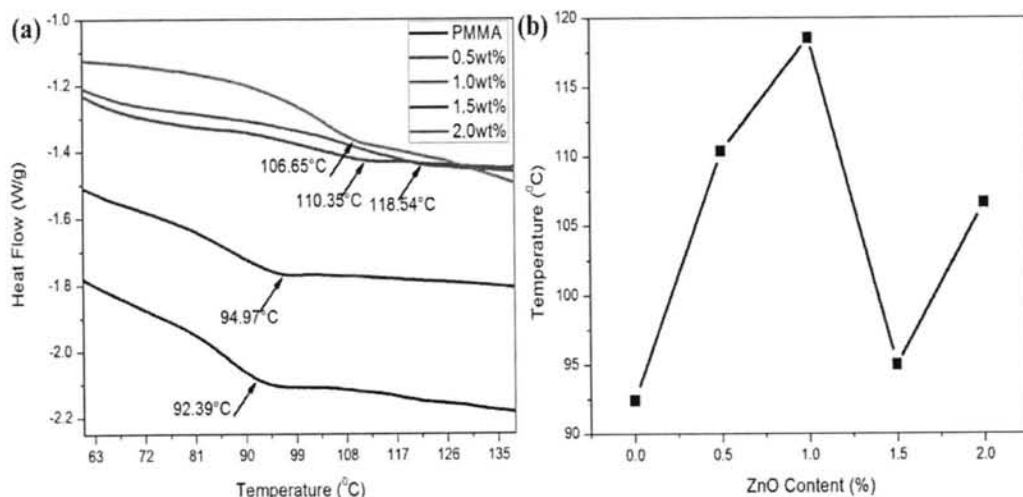


**Figure 6.4** (a) DSC scans of PMMA/ZnO films loaded with different amounts of ZnO nanoparticles (b) The variation in glass transition temperature ( $T_g$ ) as a function of the ZnO contents.

## 6.4.4 Optical Characterization

### 6.4.4.1 UV-Visible Absorption Spectroscopy

The effect of the incorporation of ZnO nanoparticles in PMMA was investigated by UV-visible absorption spectroscopy. The absorption spectra of the PMMA based ZnO nanocomposite films at different ZnO loading contents are shown in Figure 6.5. Figure 6.5(a) demonstrates the onset of absorbance for these films in the range 337-347 nm, which can be attributed to the excitation of electrons from the valence band to the conduction band of ZnO. Furthermore, one can observe that the intensity of this band increase with an increase in ZnO content. The onset of the absorption shows a red shift and therefore a decrease in the band gap of ZnO with increasing the filler content in composite films. Yuwono *et al.* reported similar behavior for TiO<sub>2</sub> nanoparticles dispersed into a polymer matrix [47]. It should be noted that the nonappearance of the absorption band in the visible region of these UV absorption spectra indicates that the prepared PMMA/ZnO nanocomposite does not contain color centers and can readily be used as transparent UV-absorbing materials.

The optical transmissions of the nanocomposite films at two different wavelengths, that is at 350 and 550 nm, as a function of the ZnO content is shown in Figure 6.5(b). As we know that ZnO does not absorb in the visible region, hence we can assume that the loss of transparency in this visible region will be caused only by the scattering of nanoparticles. One can detect from Figure 6.5(b) that there is an insignificant decrease in the transparency of composite films till the loading level is 0.5 wt%. Certainly, these values are very similar to that of the pure PMMA film, i.e. 92% [24]. It proposes that, in this concentration range, our particles are small enough so that scattering losses are insignificant, and the composite films are nearly as transparent as PMMA itself. It is a known fact that the transmission of pure PMMA films for 550 nm light at normal incidence is about 92% only accordingly of the reflection losses on air/film, film/substrate and substrate/air interfaces and not for the reason that of absorption and scattering losses. An additional increase in the ZnO content of composite films from 0.5 to 2 wt% causes a substantial decrease in transparency as, at higher filler contents, particles are more likely agglomerated in the polymer matrix and hence certainly cause optical scattering. It is noteworthy that transmission loss of such a multiphase system depends on several limitations, such as the concentration of particles, the refractive index difference between the particles and the polymer matrix, the size of the inorganic domains and the thickness of the films studied. Furthermore, Figure 6.5(b) exposes that PMMA/ZnO nanocomposite films strongly absorb in the UV region, compare to that of the visible one. This can be ascribed to the wide band gap and hence the higher absorption



coefficient of ZnO nanoparticles in this spectral region [48]. It is also observed that with the increase in filler content transmission decays exponentially at 350nm. These results obviously specify that the obtained PMMA/ZnO composites can be used as UV-shielding materials, which are practically transparent in the visible region.

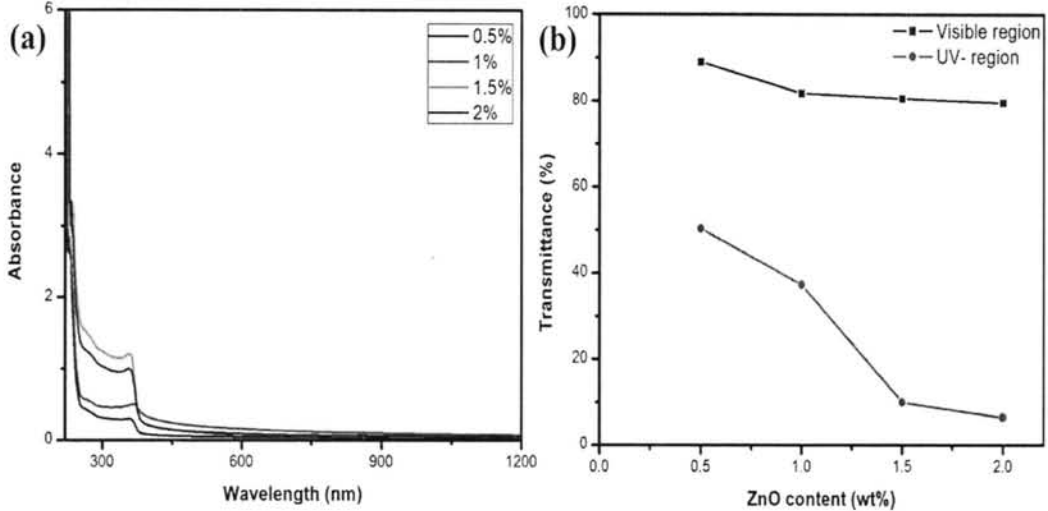


**Figure 6.5** (a) UV-Vis spectra of PMMA/ZnO nanocomposite films loaded with different amounts of ZnO nanoparticles. (b) Transmittance of PMMA/ZnO nanocomposite films as a function of filler content in the UV (350 nm) and visible regions (550 nm).

#### 6.4.4.2 Photoluminescence

Figure 6.6 shows the room temperature PL emission spectra of PMMA based ZnO nanocomposite films at different ZnO loading contents recorded using an excitation at 325nm. Since the semiconductor ZnO nanoparticles, with sizes comparable to or below their exciton Bohr radius, have characteristic electronic and optical behaviors due to exciton quantum confinement phenomena [49]. It is imminent that the room temperature PL spectra of the ZnO nanoparticles show three main peaks, a UV peak near band-edge emission around 380 nm, a green emission peak around 520 nm and an orange-red emission around 600 nm. The emission in the UV region is called the near band-edge emission, produced by the free-exciton recombination and the visible region known to be deep-level emission appearing owing to the structural defects and impurities in the structures. The PL spectra of PMMA/ZnO nanocomposite films possess one obvious intrinsic UV emission peak in the range of 378.38-379.11 nm, which corresponds to the exciton recombination related to the near-band edge emission. Clearly, the intensity of UV emission peak (around 379) increased as the concentration of ZnO nanoparticles increased in the polymer matrix. However, Figure 6 also indicate a broad deep level visible emission (DLE) ranging from 450-625 nm, centered

at 516 nm for PMMA based ZnO nanocomposite films at 0.5, 1.5 and 2 wt% ZnO loading contents, which is attributed to the recombination between the electrons in a deep defect level or a surface defect level and the holes in the valence band<sup>[50-51]</sup>. It is also clearly evident from Figure 6.6 that deep level visible emission (DLE) has not been observed for 1.0 wt%, indicating pure ZnO nanoparticles with no defects. These results more clearly demonstrate that the obtained PMMA/ZnO composites, specifically with no defects, can be used as UV-shielding materials, which are practically transparent in the visible region.

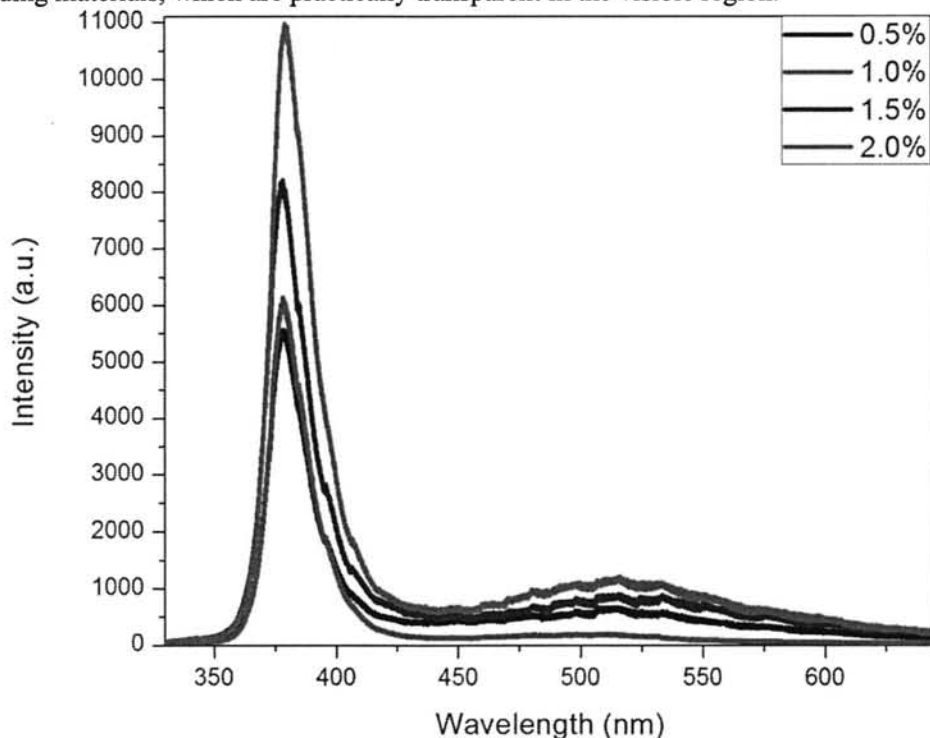


**Figure 6.6** Room temperature photoluminescence (PL) emission spectra of PMMA/ZnO nanocomposite films loaded with different amounts of ZnO nanoparticles.

## 6.5 Summary

In summary, we demonstrated a very simple and facile solution mixing approach for the synthesis of PMMA/ZnO nanocomposites. The prepared PMMA/ZnO nanocomposites possess no color, high transparency, and good thermal stability, UV shielding capability, luminescence and homogeneity. The chemical process involved solution mixing of ZnO nanoparticles dispersed in DMAc with the PMMA matrix dissolved in the same solvent. The effect of ZnO content on the physical properties of the PMMA matrix is investigated by X-ray diffraction, field emission scanning electron microscopy, thermo-gravimetric analysis,

UV-Vis absorption and photoluminescence spectroscopy. It was found that pure hexagonal ZnO nanoparticles with an average particle size of 4-8 nm were homogeneously dispersed in the PMMA matrix. A significant improvement in thermal properties was observed with the incorporation of 1.0 wt% ZnO nanoparticles. The prepared nanocomposite films are highly transparent and a clear excitonic peak is observed in their absorption spectra. Measurement of room temperature photoluminescence spectra shows intensive near-band edge emission peak at 3.28eV without any structural defects for a nanocomposite film with a filler content of 1.0 wt%. Moreover, the PMMA/ZnO nanocomposites films were highly transparent and possess good absorption of light in the UV region which can strongly shield harmful UV light for human health. The low cost, non-toxicity, long-term stability, bright luminescence, and high UV shielding efficiency of final PMMA/ZnO nanocomposites make them extremely promising and applicable as optical materials.

## 6.6 References

1. C. Arango, L. R. Johnson, V. N. Bliznyuk, Z. Schlesinger, S. A. Carter, H. H. Horhold, *Adv. Mater.* 12 (2000), 1689.
2. W. U. Huynh, J. J. Dittmer, A. P. Alivisatos, *Science* 295 (2002), 2425.
3. G. Kickelbick, *Prog. Polym. Sci.* 28 (2003), 83.
4. M. Agrawal, A. Pich, S. Gupta, N. E. Zafeiropoulos, J. R. Retama, M. Stamm, *J. Mater. Chem.* 18 (2008), 2581.
5. M. Agrawal, A. Pich, N. E. Zafeiropoulos, M. Stamm, *Colloid Polym. Sci.* 286 (2008), 593.
6. M. Agrawal, N. E. Zafeiropoulos, S. Gupta, E. Svetushkina, A. Pich, M. Stamm, *Macromol. Rapid Commun.* 31 (2010), 405.
7. J. Lee, V. C. Sundar, J. R. Heine, M. G. Bawendi, K. F. Jensen, *Adv. Mater.* 12 (2000), 1102.
8. C. H. Dan, Y. D. Kim, M. Lee, B. H. Min, J. H. Kim, *J. Appl. Polym. Sci.* 108 (2008), 2128.
9. T. K. Leodidou, P. Margraf, W. Caseri, U. W. Suter, P. Walther, *Polym. Adv. Technol.* 8 (1997), 505.
10. R. F. Mulligan, A. A. Iliadis, P. Kofinas, *J. Appl. Polym. Sci.* 89, (2003), 1058.
11. I. W. Mikrajuddin Lenggoro, K. Okuyama, F. G. Shi, *J. Electrochem. Soc.* 149 (2002), H107.
12. M. R. Bockstaller, R. A. Mickiewicz, E. L. Thomas, *Adv. Mater.* 17 (2005), 1331.

13. S. M. De Paul, J. W. Zwanziger, R. Ulrich, U. Wiesner, H. W. Spiess, *J. Am. Chem. Soc.* 121 (1999), 5727.
14. L. H. Lee, W. C. Chen, *Chem. Mater.* 13 (2001), 1137.
15. J. Y. Wen, G. L. Wilkes, *Chem. Mater.* 8 (1996), 1667.
16. R. Palkovits, H. Althues, A. Rumplecker, B. Tesche, A. Dreier, U. Holle, G. Fink, C. H. Cheng, D. F. Shantz, S. Kaskel, *Langmuir* 21 (2005), 6048.
17. U. Ozgur, Y. I. Alivov, C. Lui, A. Teke, M. A. Reshchikov, S. Dogan, V. Avrutin, S. J. Cho, H. Morkoc, *J. Appl. Phys.*, 98 (2005), 041301.
18. D. R. Lide, *CRC Handbook of Chemistry and Physics*, 76th edition, Ed., CRC Press, Boca Raton (1995), p. 4/138.
19. T. Olorunyolemi, A. Birnboim, Y. Carmel, O. C. Wilson, I. K. Lloyd, S. Smith, R. Campbell, *J. Am. Ceram. Soc.* 85 (2002), 1249.
20. D. C. Look, *Semicond. Sci. Technol.* 20 (2005), S55.
21. W. Wunderlich, *Polymer Handbook*, 4th edition, J. Brandrup, E. H. Immergut, E. A. Grulke, Eds. J Wiley & Sons, New York (1999), p. V/87.
22. W. G. Zheng, S. C. Wong, H. J. Sue, *Polymer* 43 (2002), 6767.
23. M. Agrawal, S. Gupta, N. E. Zafeiropoulos, U. Oertel, R. Habler, M. Stamm, *Macromol. Chem. Phys.*, 211 (2010), 1925.
24. M. M. Demir, K. Koynov, U. Akbey, C. Bubeck, I. Park, I. Lieberwirth, G. Wegner, *Macromolecules* 40 (2007), 1089.
25. M. M. Demir, M. Memesa, P. Castignollesb, G. Wegner, *Macromol. Rapid Commun.* 27 (2006), 763.
26. P. Liu, Z. Su, *J. Macromol. Sci., Phys.* 45 (2006), 131.
27. C. H. Hung, W. T. Whang, *J. Mater. Chem.* 15 (2005), 267.
28. S. C. Liufu, H. N. Xiao, Y. P. Li, *Polym. Degrad. Stab.* 87 (2005), 103.
29. Wang, J.; Cao, J.; Fang, B.; Lu, P.; Deng, S.; Wang, H. Synthesis and characterization of multipod, flower-like, and shuttle-like ZnO frameworks in ionic liquids. *Mater. Lett.* 2005, 59, 1405–1408.
30. Wang, Z.L. Splendid one-dimensional nanostructures of zinc oxide: A new nanomaterial family for nanotechnology. *ACS Nano* 2008, 2, 1987-1992.
31. J. Nishii, F.M. Hossain, S. Takagi, T. Aita, K. Saikusa, Y. Ohmaki, I. Ohkubo, S. Kishimoto, A. Ohtomo, T. Fukumura, F. Matsukura, Y. Ohno, H. Koinuma, H. Ohno, and M. Kawasaki, *Jpn. J. Appl. Phys.* 42, L347 (2003).

32. F. M. Hossain, J. Nishii, S. Takagi, T. Sugihara, A. Ohtomo, T. Fukumura, H. Koinuma, H. Ohno, M. Kawasaki, *Physica E* 21, 911 (2004).
33. Radzimska A K, Jesionowski, Zinc Oxide-From Synthesis to Application: A Review, *Materials* 2014, 7, 2833-2881.
34. Althues H, Henle J, Kaskel S. Functional inorganic nanofillers for transparent polymers. *Chem Soc Rev.* 2007; 36:1454-5.
35. L. D'Orazio, R. Guarino, C. Mancarella, E. Martuscelli, G. Cecchin, *J. Appl. Polym. Sci.* 66 (1997), 2377.
36. H. M. Xiong, X. Zhao, J. S. Chen, *J. Phys. Chem. B* 105 (2001), 10169.
37. N. R. Yogamalar, R. Srinivasan, A. Chandra Bose, *Opt. Mater.* 31 (2009), 1570.
38. V. Khrenov, M. Klapper, M. Koch, K. Müllen, *Macromol. Chem. Phys.* 206 (2005), 95.
39. S. C. Hsu, W. T. Whang, C. H. Hung, P. C. Chiang, Y. N. Hsiao, *Macromol. Chem. Phys.* 206 (2005), 291.
40. C. Dong, X. Ni, *J. Macromol. Sci. A.* 41 (2004), 547.
41. T. Kashiwagi, A. Inaba, J. E. Brown, K. Hatada, T. Kitayama, E. Masuda, *Macromolecules.* 19 (1986), 2160.
42. J. D. Peterson, S. Vyazovkin, C. A. Wight, *J. Phys. Chem. B.* 103 (1999), 8087.
43. A. Laachachia, M. Cocheza, M. Ferriola, J. M. Lopez-Cuestab, E. Leroy, *Mater. Lett.* 59 (2005), 36.
44. J. Zhu, Uhl FM, A. B. Morgan, C. A. Wilkie, *Chem. Mater.* 13 (2001), 4649.
45. L. Schadler, *Polymer-based and polymer-filled nanocomposites.* Wiley: Nanocomposite Science and Technology, (2003), p. 77–153.
46. D. A. Savin, J. Pyun, G. D. Patterson, T. Kowalewski, *J. Polym. Sci., Part B: Polym. Phys.* 40 (2002), 2667.
47. A. H. Yuwono, J. Xue, J. Wang, H. I. Elim, W. Ji, Y. Li, T. J. White, *J. Mater. Chem.* 13 (2003), 1475.
48. U. Ozgur, Y. I. Alivov, C. Liu, A. Teke, M. A. Reshchikov, S. Dogan, V. Avrutin, S. J. Cho, H. Morkoc, *J. Appl. Phys.* 98 (2005), 041301.
49. M. A. Gondal, Q. A. Drmosh, Z. H. Yamani, T. A. Saleh, *Appl. Surf. Sci.* 256 (2009), 298.
50. K. Vanheusden, W. L. Warren, C. H. Seager, D. R. Tallant, J. A. Voigt, B.E. Gnade, *J. Appl. Phys.* 79 (1996), 7983.
51. J. Yguerabide, E. E. Yguerabide, *Anal. Biochem.* 2 (1998), 137.

## Acknowledgements

Working on my Ph.D. thesis during the last three years in University of Science & Technology of China (USTC), Hefei is an unforgettable life journey for me. I think USTC and the city of Hefei is a perfect place for living, but what I enjoy most was the research during this period of time. So at first I want to thank my advisor, Professor Liangbin Li, for accepting me as a PhD student and bringing me into an exciting area of scientific study and leading me to the successful completion of this thesis. I am also thankful to my co-advisor Professor Zeming Qi for guiding me in my research and helping in my research articles. I would also like to thank Dr. Ningdong Huang, whose group leadership has allowed me to learn about and understand other areas of research as well as my own. I would also like to thank China Scholarship Council (CSC) for providing me with the funding and financial support.

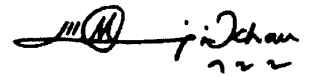
The research of this thesis is supported by the National Natural Science Foundation of China under grant no. 51325301 and 11204285.

I would like to thank Soft Matter Group and my fellow lab colleagues; Chengsha Wei, Mingming Chen, Jiaojiao Tao, Wu Xibo and Sarmad, all of whose hard work and dedication informed the success of this project. I would like to acknowledge and thank Ammar Bin Yousaf for helping in electrochemical characterizations and supporting me in every aspect of my life in USTC.

I would like to thank all my friends and colleagues in the USTC who I have not already mentioned for making my time in Hefei so pleasant. In particular I would like to thank Faisal Yousafzai, Murad Khan, Waqar Khan, Mohammad Rizwan Arif, Akif Zeb, Noor Ul Afsar, Asad Khan, Muhammad Imran, Munir Khan, Junaid Khaliq, Badar Munir, Quaid-e-Iqbal and Bakhtzada Khan. We share many wonderful memories exploring different cities and national parks across the China and trying different kinds of food around. I would also like to thank the staff of my department National Synchrotron Radiation Laboratory.

I am grateful to my family and my beloved ones, Shakeel Ahmad, Haroon Khan, Kamran Khan, little Ghazala Khan, little Maheer Khan and especially Xiaxia who gave me unlimited love and great support in every aspect of my life, and helped me a lot in completion of my Ph.D. At last, I want to thank my father and my mother, who always encouraged me to pursue higher education and gave me their love and support.

Inevitably, I might leave someone deserving my appreciation in helping me complete this thesis. Therefore, I am thankful to all of those who have contributed in some way to my success.

A handwritten signature in black ink, appearing to read 'Majid Khan' with a stylized flourish at the end.

**Majid Khan**

22/05/2015

## List of Publications

### List of publications included in this thesis

1. **Majid Khan\***, Ammar Bin Yousaf, Mingming Chen, Chengsha Wei, Xibu Wu, Ningdong Huang, Zeming Qi, Liangbin Li, Molybdenum Sulfide/Graphene-Carbon Nanotube Nanocomposite Material for Electrocatalytic Applications of Hydrogen Evolution Reactions, *Nano Research* 2015, submitted
2. **Majid Khan\***, Ammar Bin Yousf, Noor Ul Afsar, Muhammad Imran, Mingming Chen, Chengsha Wei, Xibu Wu, Ningdong Huang, Zeming Qi, Liangbin Li, Palladium Octahedral and Spherical Nanocrystals on Graphene Oxide: Their Comparative Studies as Anode Material for Direct Methanol Fuel Cells, *Advanced Material Letters* 2015, submitted
3. **Majid Khan\***, Ammar Bin Yousaf, Mingming Chen, Chengsha Wei, Xibu Wu, Ningdong Huang, Zeming Qi, Liangbin Li, Mixed-Phase Pd-Pt Bimetallic Alloy on Graphene Oxide with High Activity for Electrocatalytic Applications, *Journal of Power Sources* 282 (2015) 520-528.
4. **Majid Khan\***, Mingming Chen, Chengsha Wei, Jiaojiao, Ningdong Huang, Zeming Qi, Liangbin Li, Synthesis at the nanoscale of ZnO into poly(methyl methacrylate) and its characterization, *Applied Physics A* 117 (2014) 1085-1093.
5. **Majid Khan**, Chengsh Wei, Mingmin Chen, Jiajiao Tao, Ningdong Huang, Zeming Qi, Liangbin Li, CTAB-mediated synthesis and characterization of ZnO/Ag core-shell nanocomposites, *Journal of Alloys and Compounds* 612 (2014) 306-314.

### List of publications not included in this thesis

6. Chengsha Wei, Mingming Chen, Dong Liu, Weiming Zhou, **Majid Khan**, Xibo Wu, Ningdong Huang, Liangbin Li, A recyclable disulfide bond chemical cross-linking high toughness, high conductivity ion gels based on re-shaping and restructuring in gel state, *Polymer Chemistry* 6 (2015) 4067-4070.
7. M. Chen, C. Wei, X. Wu, **Majid Khan**, N. Huang, G. Zhang, L. Li, Metallogels Self-Assembled from Linear Rod-Like Platinum Complexes: Influence of the Linkage, *Chemistry-A European Journal* (2015) 21(11):4213-4217.



8. C. Wei, M. Chen, D. Liu, W. Zhou, **Majid Khan**, X. Wu, N. Huang, L. Li, Recyclable chemical crosslinking high toughness, high conductivity ion gels by sequential triblock copolymer self-assembly and disulfide bond cross-linking, *RSC Advances* (2015) 5(29):22638-22646.
9. A.B. Yousaf, **Majid Khan\***, M. Imran, M. Usman, M.A. Jamal, Influence of particle size on density, ultrasonic velocity and viscosity of magnetite nanofluids at different temperatures, *Nano* 9 (2014) 1450089.
10. C. Wei, M. Chen, J. Tao, X. Wu, **Majid Khan**, D. Liu, N. Huang, L. Li, CdS nanorods assisted thermal oxidation of polythiol segments of PS-b-Polythiols to produce core cross-linking micellar clusters, *Polymer Chemistry* 5 (2014) 7034-7041.
11. **Majid Khan\***, M. Islam, A. Akram, Z. Qi, L. Li, Residual strain and electrical resistivity dependence of molybdenum films on DC plasma magnetron sputtering conditions, *Materials Science in Semiconductor Processing* 27 (2014) 343-351.
12. M.U. Farooq, **Majid Khan\***, A. Faraz, A. Maqsood, W. Ahmad, L. Li, Comparative study of ZnTe thin films prepared using close space sublimation (CSS) and electron beam evaporation (EBE) thin film fabrication techniques for optoelectronic applications, *Materials Technology* 29 (2014) 29-35.
13. **Majid Khan**, M. Islam, A. Akram, U. Manzoor, Processing-structure-property correlation in DC sputtered molybdenum thin films, *Surface Review and Letters* 20 (2013) 1350065.